Development and Construction of the Low-Energy Photon Tagger

NEPTUN

Vom Fachbereich Physik
der Technischen Universität Darmstadt

zur Erlangung des Grades
eines Doktors der Naturwissenschaften
(Dr. rer. nat.)

genehmigte

D i s s e r t a t i o n

angefertigt von

Dipl.-Phys. Kai Lindenberg
aus Bremervörde

Juli 2007

Darmstadt
D17

Referent:	Professor Dr. rer. nat. A. Zilges
Korreferent:	Professor Dr. rer. nat. Dr. h.c. mult. A. Richter
Tag der Einreichung:	17. Juli 2007
Tag der mündlichen Prüfung:	19. November 2007

Abstract

Within the scope of this thesis a photon tagging system was designed and constructed at the superconducting Darmstadt electron linear accelerator (S-DALINAC). The set-up consists of a deflecting magnet, an array of focal plane detectors, the data acquisition system and new beam-line components. The system provides tagged photons in an energy range from 6 MeV to 20 MeV with the emphasis on best possible resolution and intensity. The absolute energy resolution of photons at 10 MeV is better than 25 keV. With the current focal-plane detectors a maximum rate of tagged photons of $10^4\,/(\mathrm{keV}\cdot\mathrm{s})$ can be achieved. An upgrade to more than $10^5\,/(\mathrm{keV}\cdot\mathrm{s})$ with an alternative detector array is under investigation.

The design values mentioned above are the requirements for planned experiments in the fields of nuclear astrophysics and nuclear structure. The most important constraints which have to be considered arise from the special demands of (γ,n) reactions above but close to the particle threshold which generates slow neutrons with energies of a few hundreds of keV. The unambiguous assignment of slow neutrons to prompt electrons is done on-line in special buffered time-to-digital converters. With a design of the data acquisition for this scenario one also covers the requirements for experiments with prompt detection of the ejectiles such as in nuclear resonance fluorescence and (γ,n) far above the threshold.

This photon tagging system enables to measure (γ,x) cross sections as a function of excitation energy and decay patterns after particle evaporation. It is an important extension to the high-flux activation experiments and the nuclear resonance fluorescence experiments below the threshold with untagged bremsstrahlung.

Zusammenfassung

Im Rahmen dieser Arbeit wurde ein Photonentagger am supraleitenden Darmstädter Elektronenlinearbeschleuniger S-DALINAC entwickelt und aufgebaut. Das System besteht aus einem Ablenkmagneten, einem Feld aus Fokaldetektoren, einer neuen Datenaufnahme und mehreren Strahlführungselementen. Es werden Photonen in einem Energiebereich von 6 MeV bis 20 MeV mit einer sehr hohen Auflösung von 25 keV bei 10 MeV zur Verfügung gestellt. Mit den aktuell verwendeten Detektoren kann eine maximale Rate von $10^4\,/(\mathrm{keV}\cdot\mathrm{s})$ getaggter Photonen erreicht werden. Ein Ausbau mit anderen Detektoren wird gerade untersucht um diese über $10^5\,/(\mathrm{keV}\cdot\mathrm{s})$ zu steigern.

Oben genannte Design-Werte sind die Anforderungen der geplanten Experimente im Bereich der nuklearen Astrophysik und der Kernstruktur. Die stärksten Bedingungen, die berücksichtigt werden müssen, kommen von den speziellen Anforderungen von (γ,n)-Reaktionen, die nahe oberhalb der Teilchenseparationsschwelle langsame Neutronen mit Energien von wenigen hundert keV produzieren. Die eindeutige Zuordnung von langsamen Neutronen zu schnellen Elektronen wird online in speziellen, gepufferten Time-to-Digital-Konvertern gemacht. Mit der Auslegung der Datenaufnahme auf dieses Szenario werden die Anforderungen an Experimente mit schnellen Teilchen, wie zum Beispiel Kernresonanzfluoreszenz und (γ,n) weit über der Schwelle, abgedeckt.

Dieser Photonentagger erlaubt es (γ,x)-Wirkungsquerschnitte direkt zu vermessen und Zerfallsschemata nach Neutronenabdampfung zu untersuchen. Es ist eine wichtige Erweiterung zu den Aktivierungsexperimenten mit hohen Flüssen und zu Kernresonanzfluoreszenzexperimenten unterhalb der Schwelle mit einem Bremsstrahlungsspektrum.

Contents

1 Introduction

This work describes in detail the development process of the photon tagging facility at S-DALINAC. The first four letters of the name “NEPTUN” stand for “Niederenergie-Photonentagger”.

The chapters are organized as follows. This chapter gives a general overview about the main research fields within the research centre of excellence SFB634 at the Institut für Kernphysik (institute for nuclear physics) at the Technische Universität Darmstadt. The current experiments will be outlined and their extension with a photon tagging system elucidated. Furthermore the special experimental demands are explained. The second chapter will explain the principle of tagging. This is mandatory for the comprehension of this work. It will also go into the limiting factors for tagging. In chapter three the production of high energy photons with the process of bremsstrahlung will be explained and a quantitative analysis of Monte-Carlo simulations of photons and scattered electrons is given. With this data one can design the geometry of the magnet, which is described in detail in chapter four. Here the focus is on the resolving power of the magnet. Chapter five is about the detectors of the focal plane. The geometry and the principle of operation will be explained. It also addresses the generation of the signals with photomultipliers which were developed especially for this purpose. The data acquisition is one of the most important parts of coincidence experiments. Chapter six discusses the demands of coincidence experiments with slow neutrons and introduces the main electronic module for this task. An extension of the electron-beam transport system with new beam control magnets was necessary and chapter seven deals with the characteristics of the S-DALINAC and the installation of the system. In chapter eight the results of the first test experiments are presented. Besides a direct measurement of the tagged photons with a high-purity germanium detector, a method to measure the momentum spread of the electron beam was developed. Furthermore examples of future experiments on nuclear resonance fluorescence and (γ,n) reactions will be given. The main part of the work closes with final remarks and an outlook to further developments and improvements in chapter nine. The appendices elaborate some details that are referenced in the text.

1.1 Photoresponse of atomic nuclei

The photoresponse of atomic nuclei below and close above the particle threshold was studied at the S-DALINAC for more than ten years. The expression *photoresponse* embraces the

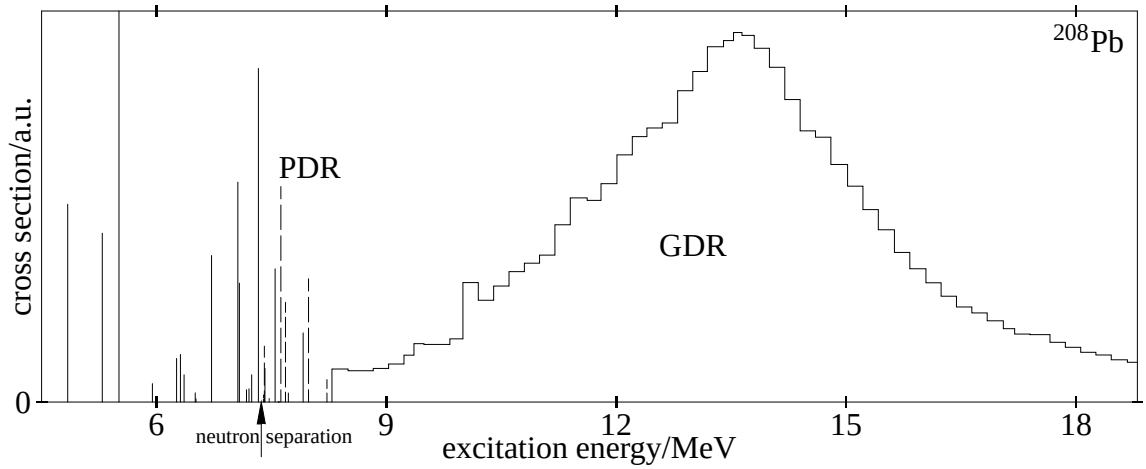

Figure 1.1: The experimental photo-absorption cross section is the quantity that describes the photoresponse of nuclei. For ^{208}Pb this cross section is shown up to 18.5 MeV excitation energy. The data was taken in different experiments. The solid and dashed lines in the low-energy part up to 8 MeV stem from (γ,γ') measurements [Rye02]. The high-energy part was taken by [Vey70, Bel82]. Consider the different units on the ordinate of strength of the low-energy part and the high-energy part. The neutron separation energy of ^{208}Pb is 7367.87 keV.

nuclear responses of an atomic nucleus to an external field of high energy photons. Besides experiments at the old and new photon scattering facility [Zie90, Moh99], respectively, at the S-DALINAC [Ric96] many experiments at other facilities such as Stuttgart Dynamitron [Ham79], Rossendorf ELBE [Arn07], Duke HIγS [Lit97] and AIST Tsukuba [Ohg91]) have been performed.

Figure 1.1 shows an example of a measured photoresponse below and above the particle threshold. The low-energy part of the spectrum below 8 MeV displays data taken from a nuclear resonance-fluorescence experiment [Rye02] at the S-DALINAC. The high-energy part was taken from experiments with two different photon monochromators. In [Vey70] the photo-neutron cross section was determined by in-flight annihilation of positrons and electrons at the Saclay linear accelerator. The fine structure between 9.9 MeV and 11.2 MeV was examined at the Illinois tagged photon facility [Bel82]. The high energy resolution of a few keV in the low-energy part is remarkable. The energy resolution for the photo-neutron experiments is about $100-200$ keV.

The resonance between 8 MeV and 18 MeV is known as the giant dipole resonance. The picture here is an anti-phase oscillation of the protons and neutrons in the nucleus. This is the strongest excitation that is found in almost any heavy nucleus. The giant dipole resonance nearly exhausts the energy-weighted sum rule of an atomic nucleus and contains almost 100 %

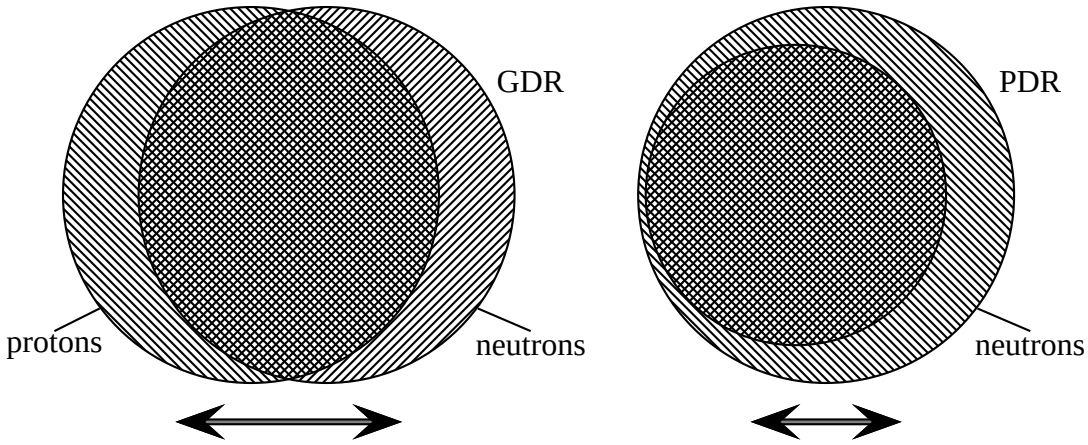

Figure 1.2: These are the classical macroscopic descriptions of two important nuclear resonances. On the left side the giant dipole resonance is shown, where the neutron fluid (hatched diagonal down) oscillates against the proton fluid (hatched diagonal up). On the right side the pygmy dipole resonance is shown, where a neutron skin oscillates around an N-equal-Z core (cross hatched).

of the total strength.

A group of strong transitions below 6 MeV and a resonance-like structure around the particle threshold at 7.4 MeV is observed. The latter is interpreted as the pygmy dipole resonance. A possible macroscopic picture of this mode is the oscillation of a neutron skin of the nucleus against a core with equal numbers of protons and neutrons, see left side of figure 1.2. The nature of the pygmy dipole resonance is still not understood very well and the details of the underlying structure are a matter of ongoing discussions (see [Sav06, Kne06]). A detailed description of this "three-fluid hydrodynamical model" can be found in [Moh71].

Furthermore another excitation is prominent in spherical medium heavy and heavy nuclei. This so-called two-phonon excitation is a vibration of the surface of the nucleus, that can be explained by a superposition of two phonons that describe a coupled vibration of the surface [Str57, Boh57, Boh58]. See [Kne06, Zil00] for detailed reviews.

In figure 1.1 the neutron separation threshold at 7367.87 keV is marked with an arrow. This means that at higher excitation energies the emission of a neutron is more probable than the de-excitation by emission of a photon. A detailed investigation of cross sections for photodisintegration reactions can be performed. These are relevant for the nucleosynthesis of heavy neutron-deficient nuclei.

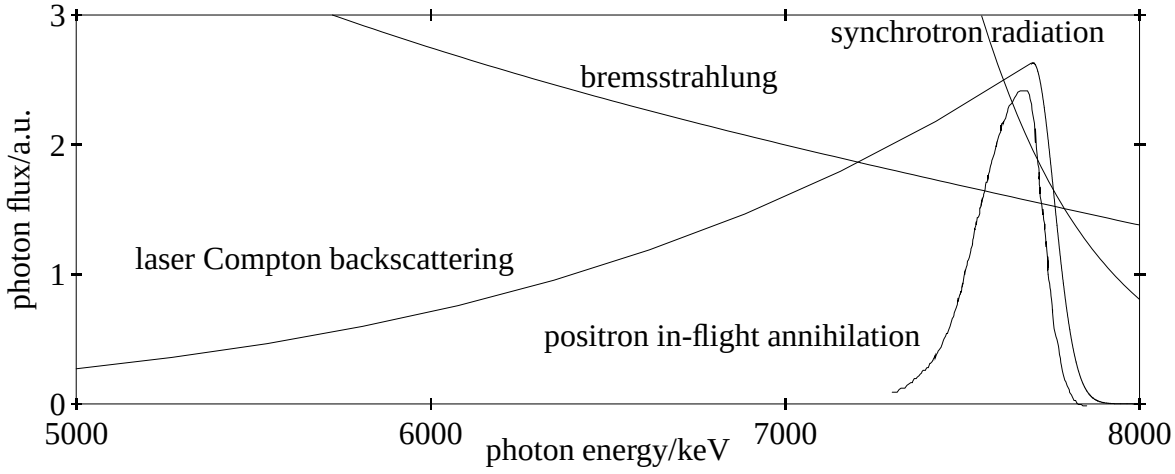

Figure 1.3: The photon spectra of different production methods are compared. The bremsstrahlung and the synchrotron radiation spectra decrease exponentially with higher energies and the energy distributions of Compton laser backscattering and positron in-flight annihilation show a peak at the end of the spectrum. The end-point energies of bremsstrahlung and synchrotron radiation are chosen to be far above the energies shown here to achieve reasonable photon rates between 7 MeV and 8 MeV.

1.2 Experimental set-ups

Experiments on the photoresponse of nuclei have to be distinguished by the energy distribution of the gamma source and by the field of application. The energy distribution depends mainly on the production method of the photons. The easiest way to produce high-energy photons is to use bremsstrahlung of electrons. With this method one obtains a nearly exponentially decreasing energy distribution up to the energy of the electrons. The method of Compton laser backscattering produces a distribution with a maximum energy under zero degrees and decreases with greater angles. The width of the distribution depends extremely on the scattering angle. Synchrotron radiation produced by magnetically bended electron trajectories delivers a rapidly decreasing exponential spectrum of photons. The in-flight annihilation of electron-positron pairs can be used to produce a very sharp energy distribution, but due to the very low flux, this method is not used as a workhorse for the systematic observation of the photoresponse. For a comparison of the energy distributions see figure 1.3. In this figure the bremsstrahlung spectrum is produced by a calculation of electrons hitting a thin copper target at 10 MeV [Sch51]. The synchrotron-radiation spectrum is taken from [Uts05]. The electron energy is 9 GeV and the magnetic field is about 8 Tesla. In this energy range it can be approximated by a Planck spectrum at 3.5×10^9 Kelvin which has some importance for astrophysical applications. The energy distribution of the spectrum of Compton laser backscattering [Uts06b] and positron in-flight annihilation [Aud70, Arg84, Var04] is defined by the solid angle that is covered by the

target. The electron energy and laser wavelength for this Compton laser backscattering spectrum are 555 MeV and 527 nm, respectively. The positron energy for the annihilation spectrum is 7.6 MeV on thin metallic lithium.

The two fields of application that can be mentioned here are nuclear resonance fluorescence (NRF) and photoneutron reactions. The details of the experimental procedures for bremsstrahlung production and laser Compton backscattering are addressed in the following sections.

1.2.1 Nuclear resonance fluorescence with bremsstrahlung

An ideal tool for examining excited states in the energy range up to the particle threshold is nuclear resonance fluorescence (NRF). Generally resonance fluorescence denotes the absorption of electromagnetic radiation and the subsequent emission of radiation with the same wavelength. In the majority of cases this phenomenon is described by excitation of a composite system to a state with a higher energy level with a subsequent decay to the ground state. In atomic nuclei one observes levels with high excitation probabilities in the energy range of a few keV up to the particle threshold, above which the nucleus de-excites predominantly through emission of a particle. For many nuclei this limit is at an energy of a few MeV. Because the transition probability is a function of $(R/\lambda)^{2l}$ times the squared transition matrix element, where R is the nuclear radius and λ is the wavelength of the emitted radiation, it is much harder to transfer high angular momentum l [May92]. This gives a high selectivity in exciting low-spin states. In spite of the definition nuclear resonance fluorescence is not only characterised by resonant excitations and de-excitations but also de-excitations to intermediate states.

One obtains fundamental information on the strong interaction between the nucleons in the atomic nucleus through excitation energies, lifetimes, angular momenta and parities. The analysis of these quantities are based only on the theory of the electromagnetic interaction, which is the best verified theory of interactions in physics.

In 1946 L.I. Schiff [Sch46] proposed to use a continuous γ-ray spectrum produced by a betatron [Wid28, Ker40, Ker41] to perform nuclear resonance fluorescence experiments. A beam of high-energy electrons is decelerated in a solid material to produce bremsstrahlung photons. The converter target may be *thick* to stop all electrons in the target and to get a higher photon flux or it may be *thin* to ensure that only one bremsstrahlung process takes place in order to analyse the scattered electron or use the polarised off-axis bremsstrahlung. The shape of the energy spectrum decreases nearly exponentially to an endpoint energy, which is the energy of the accelerated electrons.

The use of bremsstrahlung produced by electron accelerators has two important features. The photon flux scales directly with the electron current of the accelerator and it is in many cases limited by the cooling technique of the bremsstrahlung target. Modern facilities reach currents of about some tens to a few hundreds microamperes [Ric96, Ham79, Arn07]. The resulting photon rate is typically 10^6 photons keV^{-1} s^{-1} for 3 MeV photons [Moh99, Kne06].

Besides this a continuous photon spectrum enables to excite *all* states up to the endpoint energy simultaneously depending on their transition probability.

Many experiments with thick converter targets have been performed at the S-DALINAC with excitation energies up to 10 MeV (see e.g. [Har00, Har02, Bab02, Rye02, Har04, Vol06]).

1.2.2 Nuclear resonance fluorescence with laser Compton backscattering

Another method to produce high-energy photons is to use Compton laser backscattering of a laser beam off accelerated electrons [San83]. After a head-on collision momentum is transferred from high-energy electrons to low-energy laser photons. When the product of the Lorentz factor of the electron beam γ and the energy of the laser photon is small compared to the rest mass of the electron the peak energy of the backscattered photon is given by $4\gamma^2 E_{\mathrm{Ph}}$ for $\gamma \gg 1$. A strong dependence of this energy on the scattering angle results in a finite energy resolution of $(\gamma\theta)^2$. This means high-energy photons with small energy spread are produced, in other words *monochromatic photons*. This collision also conserves the helicity of the incoming laser photon and Compton laser backscattering provides a photon beam that allows experiments with polarised photons.

Several experiments have been performed at the laser Compton backscattering facility HIγS at Duke University, Durham, e.g. [Sav05, Pie02]. This facility delivers about 10^5 high-energy photons per second over the whole peak. With an electron energy of 500 MeV and a laser wavelength of 379.4 nm a resulting photon energy of 12.2 MeV with an energy width of 120 keV was obtained [Lit97]. These values are based on an incoming photon rate of 10^{18} photons per second and a pulse current of 1.2 mA with a repetition rate of $6 \cdot 10^6$ /s. The laser is a tunable FEL at the same storage ring, so a smooth variation of the photon energy is possible.

The advantage compared to bremsstrahlung is the nearly monochromatic energy distribution of the scattered photons and nearly 100 % polarisation. So one can excite specific states and analyse the decay pattern directly. Nevertheless the high flux of continuous bremsstrahlung photons cannot be reached and it is not possible to measure a wide spectrum in one run.

For all nuclear resonance fluorescence experiments the detection of photons emitted by the nucleus requires a very high energy resolution to resolve densely lying levels. A resolution of the order of some tenth of a percent was available with the advent of the first high-purity germanium detectors in the early seventies of the last century. The research on the development was initiated at the Lawrence Berkeley Laboratory and General Electric [HPGE86]. In the fully depleted germanium crystal the production of a electron-hole pair consumes about 3 eV of energy. So about 5×10^5 electron-hole pairs are produced by an incoming photon with an energy of 1.5 MeV. Because of the high correlation of the individual pair-production processes among one another (Fano factor) the absolute resolution is about 2.5 keV. This is ideal for the examination of nuclear γ rays.

1.2.3 Photo-disintegration reactions for nuclear astrophysics

At excitation energies above the particle threshold particles can be emitted by a nucleus. To study (γ,x) experiments generally two methods are used. The first method is to measure the ejectile of the reaction directly with an appropriate detector. This needs a good shielding of the gamma background and much effort to distinguish different particles such as pulse shape discrimination, time-of-flight measurements and energy-loss measurements. Amongst others a reasonable energy resolution for the detection of the ejectiles enables to draw conclusions for an energy dependence of the reaction cross section.

At the S-DALINAC the technique of photo-activation is used to study (γ,x) reactions [Moh00]. The activation of the target is done by (γ,x) reactions and the target contains the accordant daughter nuclei. Then, beta decays to excited states of daughter nuclei follow and the final gamma decays to the ground state are measured with high-purity germanium detectors. With the radioactive decay law this allows to count the activated nuclei and to calculate the integral reaction cross section. This method is restricted to nuclei whose reaction chain includes a beta decay with a half-life between some seconds and a few years. At the photo-activation set-up at the S-DALINAC the lower limit for the half-life is some minutes. Additionally, the beta decay must have measurable consequent gamma decays.

Both approaches lead to important contributions details of astrophysical network calculations of nucleosynthesis [Moh01, Vog01, Vog02, Vog03, Moh03b, Moh03a, Son03b, Son03a, Son04, Uts06a, Uts06c].

1.3 Experimental advantages using a photon tagging system

The explained methods for the production of photons with energies around the particle threshold have several advantages.

A continuous bremsstrahlung beam can be produced very easily with a simple set-up at an electron accelerator. The continuous spectrum itself has the advantage that a complete scan of the excitations can be performed with only one accelerator setting. But in nuclear resonance fluorescence experiments below the threshold one may need several experiments with different endpoint energies to estimate feeding from higher states in the nucleus. Above the particle threshold it is very difficult to measure an energy dependent cross section with high energy resolution and integral cross sections are very sensitive to the endpoint energy especially near the threshold.

As mentioned before, the method of Compton laser backscattering enables one to produce a peaked photon spectrum at the desired energy. The width is mainly defined by the solid angle that is covered by the target. One can reach a resolution of about 80 keV at 10 MeV photon energy at the expense of photon rates. A high energy resolution at low photon rates

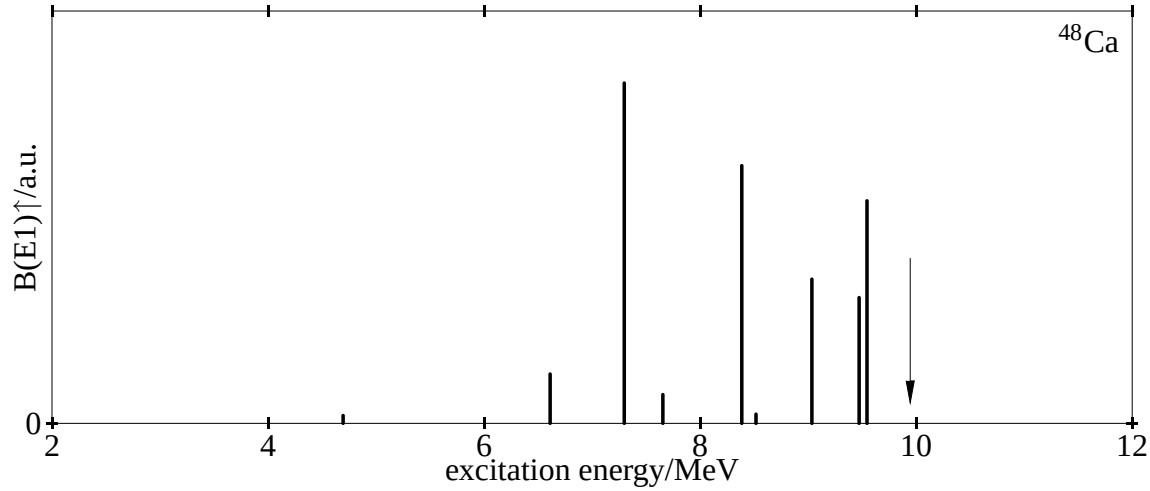

Figure 1.4: The distribution of the reduced dipole excitation strength of ^{48}Ca is shown. The neutron separation energy is marked with an arrow at 9.945 MeV which was the detection limit for the experiments. The strength is predominantly located close to this energy. The data are taken from [Har02].

requires very long beam times and to cover a range of 2 MeV about twenty runs with different apparatus settings are needed. Furthermore, the required machinery is much more complicated, as described above.

A photon tagging system enhances the production of bremsstrahlung by the determination of the photon energy. The energy of nearly each produced photon is measured with high energy resolution. Although the maximum flux is limited by this determination process, a much higher rate than in laser Compton backscattering is obtained with respect to the energy resolution. Besides that, the machinery could be kept very simple. In the past many photon tagging facilities have been developed for different energies [Are82, Kno82, Kel85, Ter86, Adl90, Kra91, Ant91, Det92, Vog93, Sob00, Nau03, Hir06]. This work has been inspired by many of them.

1.3.1 Nuclear-structure studies below and above the particle threshold

The major part of the photoresponse in spherical nuclei up to the giant dipole resonance is governed by electric dipole excitations. In the last few years the experimental investigation of the strength below the particle threshold gave important details of the pygmy dipole resonance. A systematic study of the structure in many nuclei has been performed below the particle threshold [Rye02, Zil02, Har04, Vol05, Vol06]. Preliminary results show that the simple description of the three-fluid hydrodynamical model of an oscillation of a proton-neutron core against a neutron skin cannot be confirmed. Other experiments with α scattering on ^{140}Ce [Sav06] even

show a structural splitting of the pygmy dipole resonance.

All these studies have been limited by the particle threshold because of the restriction to the detection of the gamma rays emitted by the excited nucleus. But data of some nuclei give rise to the assumption that part of the pygmy dipole resonance is above the particle threshold. In figure 1.4 the evaluated distribution of the reduced electric dipole excitation strength of the doubly-magic nucleus ^{48}Ca is shown. The neutron separation strength at 9.945 MeV is marked with an arrow. One clearly finds that the main part of the strength is located close below the threshold. There is no strong flattening towards the threshold, so it is important to measure the characteristics of the photoresponse of those nuclei above the threshold to understand the structure.

Above the threshold nuclei prefer to decay by particle emission. Since the particle detection with high energy resolution is not possible close to the threshold one can countervail this by determining the energy of the exciting photon. The tagging facility allows to study nuclear structure below and above the particle threshold with high energy resolution. The cross section of the reaction with the target nucleus and the decay pattern of the target nucleus or its daughter nucleus can be measured systematically with high precision.

1.3.2 Determination of astrophysically relevant cross sections

Collective dipole excitations of neutron deficient nuclei offer an experimental access to the nucleosynthesis of the elements. They allow realistic estimates of temperature dependent (γ,n) reaction rates and therefore (n,γ) reaction rates via detailed balance [Rau00]. Figure 1.5 shows the stellar photon bath as a Planck spectrum and a typical (γ,n) cross section that covers the giant dipole resonance. The reaction rate is the product of the photon distribution and the cross section. Due to the exponential decrease of the photon distribution with the energy and the threshold behaviour of the cross section only a small energy region yields significant contributions to the total reaction rate. This energy window is located above but close to the threshold. This Gamow-like window is the astrophysically important photon energy range for the p process. New experiments can be performed in this energy range with high resolution using the photon tagging facility.

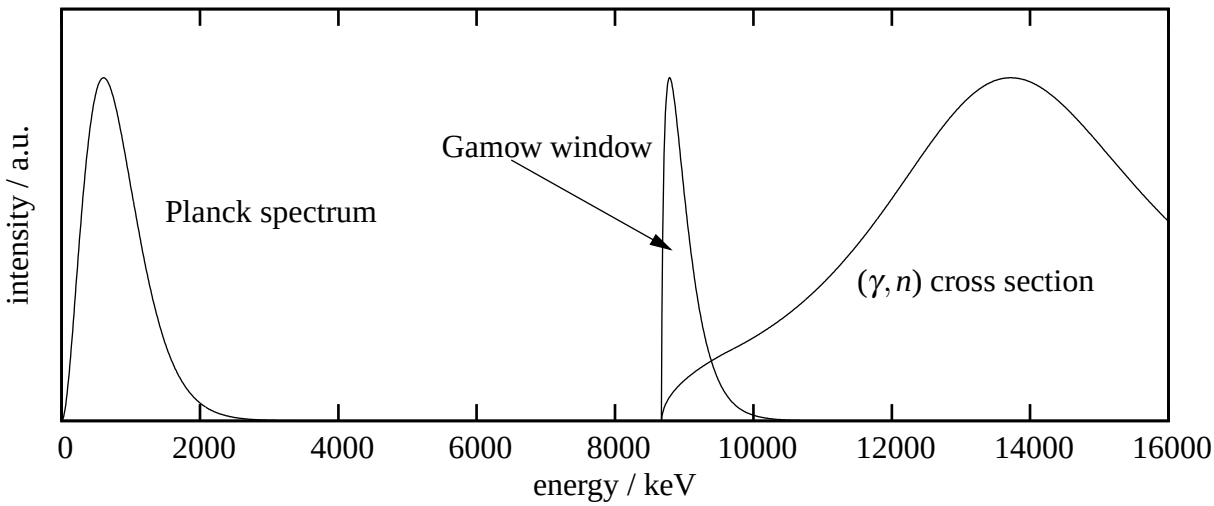

Figure 1.5: The Gamow window of (γ,n) reaction rates in nuclear astrophysics is the peak close above the particle threshold in the product of the photon flux in the stellar photon bath and the nuclear (γ,n) cross section. Due to the Planck distribution of the photons and the photo-disintegration threshold, a small window with high reaction rates is obtained.

2 Tagging process

In the early fifties of the last century the first photon tagging spectrometer was developed. The study of the production of protons by photons from light nuclei required essentially mono-energetic photons for the incident spectrum because the conventional subtraction technique of results from different bremsstrahlung spectra at different end-point energies was too inaccurate [Per52, Gol53b]. Furthermore the fundamental nuclear theory needed results from mono-energetic photon beams.

Weil and McDaniel [Wei53] used the synchrotron at Cornell University, Ithaca. This facility had produced bremsstrahlung beams until several years ago up to endpoint energies of a few hundreds of MeV. The tagging procedure is essentially a method for selecting or identifying individual photons of a given small energy range out of a continuous bremsstrahlung spectrum. This technique was originally suggested independently by Koch at Illinois and by Camac at Cornell. As described in chapter 1 the production of bremsstrahlung is generally done by scattering electrons at a radiator. For tagging facilities thin radiators are required to guarantee single event processes. At Cornell the *internal tagging* method with a thin ($250\,\mu$m) copper target was used. The basic concept is as follows. A synchrotron is a storage ring for mono-energetic electrons with a constant magnetic field in the bending magnets. If the electrons are degraded by a thin radiator foil inside the synchrotron they produce bremsstrahlung. Ideally an electron should not produce more than one photon by interactions inside the foil. To fulfil this constraint the photon-production yield is some order of magnitude below one. After a bremsstrahlung process the initial momentum $\mathbf{p}_0$ of the incident electron is shared between the momenta of three particles, the emitted photon, $\mathbf{p}_\gamma$, the change in momentum of the scattering nucleus, $\mathbf{p}_{\text{recoil}}$, and the degraded electron, $\mathbf{p}_e$:

$$\mathbf{p}_0 = \mathbf{p}_e + \mathbf{p}_\gamma + \mathbf{p}_{\text{recoil}}.$$

Due to its large mass the nucleus can take any recoil momentum, so the kinematic relation between the final electron and the photon is not fixed to particular scattering angles. However for the same reason the recoil energy is negligible and then from the conservation of energy it follows

$$E_\gamma = E_0 - E_e. \tag{2.1}$$

This simple equation points out the principle of tagging. The energy of the scattered electron is linearly connected to the photon energy. If the energy of the electron is measured the energy of the photon can be calculated. By using a coincidence set-up as described in chapter 1 the energy

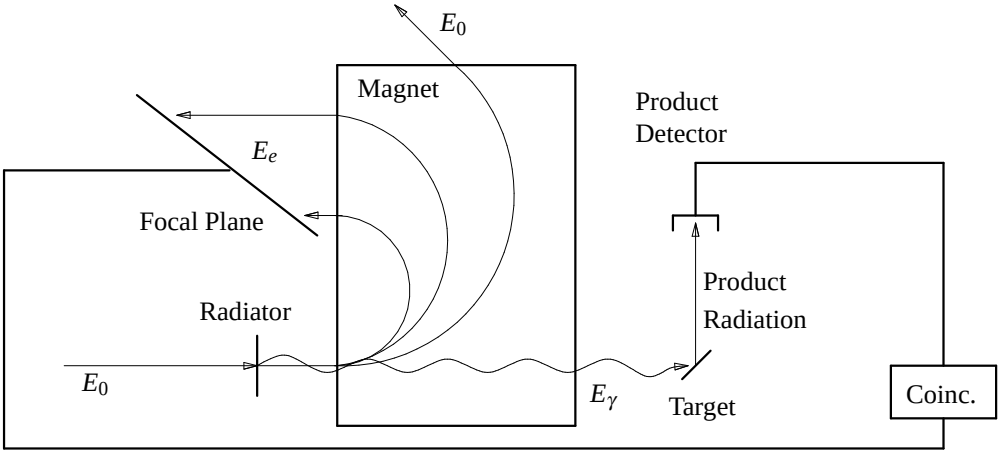

Figure 2.1: The incoming electron beam, denoted with E_0, hits the radiator with a constant energy from left. In the radiator at most one bremsstrahlung photon is produced and besides elastic scattering, no more interactions occur. The produced photon is not deflected by the magnet and hits the experimental target for the nuclear reaction. The reaction product is then detected. The degraded electron is bent to the focal plane for momentum analysis. More than 99 % of the electrons do not perform an interaction in the radiator and leave the magnet without energy loss. An electronic coincidence system assigns the reaction products and the appropriate degraded electron. Since the energy of the incoming electron is known one can easily determine the energy of the photon that caused the reaction.

of each emitted photon is known. Apart from the energy definition of the incident electrons and the energy resolution of the electron detection system, the accuracy depends on the additional energy loss due to straggling in the radiator target. These open issues are discussed later.

At the Cornell synchrotron, the detection of the scattered electrons is done with only one electron detector that is placed in the synchrotron ring near the beam line after the target. Due to the energy loss after the bremsstrahlung process, the bending radius of the electron is smaller than that of the main beam, and those electrons are deflected to the detector. The energy range of detectable electrons is defined by the acceptance of the detector. The geometry was chosen so that electrons of 120 MeV can be detected at a synchrotron energy of 310 MeV with a resolution of about 50 MeV. The resulting tagged photon energy is 190 MeV with the same absolute energy resolution.

At the external tagging facility a dedicated electron beam is used for the tagging method. The advantage is that an optimised spectrometer can be used. The best energy resolution for the electron detection is obtained with magnetic spectrometers with a high-rate detector array in the focal plane. Details will be discussed in chapter 4. In figure 2.1 the principle of an external photon tagging facility is shown. The first external tagging facility was built in 1953

by Goldemberg [Gol53a] at the Illinois betatron. This was still a tagging facility with only one tagged photon energy, but the tagging energy could be changed from zero to 19 MeV by changing the energy of the incident electrons. Later the Illinois tagging facility was upgraded with a focal-plane detector array [Kno82].

2.1 Tagging efficiency

An important quality feature of a photon tagging facility is reflected in the probability that the energy of a produced photon is known. This *intrinsic tagging efficiency* ε_{int} can be written as

$$N_{\gamma,\text{tagged}} = \varepsilon_{\text{int}}(E_\gamma) \cdot N_\gamma$$

where N_γ is the number of all primarily produced photons and $N_{\gamma,\text{tagged}}$ the number of tagged photons. The intrinsic tagging efficiency is equal to the electron detection efficiency of the magnetic spectrometer with the focal-plane detectors if the radiator target is thin enough so that secondarily (and higher in order) produced photons can be neglected.

$$\varepsilon_{\text{int}}(E_\gamma) = \varepsilon_{\text{det}} C(E_\gamma) \int_0^{\theta_{\text{ver}}} \int_0^{\theta_{\text{hor}}} I(E_\gamma, \vartheta) d\theta_h d\theta_v \tag{2.2}$$

with $C^{-1}(E_\gamma)$ as the sum of all produced photons for normalisation ε_{det} is the detection efficiency of the focal-plane detectors that is nearly independent of the electron energy in this energy range, $I(\vartheta)$ is the radial symmetric intensity distribution of the photon producing electrons after the radiator. The parameter ϑ is the azimuthal electron angle

$$\tan^2 \vartheta = \tan^2 \theta_h + \tan^2 \theta_v$$

with a parametrisation in the horizontal and vertical angles θ_h and θ_v, respectively. The horizontal and vertical angular acceptance of the spectrometer is given by θ_{hor} and θ_{ver}. In equation (2.2) the expression $C \int I d\theta_h d\theta_v$ describes the fraction of electrons that are focused to the electron detectors. This will be discussed in chapters 3 and 4.

The photons produced in the radiator target can be scattered afterwards at the collimator borders or other material. Then the photon that hits the experimental target is not the tagged photon. This background affects the *experimental tagging efficiency*. The ratio of primary photons and the sum of primary and background photons decreases directly the efficiency

$$\varepsilon_{\text{exp}} = \frac{\dot{N}_{\text{prim}}}{\dot{N}_{\text{prim}} + \dot{N}_{\text{BG}}} \varepsilon_{\text{int}}. \tag{2.3}$$

This ratio has to be estimated in Monte-Carlo simulations.

Background events in the electron detectors of the focal plane only affect the tagging efficiency if the rate is too high for an unambiguous assignment of photon and electron. A direct

correlation to the efficiency is only given if the background event is detected simultaneously in the same detector element. As shown in section 2.2.2 at a rate of 10^6 /s the probability of having events in a time window of 10 ns is less than $P_{10^6\,/\mathrm{s}\,\cdot\,10\,\mathrm{ns}}(0) = 1\,\%$ and can be neglected at lower rates and better time resolution.

The tagging efficiency is not changed if the background event is detected simultaneously in another detector element. If all events including the true coincidences are counted, this does only lead to higher background which can be subtracted in the analysis. Those background events that are counted without a true coincidence were taken into consideration with the introduction of the experimental tagging efficiency on the condition that the corresponding photons are produced as a consequence of the incoming electron beam. Additional uncorrelated background on the experimental side has to be regarded separately and has to be added to $\dot{N}_{\mathrm{BG}}$ in equation (2.3).

The difference between this definition of the tagging efficiency and that of other photon tagging facilities given by

$$\varepsilon = \frac{\dot{N}_\gamma}{\dot{N}_{\mathrm{focalplane}}}$$

is because the main trigger is generated by the focal-plane detectors and ε is the probability that a photon is produced and hits the experimental target. Therefore, the direct comparison of these quantities is not possible. This *photon production probability* is necessary to control the electron current with the focal plane detectors. With high photon production probabilities the absolute photon flux can be controlled with high accuracy. Remembering that the main trigger of experiments at NEPTUN is generated by the experiment this precondition is not given.

2.2 Experimental constraints to the specification

This section describes the requirement specification and a rudimentary feature specification of the photon tagging facility. The features and limits are described in detail within the main part of this work.

As shown in figure 2.2 the neutron separation energies of most stable nuclei lie between 6 MeV and 14 MeV. The planned experiments, as described above, need photon energies from close below to a few MeV above the neutron separation energy of the target. To accomplish this requirement for many nuclei photon energies from about 6 MeV to 20 MeV have to be provided with high energy resolution. To resolve the final states of the daughter nucleus after photodisintegration and to examine structures in the giant dipole resonances, the energy resolution has to be as good as possible. An resolution of better than 25 keV at a photon energy of 10 MeV is possible, as described later. Nowadays there is no photon source for that energy range with this high resolution. Other photon tagging facilities provide much higher energies or not reach such an energy resolution [Adl97, Ant91, Nau03, Vog93, Sob00]. Of course the photon rate should be as high as possible to gain enough experimental statistics for the analysis

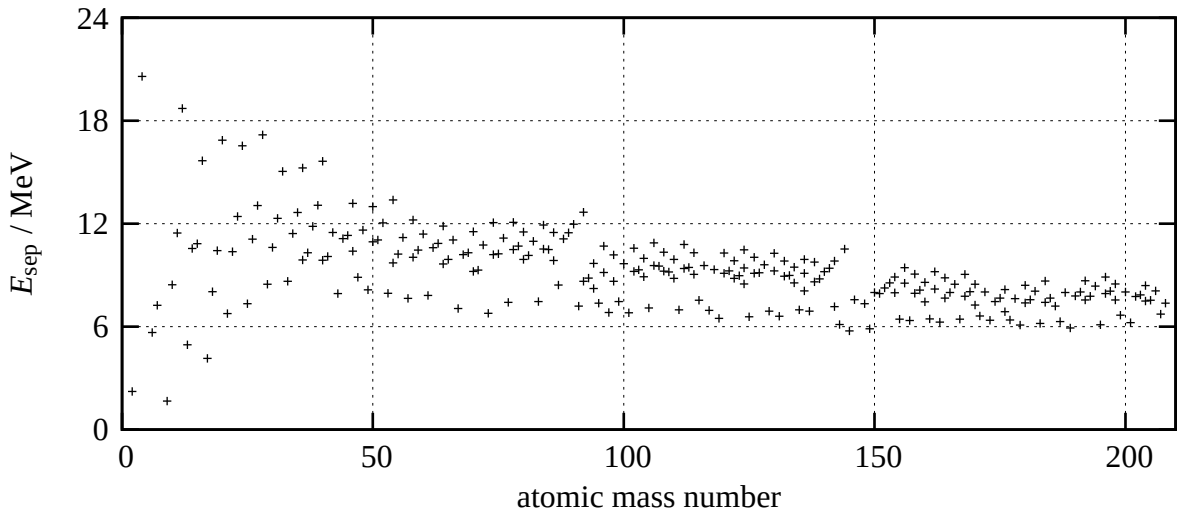

Figure 2.2: Neutron separation energies of stable nuclei via the atomic mass number. Nearly all nuclei have separation energies above 6 MeV. The light nuclei with lower separation energies are ^{2}H, ^{6}Li, ^{9}Be, ^{13}C and ^{17}O. The heavy nuclei close below are ^{145}Nd at 5755.29 keV, ^{149}Sm at 5871.07 keV and ^{189}Os at 5920.27 keV. The data are taken from [Wap03].

in a reasonable time. A rate of $10^4\,\gamma/(\mathrm{keV}\cdot\mathrm{s})$ is the lower limit for most applications.

2.2.1 The superconducting Darmstadt linear accelerator for electrons

The electron accelerator at the institute for nuclear physics is a recirculating linear accelerator with superconducting radio frequency cavities (see figure 2.3 for an overview). The cavities of the S-DALINAC [Ric96, Bru00] (Superconducting DArmstadt LInear ACcelerator) are made of niobium which are cooled to 2 K and driven with a frequency of $c/0.1\,\mathrm{m} \approx 3\,\mathrm{GHz}$. The accelerator consists of an 10-MeV injector that can provide a current of about 45 μA. The injector alone can be used for low-energy channelling experiments [Fre97] and the above mentioned nuclear resonance fluorescence and photo-neutron experiments with high intensity.

The main accelerator increases the electron energy on each passage by up to 40 MeV. Two recirculations are possible which leads to a maximum energy of 130 MeV. The electrical power supplies of the cavities in the main accelerator allow currents of 20 μA for different experimental facilities as shown in figure 2.3.

Besides the new photon tagging facility in the experimental hall, there are experiments to derive nucleon polarisabilities from Compton scattering [Wat05], high-energy channelling radiation [Net95], the Q-Clam spectrometer with high momentum acceptance and large angular

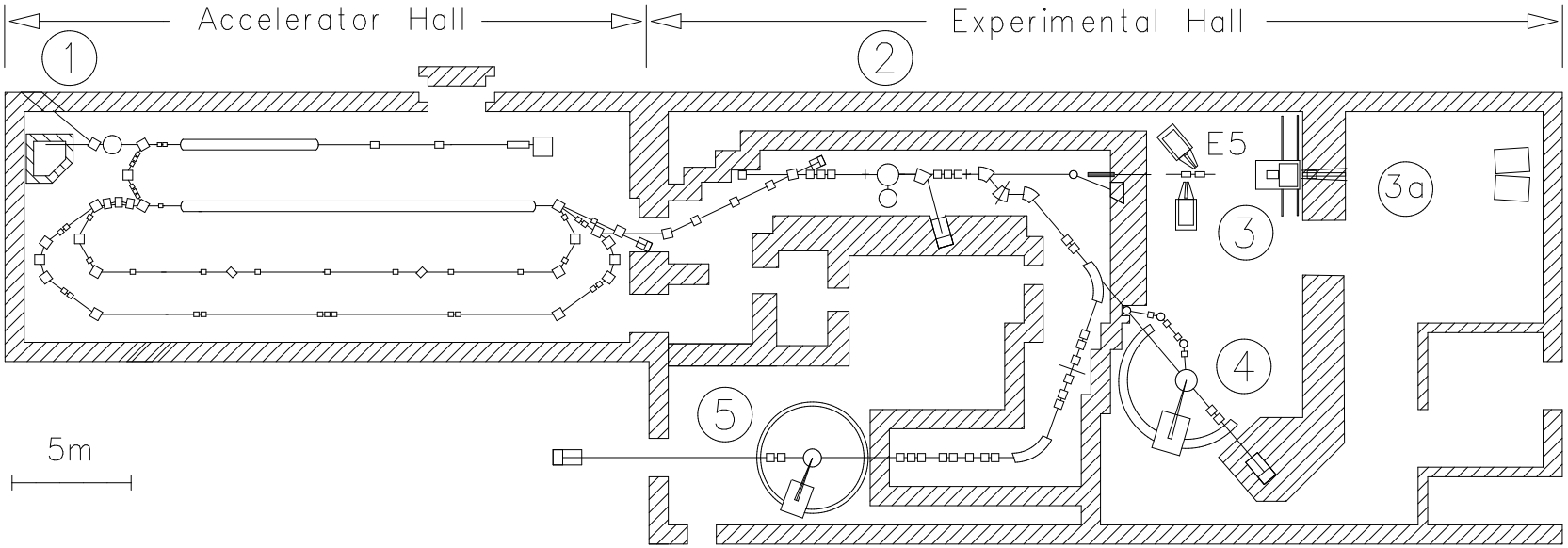

Figure 2.3: The accelerator and the experimental facilities are located in the basement of the institute for nuclear physics. On the top of the picture of the accelerator hall is the electron gun and the injector. On the top-left side is the high-intensity bremsstrahlung set-up HIPS at ① for the previously mentioned experiments. Furthermore experiments with low-energy channelling radiation and parametric x rays have been performed. In the lower part of the picture is the main accelerator with the two recirculations. On the right side at the end of the accelerator hall is the beam extraction to the experimental hall.

At ② is a set-up for channelling and parametric x rays at high energies. ③ and ③a is a shared location for experiments for nucleon polarisabilities from Compton scattering and the new low-energy photon tagging facility. This part is also called E5. At ④ and ⑤ are two electron spectrometers for electron scattering experiments.

acceptance [Hum92] and the high-resolution energy-loss spectrometer LINTOTT [Len04].

Due to the frequency of 3 GHz the accelerator delivers virtually a continuous electron beam. The bunch length is about 2 ps with a average bunch content of 2.1 electrons per nA.

The complexity of the beam control increases with the energy. For instance the so-called single-pass mode without any recirculations is much easier to prepare than a three-pass mode. Moreover the cavities should not be operated at the power limits, so one should consider the simplest mode of operation for the new photon source.

2.2.2 Intensity and background estimate

The maximum intensity is generally not limited by the current of the electron beam, but rather by the dead time of the detector system and random coincidences. Since the events are distributed uniformly in time the next-neighbour distribution is exponential, which can be derived from the Poisson distribution.

The Poisson distribution is given by

$$P_{\lambda t_0}(n) = \frac{(\lambda t_0)^n}{n!} e^{-\lambda t_0}.$$

$P_{\lambda t_0}(n)$ is the probability to have exactly n counts in a time span of t_0 at a count rate of λ. To get the next-neighbour distribution n is set to zero and

$$P_{\lambda t_0}(0) = e^{-\lambda t_0}, \tag{2.4}$$

which describes the probability to have no events in t_0.

Now the maximum rate per detector element can be calculated. Typical photomultiplier tubes, which are used in this tagging facility have a signal width of about 10 ns [Kno00].

$$P_{\lambda\, 10\,\mathrm{ns}}(0) = 0.99 = e^{-\lambda \cdot 10\,\mathrm{ns}}$$

$$\Rightarrow \lambda = \frac{-\ln 0.99}{10\,\mathrm{ns}} \approx 10^6\,/\mathrm{s}.$$

This result gives an estimate for the maximum count rate in one detector element.

In coincidence experiments one assigns events by their time stamps. The time of two events can be assigned with an accuracy of better than 10 ns. The final tagging system will contain 128 detector elements each with a maximum count rate of $\lambda = 10^6\,/\mathrm{s}$ and a *trigger signal* from the photonuclear experiment. The trigger signal has a few orders of magnitude less count rate than the tagging system itself.

With a total count rate of $10^8\,/\mathrm{s}$ in the tagging system (128 detector elements with $10^6\,/\mathrm{s}$ each) and the given total time definition t_0 the next-neighbour distribution gives a probability for a random coincidence of

$$P_{RC} = 1 - P_{10^8\,/\mathrm{s}\,\cdot\,10\,\mathrm{ns}}(0) = 1 - e^{-10^8\,/\mathrm{s}\,\cdot\,10\,\mathrm{ns}} = 1 - 1/e \approx 63.2\,\%.$$

$P_1 = 1/en!$	
$P_1(0)$	0.368
$P_1(1)$	0.368
$P_1(2)$	0.184
$P_1(3)$	0.061
$P_1(4)$	0.015
$1 - \sum_{n=0}^{4} P_1(n)$	0.004

Table 2.2: This table shows the probabilities for different numbers of random coincidences at a maximum count rate of 10^8 photomultiplier events per second and a time resolution of 10 ns.

So for each true coincidence one or more additional background coincidences are registered with a probability of 63.2 %.

Table 2.2 shows the probabilities for zero to four additional background events. The additional background events are not a problem for the analysis because they are energetically distributed uniformly across the whole recorded spectrum in the analysis. Compared to that the true coincidences are distributed only in a few channels so the statistical weight of the background can be neglected. The background rate can be estimated by the expectation value of the distribution

$$\sum_{n=0}^{\infty} n \cdot P_{\lambda t_0}(n) = \lambda t_0 = 10^8 \,/\mathrm{s} \cdot 10\,\mathrm{ns} = 1.$$

This means that for one true coincidence one background event is registered on average.

$$\dot{N}_{BG} = \dot{N}_{TC}$$

The peak-to-background ratio of a spectrum with uniformly distributed background is defined as the rate of true events per sum of peak widths divided by the rate of background events per spectrum width as given by

$$R_{\mathrm{p2b}} = \frac{\dot{N}_{TC}}{\sum_n w_n} \cdot \frac{W_{\mathrm{spectrum}}}{\dot{N}_{BG}}.$$

If a spectrum width of more than hundred channels, which is one channel per detector element, and a sum of peak width less than twenty channels is assumed a peak-to-background ratio of better than

$$R_{\mathrm{p2b}} = \frac{100}{20} = \frac{5}{1}$$

is expected. For example the sum of peak widths can occur from seven peaks with a single width of three channels. For Gaussian peak shapes the width is defined as $\sqrt{2\pi}\sigma \approx 2.5\sigma$ with σ as the root mean square deviation. This definition is equivalent to a width of a rectangle with the same height and area.

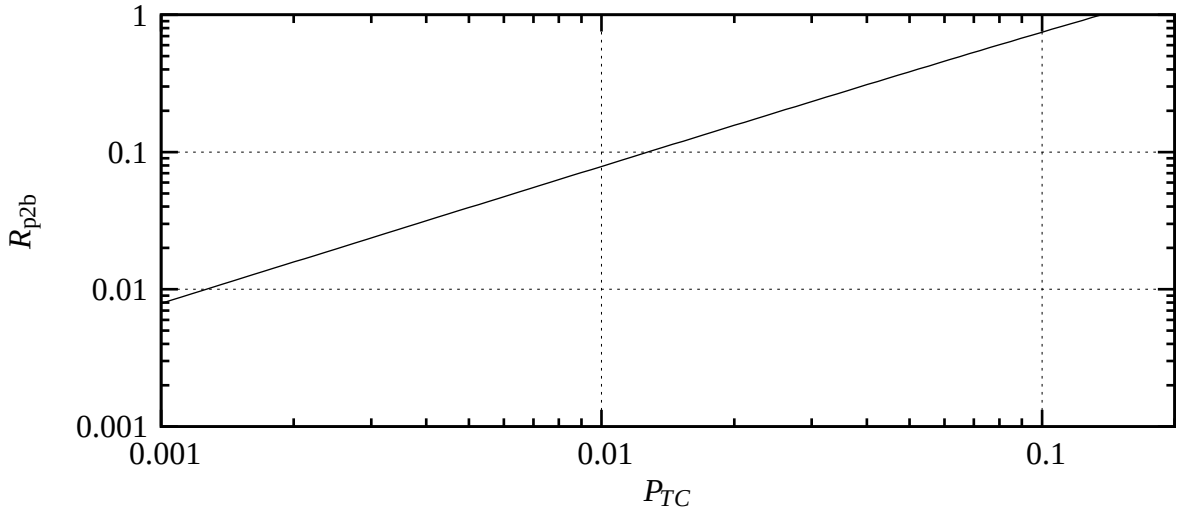

Figure 2.4: Equation (2.5) describes the peak-to-background ratio in the raw spectrum of coincidence experiments as a function of the signal-to-noise ratio of the trigger signal P_{TC}.

The optimum value deduced above can only be reached if only true coincidences occur. Generally not every trigger signal belongs to a true coincidence. If the chance of a true coincidence is the signal-to-noise ratio P_{TC} the rate of true coincidences derives from the trigger rate

$$\dot{N}_{TC} = P_{TC} \cdot \dot{N}_{TR}.$$

All other events

$$\dot{N}'_{BG} = (1 - P_{TC}) \cdot \dot{N}_{TR}$$

are additional background events and with a probability of $P_{RC} = 1 - P_1(0) = 63.2\,\%$ the background event is assigned to a hit in the focal plane. Then the peak-to-background ratio changes to

$$R_{\mathrm{p2b}} = \frac{\dot{N}_{TC}}{\sum_n w_n} \cdot \frac{W_{\mathrm{spectrum}}}{\dot{N}_{BG} + P_{RC} \cdot \dot{N}'_{BG}} = \frac{W_{\mathrm{spectrum}}}{\sum_n w_n} \cdot \frac{1}{(1 - P_{RC}) + \frac{P_{RC}}{P_{TC}}}. \tag{2.5}$$

The shape is plotted in figure 2.4. A peak-to-background ratio of better than $R_{\mathrm{p2b}} = 1/10$ can be reached if the signal-to-noise ratio of the trigger signal could be kept above $P_{TC} = 1\,\%$.

Thus the limit for the maximum intensity is based on the count rate of the detector elements and the time resolution of the coincidence. To maximize the intensity only a small energy range should be covered by one detector element. If a range of 25 keV is covered and the count rate is limited to 10^6 photons per second an intensity of $I = 4 \times 10^4 \,/(\mathrm{keV} \cdot \mathrm{s})$ can be reached.

2.2.3 Coincidence experiments with slow particles

In nuclear physics generally the products of different nuclear reactions are detected. Often the desired information about the reaction itself can only be obtained if more than one product in one reaction or reaction chain is measured. The simplest method is to record all events with a time stamp and then search the data for events with similar time stamps. But with an accuracy of the time data of 1 ns and beam-times of several weeks the time has to be stored as an 8-byte value. At a count rate of 10^8 /s the resulting data rate is about $760\,\mathrm{MiB/s} = 62\,\mathrm{TiB/day}$. To record and store this amount of data one needs 62 hard-discs per day and more than 99.9 % is useless background. So the general idea is to start the acquisition not unless two or more different events occur simultaneously within a few nanoseconds that may be correlated. This method reduces the background by a few orders of magnitude without losing too much information.

A new problem arises when slow particles come into play. Although the time resolution of the detection is in the order of some nanoseconds the time stamp itself does not define the time of particle scattering or particle production. It depends strongly on the time of flight. If the lower limit for the time of flight is a microsecond, then one possible solution is to reduce the count rate of the tagging system to 2×10^4 per second and per detector element or to use a pulsed beam with a repetition rate of less than 1 MHz. With a pulsed beam one has to pay attention to multiple produced photons from different electrons in one bunch.

In coincidence experiments with slow particles where the energy is known the information suffices to calculate the time of the reaction. The method that is used with this tagging facility is explained in chapter 6.

3 Production of bremsstrahlung

As mentioned in the introduction, for a photon tagging facility bremsstrahlung is used as a photon source. This chapter deals with the production of bremsstrahlung by electrons and a simulation with the Monte-Carlo library Geant4 [Ago03, All06]. In the next section a general overview of the interaction of electrons with a kinetic energy of a few million electron volts with matter is given. The following sections describe some important properties of bremsstrahlung photons and the scattered electrons. This chapter will finish with the requirement specification of the electron spectrometer and the radiator target.

3.1 Interaction of electrons with matter

The interaction of electrons with matter is fully described by electromagnetic forces. For electrons with an energy of a few MeV, three classes of interaction can be distinguished. First of all, elastic scattering and quasi-elastic scattering, where atoms get excited but not ionised, leads to a small energy loss and angular variation of a mono-energetic incident electron. No other particles are produced. Particle production can occur with ionisation, (including Møller scattering) and bremsstrahlung. Ionisation is considered as Møller scattering if the energy loss is above half of the rest mass of an electron.

3.1.1 Collisional energy loss

The understanding of energy loss in the radiator target due to collisions is vital for the energy resolution of the tagging facility. The resulting energy shift to lower energies leads to an absolute correction of the detected electron energy and the energy spread contributes directly to the total energy resolution. This energy loss can be described by the Bethe-Møller formula [Bet30, Møl32] for electrons

$$-\left(\frac{dE}{dx}\right)_c = \frac{2\pi e^4 NZ}{m_e v^2}\left[\ln\left(\frac{m_e v^2 E\gamma^2}{2I^2}\right) + \frac{1}{\gamma^2} - (\ln 2)\left(\frac{2\gamma-1}{\gamma^2}\right) + \frac{(\gamma-1)^2}{\gamma^3}\right]$$

with Z and $N = \rho N_A/A$ as atomic number and number density, that is expressed by density ρ, respectively, Avogadro constant N_A and molar mass A, electron rest mass and velocity m_e and v, E as kinetic energy and the Lorentz factor $\gamma = (E/m_e c^2 + 1)$. The quantity I is the mean ionisation energy of atomic electrons, which is tabulated in [ICRU93]. For $Z \geq 13$ Sternheimers

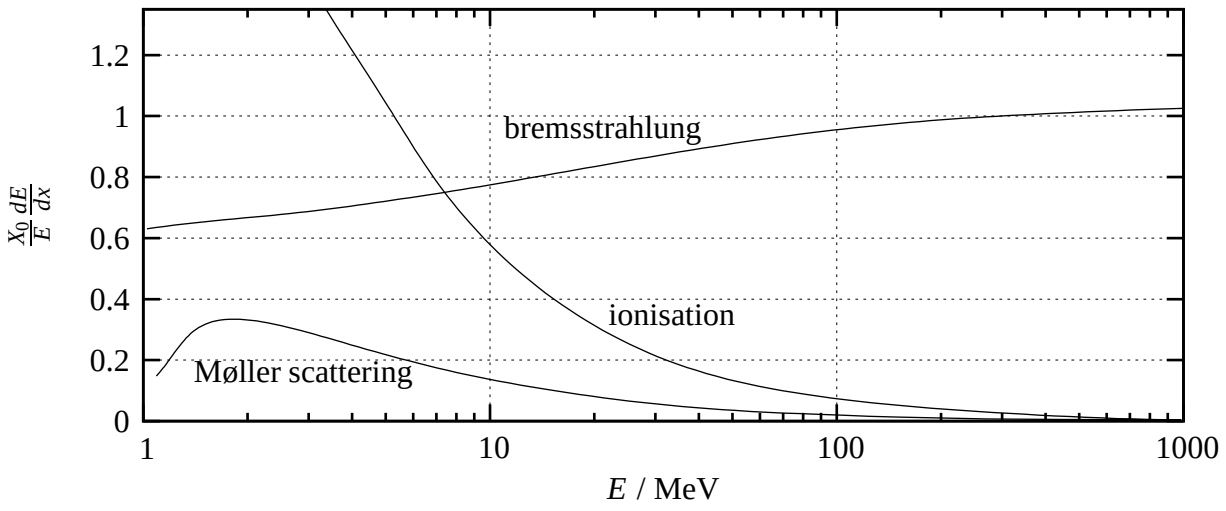

Figure 3.1: Shown is the relative energy loss $\frac{dE}{dx}/E$ for a given radiation length X_0 as a function of the electron energy. The distinction between ionisation and Møller scattering is made in dependence of the energy loss per collision. If the energy transfer to an atomic electron is more than the half of the rest mass of an electron the scattering process is considered as Møller scattering. The calculation is made for lead with $Z = 82$. Due to uncertainties in the radiation length the energy loss is given in units of X_0^{-1}. The current value given in the Table of Atomic and Nuclear Properties of Materials [Yao06] is $X_0(\mathrm{Pb}) = 6.37\,\mathrm{g/cm^2}$. The data is adapted from [Yao06].

[Ste66] parametrisation

$$I = Z \cdot (9.76 + 58.8 Z^{-1.19})\,\mathrm{eV}$$

can be used.

At energies around $E = 30\,\mathrm{MeV}$ the first term dominates. With $E_0 = m_e c^2$ and $v = c$ the equation simplifies to

$$-\left(\frac{dE}{dx}\right)_c = \frac{2\pi e^4 NZ}{E_0} \ln\left(\frac{E_0 E \gamma^2}{2I^2}\right).$$

With $e^2 = 1.44\,\mathrm{MeVfm}$ and for a gold foil the collisional energy loss is about

$$-\left(\frac{dE}{dx}\right)_{\mathrm{c}} \approx 2\,\mathrm{keV}/\mu\mathrm{m}.$$

The Bethe-Møller formula for electrons is based on the Bethe-Bloch formula for charged particles [Bet30, Blo33] and therefore is a description for the average deposited energy and is not useful for the energy loss of single electrons.

Due to the statistical nature of the scattering process, the energy transfer distribution demands to be described by a probability distribution. In thick radiators the energy-loss straggling distribution can be described quite well by a Gaussian distribution. For thin radiators the distribution can be described by *Landau straggling* [Lan44]. It is easy to see that the distribution cannot be symmetric because there is a finite probability to lose any amount of energy from zero up to its incident energy. The Landau distribution (figure 3.2) is characterised by the average energy loss, the most probable energy loss and the full width at half maximum.

Landau straggling has two restrictive assumptions. The binding energy of the electrons should be small compared to the typical energy loss in order to neglect the atomic structure. This is only important for gaseous materials where a parametrised model by Urban [Lass95] can be used. The other approximation is that the maximum energy transfer is considered to be large compared to the typical energy transfer in a single collision. This problem is addressed in the theory of Vavilov [Vav57]. In our case the typical energy loss is several keV with a maximum energy transfer of several MeV, and the Landau theory is sufficient. See [OBri74, Pri55, Cri70] and the Geant4 Physics Manual [G4PM] for review and discussion.

3.1.2 Radiative energy loss

Light charged particles such as electrons predominantly lose energy by radiation at the energies used for the tagging facility, see figure 3.1. For thick radiators the characteristic length traversed in matter is called the *radiation length*. After this distance an electron has lost all but $1/e$ of its energy by bremsstrahlung. A parametrisation is given in [Tsa74]. The radiation length for gold is $X_0 = 3.3\,\mathrm{mm}$. The mean energy loss due to radiation is then

$$-\left(\frac{dE}{dx}\right)_r = E/X_0.$$

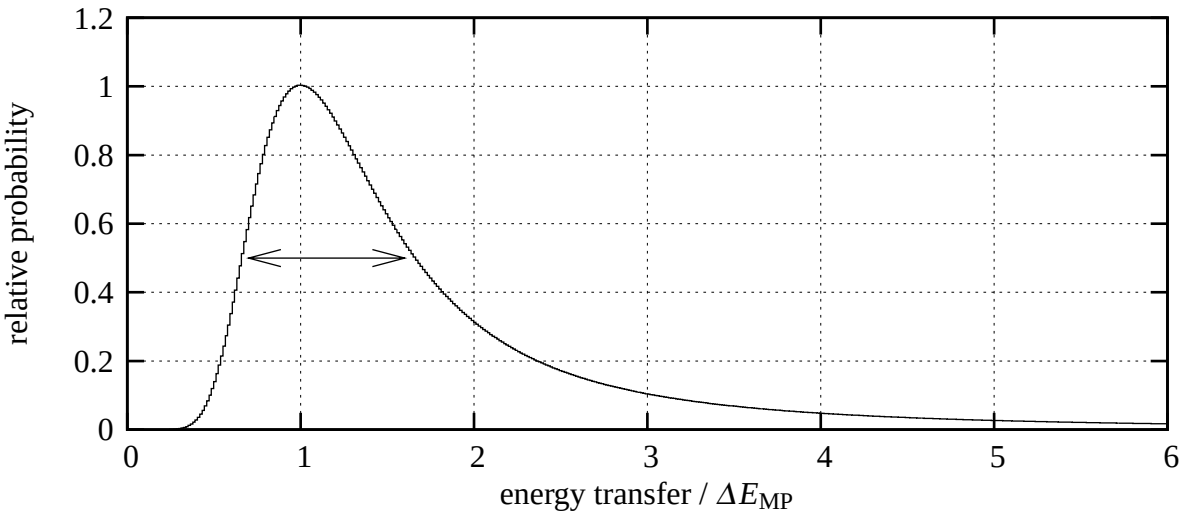

Figure 3.2: The Landau distribution describes the energy-transfer distribution in a thin radiator. The probability is plotted as a function of the energy transfer in units of the most probable energy transfer $\langle \Delta E \rangle$. The distribution is normalised to the maximum. The double-headed arrow denotes the full width at half maximum.

The important information is again not the mean energy loss but rather the energy deposit distribution of a single process because this energy is the energy of the produced photon.

As derived in [Sch51] from the Bethe-Heitler formula [Bet34] the energy spectrum is given by

$$\frac{d\sigma(E)}{dE} = \frac{2\alpha Z^2 r_e^2}{E}\left\{\left(\frac{E_0^2+E_e^2}{E_0^2}-\frac{2E_e}{3E_0}\right)\left(\ln M + 1 - \frac{2}{b}\arctan b\right) + \right.$$
$$\left. + \frac{E_e}{E_0}\left[\frac{2}{b^2}\ln(1+b^2) + \frac{4(2-b^2)}{3b^2}\arctan b - \frac{8}{3b^2} + \frac{2}{9}\right]\right\}$$

where E_0 is the energy of the incident electron, E_e the energy of the degraded electron, $E = E_0 - E_e$ the photon energy,

$$b = \frac{2E_0E_eZ^{\frac{1}{3}}}{111m_ec^2E}$$

and

$$\frac{1}{M} = \left(\frac{m_ec^2E}{2E_0E_e}\right)^2 + \left(\frac{Z^{\frac{1}{3}}}{111}\right)^2.$$

This differential cross section is plotted in figure 3.3 for a incident electron energy of 30 MeV on a gold target. The Bethe-Heitler formula applies for very thin targets in which no other effects occur. Important to notice is the dependence on Z^2 that recommends high-Z materials to get a high yield in produced photons. The heaviest material that can be created in-house in very thin foils is gold, so all subsequent discussion is based on gold as radiator material.

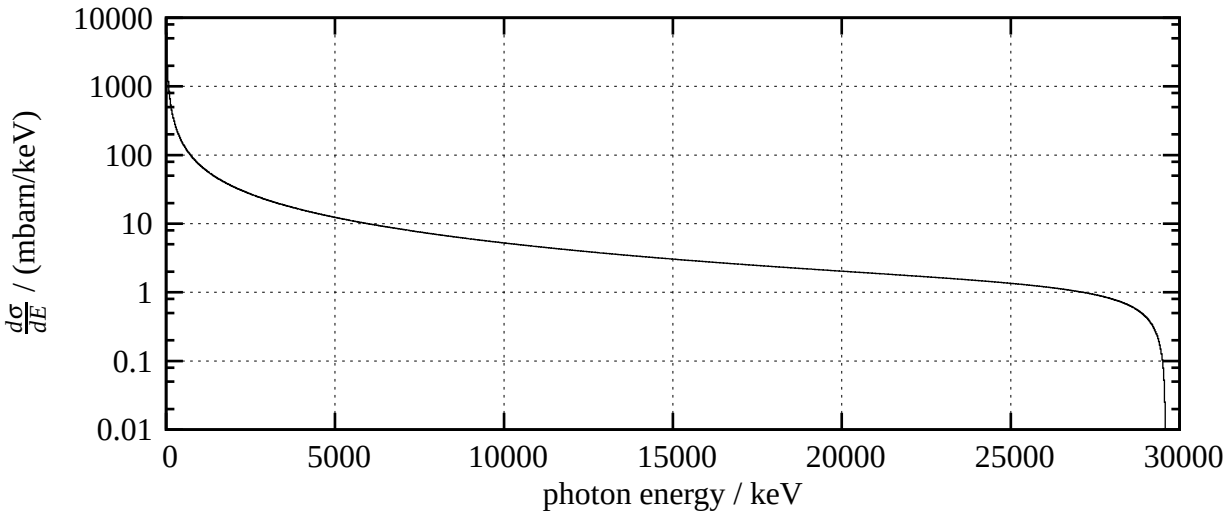

Figure 3.3: The differential cross section of the photon production in a very thin gold target is plotted for the Bethe-Heitler approximation. The incident electron energy is 30 MeV. The end-point energy of the spectrum is the kinetic energy of the electrons. Noticeable is the exponential decrease of the cross section in the middle of the spectrum.

3.1.3 Angular distribution

The angular distribution of the scattered electrons is very important for the required acceptance of the magnetic spectrometer. This in turn affects directly the resolving power and the quality of the tagged photon beam, namely the tagging efficiency as defined before. Large scattering angles require a large acceptance and a large acceptance generally leads to a worse resolving power. To obtain an excellent energy resolution it is possible to choose a smaller acceptance than required with the drawback of a low tagging efficiency. A small acceptance means that a larger amount of scattered electrons is not detected in the focal-plane detector array.

The angular distribution of the photons does not affect the quality of tagging. However, a large scattering angle means a low flux density of the photons, which requires larger targets to cover as much area of the photon beam as possible. This can limit the tagging rate on small targets. If the alternative definition of the tagging efficiency is used, this would result in a lower tagging efficiency.

Electrons

Collisional Coulomb scattering of charged particles with nuclei or atomic electrons leads to deflection by many small angles. At higher energies the scattering with nuclei dominates. The Coulomb scattering distribution is well described by Molière's theory of multiple scattering [Bet53]. The result is that for small deflection angles the distribution has nearly Gauss shape

and for large angles it behaves like Rutherford scattering. For this application it is sufficient to use a Gaussian approximation [Hig75, Hig79, Lyn91, Yao06]. Then the width and mean value are given by

$$\sigma = 37.6\gamma^{-1}\sqrt{d/X_0}\,[1+0.038\ln(d/X_0)]$$

and

$$\langle\vartheta\rangle = \sqrt{2}\sigma,$$

respectively. Here d is thickness of the radiator, the other variables are denoted as before. The accuracy is better than 10 % in the interesting cases.

Photons

The acceleration of charge in relativistic motion can be described within in the scope of classical electrodynamics [Jac98]. In quantum mechanics the classical power distribution turns into a probability distribution for the emission of radiation. Actually, the sharp cut-off at short wave lengths, as shown in figure 3.3, can only be described quantum mechanically, because the energy is quantised in doses of $\hbar\omega$ which form the photons. So the maximum energy of emitted photons is $\hbar\omega = E_0$.

The emission of radiation can be understood easily in the following picture. A moving charge with constant non-relativistic velocity has a slightly condensed electric field in forward direction that can be neglected. So one can imagine an electric field that is moving in space. After an abrupt stop of the charge a new electric field starts propagating with the speed of light c, but the old field is still present at the distance of ct. In the transition region of both fields the field intensity is very high and, most notably, the electric field changes very quickly on so it induces a quickly changing magnetic field. A short electromagnetic wave has been created. From this picture it is clear that no radiation is emitted in direction of the acceleration. At non-relativistic energies the distribution is symmetric about the perpendicular emission direction. At higher energies the emission is peaked toward forward angles.

For linear motion where the deceleration and the motion itself are parallel the distribution of emitted power is

$$\frac{dP}{d\Omega} = \frac{e^2}{4\pi c}\frac{\sin^2\vartheta}{(1-\beta\cos\vartheta)^5}.$$

For highly-relativistic particles ($\beta \to 1$) the angular distribution can be written as

$$\frac{dP}{d\Omega} = \frac{8}{\pi}\frac{e^2\dot{\beta}^2}{c}\gamma^8\frac{(\gamma\vartheta)^2}{(1+(\gamma\vartheta)^2)^5} \tag{3.1}$$

where ϑ is the observation angle with respect to the direction of motion of the incident electron. The shape of the expression evidently depends only on $(\gamma\vartheta)^2$ and with

$$\int_0^\infty \frac{x^2}{(1+x^2)^5}dx = \frac{5\pi}{2^8},$$

the probability distribution of the scattering angle follows as

$$\frac{dP(x)}{dx} = \frac{2^8 x^2}{5\pi(1+x^2)^5} \tag{3.2}$$

with x as the scattering angle in units of γ^{-1}. It is plotted in figure 3.4.

The *characteristic angle* of bremsstrahlung photons is the root mean square angle of this relativistic limit given by

$$\vartheta_{\text{char}} = \sqrt{\langle \vartheta^2 \rangle} = \frac{1}{\gamma} = E_0/E$$

With *every* change of velocity in magnitude or direction, the classical electromagnetic theory incorrectly predicts the emission of bremsstrahlung. In quantum mechanics the *power distribution* (equation (3.1)) turns into a probability distribution. The probability distribution above (equation (3.2)) is normalised to the probability that a photon is emitted in the electron scattering process. The probability of photon emission is on the order of the fine structure constant compared to elastic scattering.

In reality multiple scattering and emission of radiation are superposed. Because the desired process is the emission of radiation the electrons perform about $1/\alpha$ additional scattering processes, where α is the fine structure constant. The handling of all processes is done most easily by Monte-Carlo simulations.

3.2 Geant4

Geant4 (for GEometry ANd Tracking)[Ago03, All06] is a C++ library that covers all the main aspects for an accurate simulation of the passage of particles through matter. In detail these aspects are the geometry of the system, the materials involved, the fundamental particles of interest, the generation of primary events, the tracking of particles through materials and electromagnetic fields, the physics processes governing particle interactions, the response of sensitive detector components, the generation of event data, the storage of events and tracks, the visualization of the detector and particle trajectories, and the capture and analysis of simulation data at different levels of detail and refinement. Nearly all the mentioned items have been used for simulating the scattering process in the radiator, the electron paths in the magnetic field and all the interactions in the beam dump.

Besides theoretical descriptions of the interactions Geant4 uses experimental data tables and parametrisations to process the interactions of the particles in the simulation. The interaction of electrons with different materials and thicknesses has been simulated. The thickness of each material was ranged from $0.01\,\% \cdot X_0$ to $10.24\,\% \cdot X_0$ in steps of a factor two. In the following only gold, nickel and aluminium are considered as representatives for materials with high Z, medium Z and low Z.

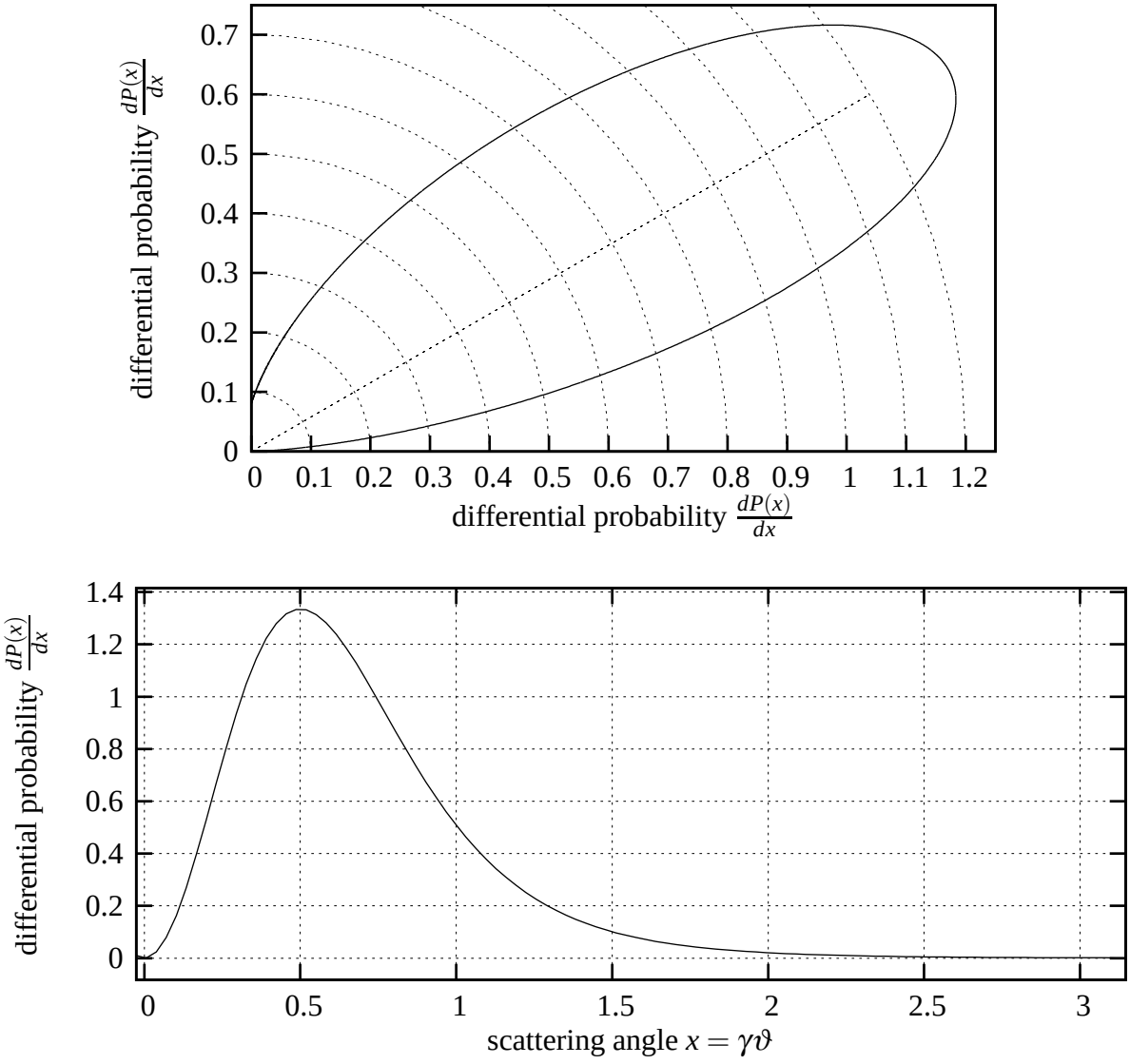

Figure 3.4: The upper picture shows the differential emission probability $dP(x)/dx$ for incoming relativistic electrons in polar coordinates and the lower picture the same linearly as a function of the scattering angle $x = \gamma\vartheta$. The maximum is at $\vartheta = (2\gamma)^{-1}$ and the mean value is at $\vartheta = \gamma^{-1}$.

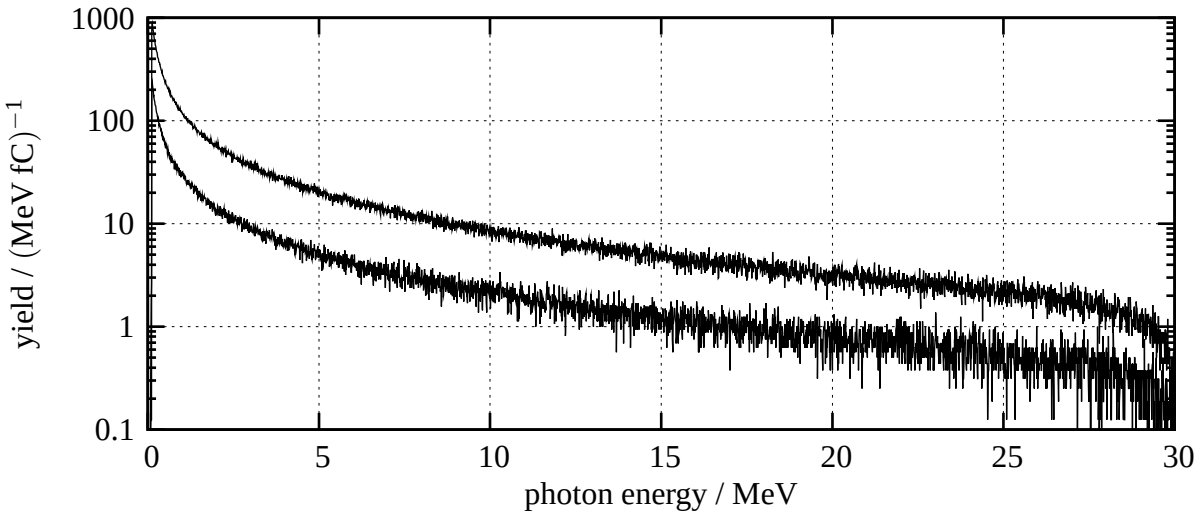

Figure 3.5: Energy spectrum of the produced photons for gold and two different thicknesses of $0.32\,\% \cdot X_0$ (lower spectrum) and $1.28\,\% \cdot X_0$ (upper spectrum). The yield is normalised to fC and MeV.

3.2.1 Production properties of the photons

The typical energy of the incoming electron beam is 30 MeV. This energy is used to analyse the production of photons with Monte-Carlo simulations, in order to determine the production efficiency, the energy distribution and the scattering angle.

The energy distribution of the photons produced in gold with two different thickness is plotted in figure 3.5 in a logarithmic scale. For thin targets the yield scales linearly with the thicknesses and has the same shape for different materials.

Figure 3.6 shows the dependence of the yield on the thickness for three different materials. The yield for a thickness of $0.32\% \cdot X_0$ is about 20 % higher for gold (upper curve) than for aluminium (lower curve). This weak dependence is ascribed to the normalisation to the radiation length.

An electron may produce more than one photon during its way through the target, so-called higher-order photons. For a tagging facility one is only interested in first-order photon production. With higher-order photons the energy of both, first order and higher-order photon cannot be determined unambiguously, so the fraction of higher-order photons should be very low. Higher-order photons with energies below 5 keV can be neglected, because this is below the desired energy resolution. For different materials the fraction of higher-order photons is shown in figure 3.7. To get a high tagging efficiency, the ratio should not exceed a value of one percent. As found in the figure, the ratio is much higher for aluminium than for gold at the same thickness. This militates clearly in favour of high-Z materials such as gold. Therefore, the desired thickness is about $0.3\,\% \cdot X_0$. The expected photon production rate is about

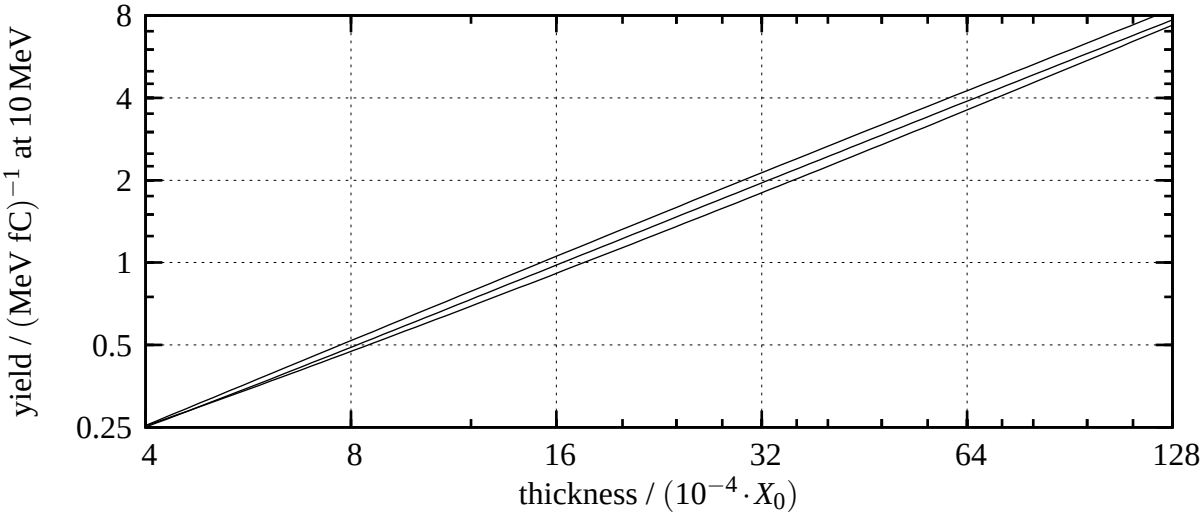

Figure 3.6: The yield for 10-MeV photons as a function of the thickness for three different material. The upper curve is gold, the lower curve is aluminium and the middle curve is nickel. The yield is normalised to MeV and fC.

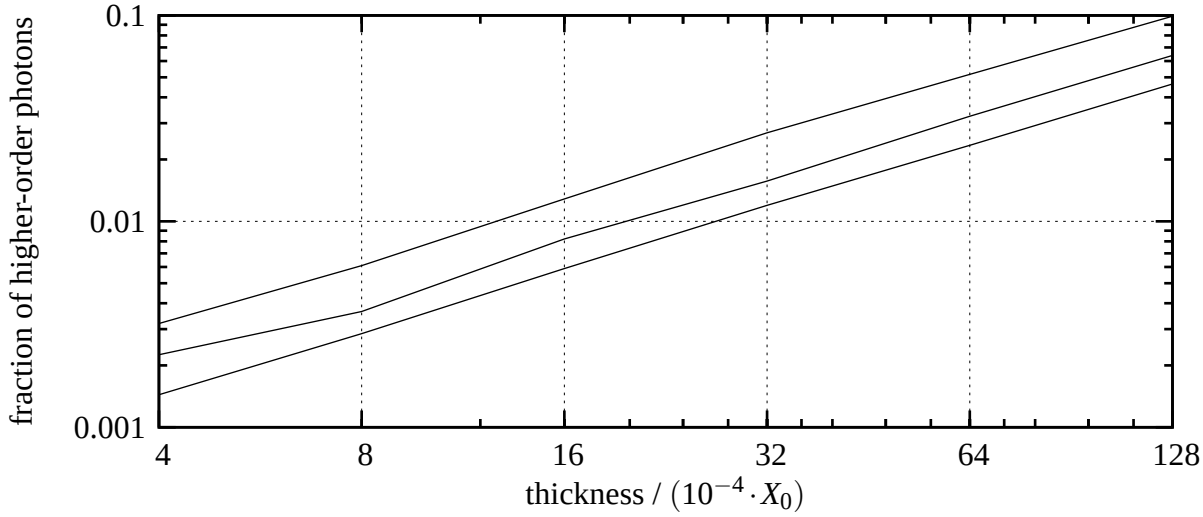

Figure 3.7: The ratio of higher-order photons to all produced photons is shown for different thickness of gold (lower curve), nickel (middle curve) and aluminium (upper curve). The kinks in curves stem from low statistics. The calculated points are at the vertical dotted lines.

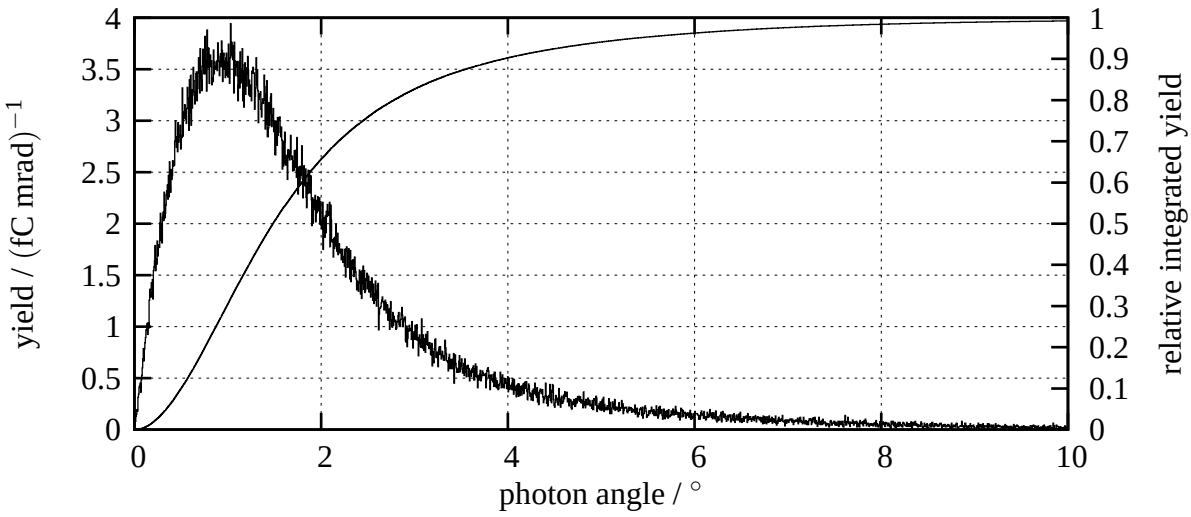

Figure 3.8: The angular distribution of the produced photons for gold at 0.32 % radiations length. The left axis of ordinates shows the differential spectrum normalised to fC and mrad. The right axis shows the relative angular-integrated yield. The most probable angle is 1° and the median is at 1.5°.

$2\,/(\mathrm{MeV}\cdot\mathrm{fC}) = 0.2\cdot 10^4\,/(\mathrm{s}\cdot\mathrm{nA}\cdot\mathrm{keV})$.

Figure 3.8 shows the angular distribution of the produced photons for gold with a 0.32 % radiation length. The most probable angle is at 1° and the median is at 1.5°. 90 % are within the large angle of 4°. For example, at a distance of 3 m from the radiator and a target radius of 3 cm a ratio of 13 % of all photons is covered.

In figure 3.9 the angular distribution of the produced photons is compared for three materials. The angles should be as small as possible to obtain a high photon density and a high tagged photon rate at the experimental site. The distribution does not change much for different materials and tends to be broader for lighter materials. The reason for this is the normalisation to the radiation length.

3.2.2 Properties of the scattered electrons

To produce photons with an energy of 10 MeV an electron beam of 30 MeV is chosen and the energy of the degraded electron is 20 MeV. The electron passes the radiator with the full energy until a photon is emitted and then leaves the radiator with the decreases energy. From the discussion above a lower limit can be assumed by choosing the low energy for the simulations.

To examine the scattering properties by a Monte-Carlo method, the energy loss of the incoming electron was exactly 20 MeV. It would consume too much compute time to simulate the full process that would require the simulation of a 30 MeV electron beam hitting a target and considering only those electrons that have emitted a photon. The two important properties

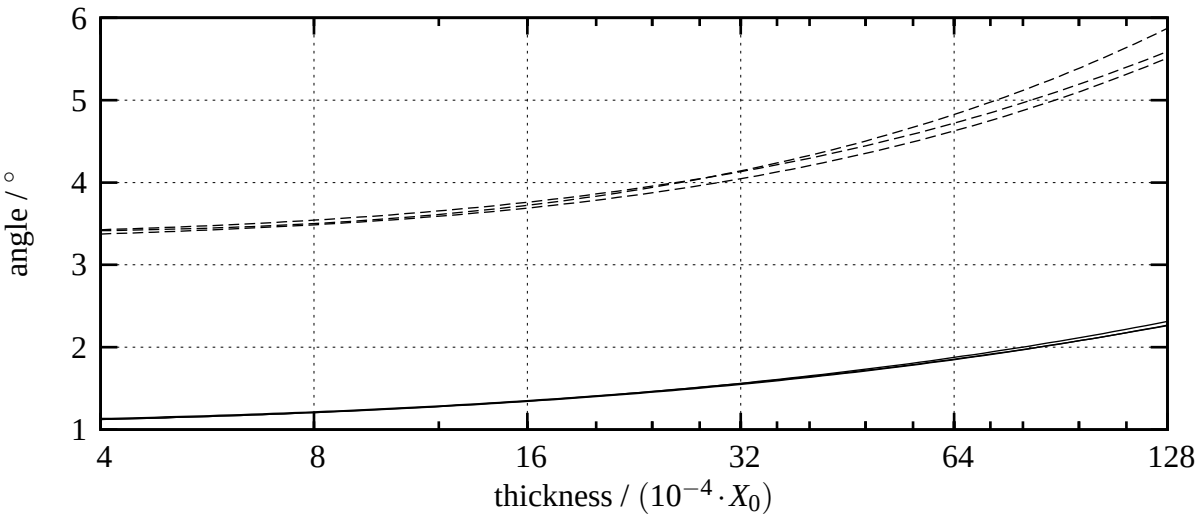

Figure 3.9: The angular distribution of the produced photons as a function of thickness and three different materials. The lower solid lines denote the median of the distribution and the upper dashed lines are for the 90-% limit. Shown are again gold (lower curve), aluminium (upper curve) and nickel. The angle is not influenced much by the choice of material. A slightly broader distribution is produced by lighter thick materials.

needed for the specification of the tagging facility are the energy spread and the scattering angle. Materials with different Z and thicknesses have been simulated.

Figure 3.10 shows a typical energy-loss spectrum of monoenergetic electrons after hitting a thin target. The energy loss and the energy spread of different materials with different thicknesses are shown in figure 3.11. The full width at half maximum contains about 65 % of all events for this energy distribution. Plotted is the width where 80 % of all events are contained. The energy spread due to straggling has to be as low as possible. To obtain a resolution of 25 keV, this requires very thin targets. The maximum value for gold is about $0.32\,\% \cdot X_0$ and for aluminium $0.10\,\% \cdot X_0$.

In figure 3.12 a typical angular distribution is shown. This defines the needed angular acceptance of the spectrometer. For a quantification a value θ_{90} is defined that describes the angle which contains the scattering angles of 90 % of all electrons. This is plotted for different materials in figure 3.13. The angular distribution does not depend strongly on the material. For all materials the 90-% limit is around 4° at a thickness of $0.32\,\% \cdot X_0$.

Finally in figure 3.14 the energy dependence of angular distribution is given for gold with a thickness of $0.32\,\% \cdot X_0$ for scattering energies from 8 MeV to 20 MeV. With less energy the scattering angles get larger which leads to a worse energy resolution of the tagging system, as discussed in the next chapter. Nevertheless, the application is still possible without any other disadvantages. The energy loss in absolute units in the target is the same for all the energies.

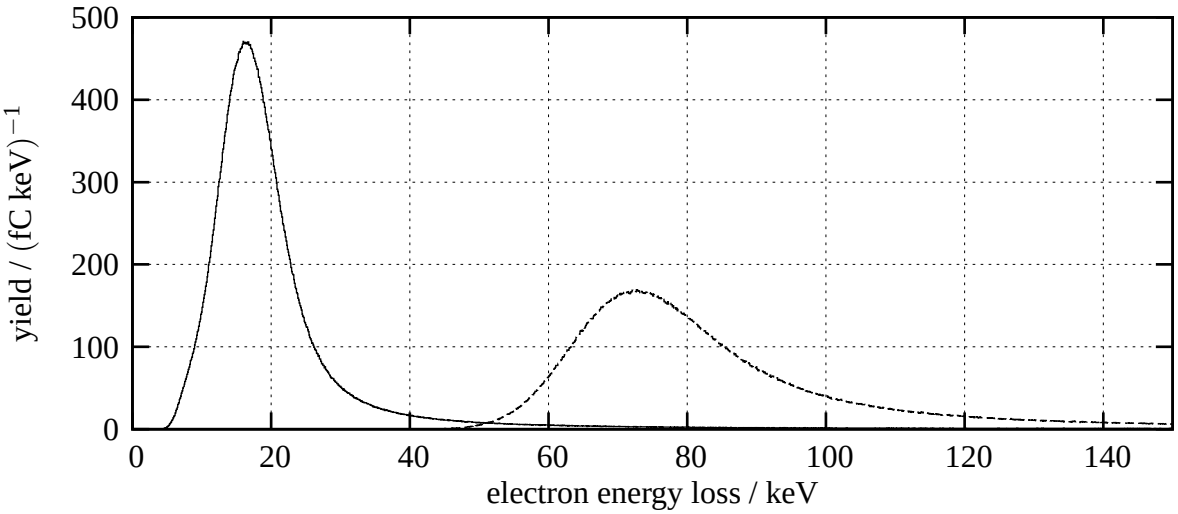

Figure 3.10: The energy-loss spectrum of an electron beam with an energy of 20 MeV hitting a gold target with a thickness of $0.32\,\% \cdot X_0$, the solid line, and $1.28\,\% \cdot X_0$, the dashed line. The energy spread (FWHM) is 11 keV (26.5 keV for the thicker target) that affects the energy resolution of the tagging facility. The energy loss is about 16.5 keV (72 keV for the thicker target).

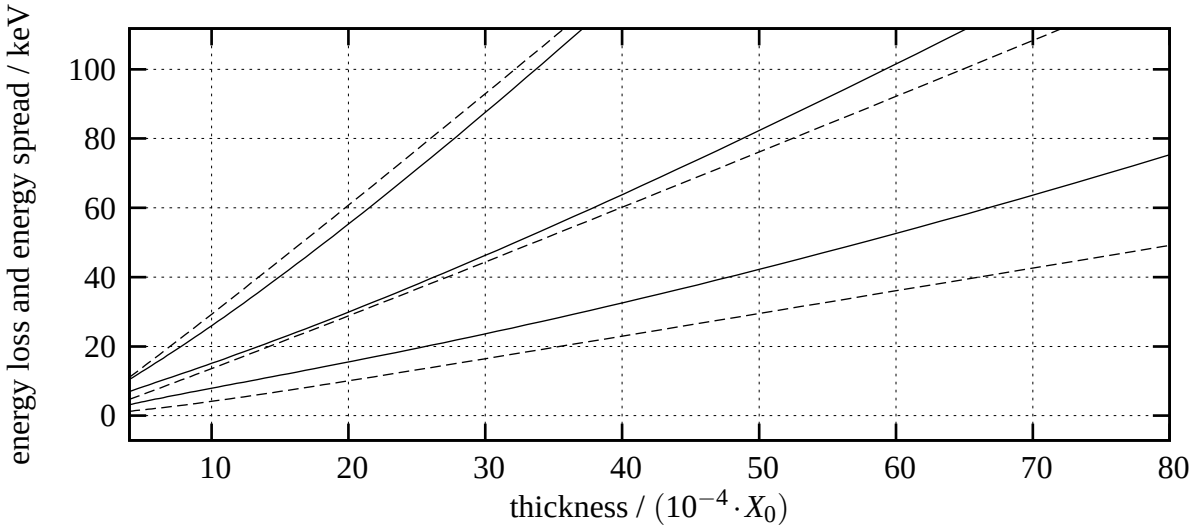

Figure 3.11: The energy spread is plotted as solid lines and the median energy loss as dashed lines for three different materials: gold (lower curves), aluminium (upper curves) and nickel (middle curves). The energy spread is the width that contains 80 % of all events.

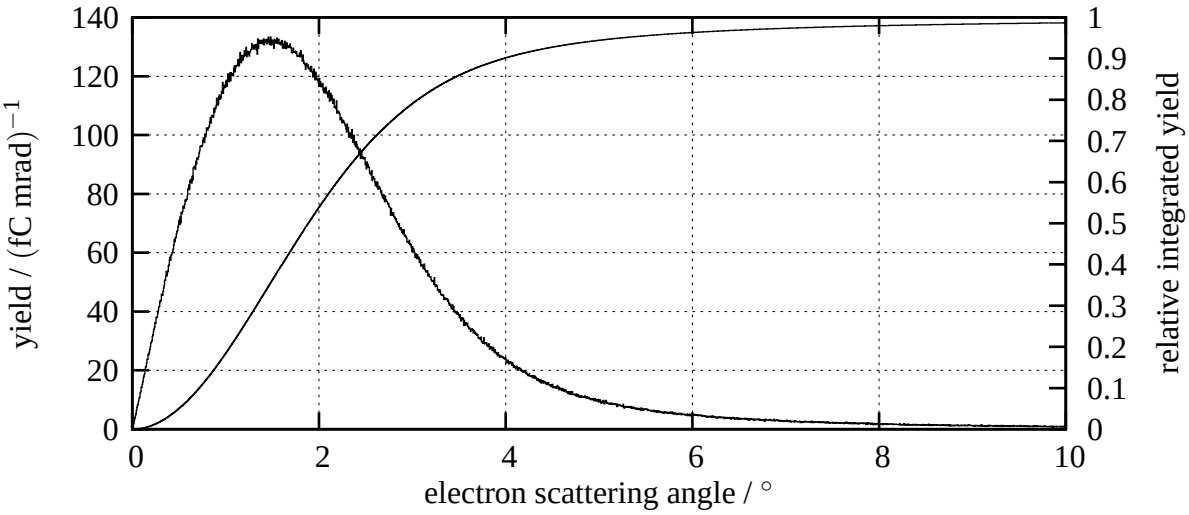

Figure 3.12: The angular distribution of an electron beam with an energy of 20 MeV hitting a gold target with a thickness of $0.32\,\% \cdot X_0$. Remarkable are the large angles that define the acceptance of the magnet. Here 90 % of the electrons are scattered at angles smaller than 4°.

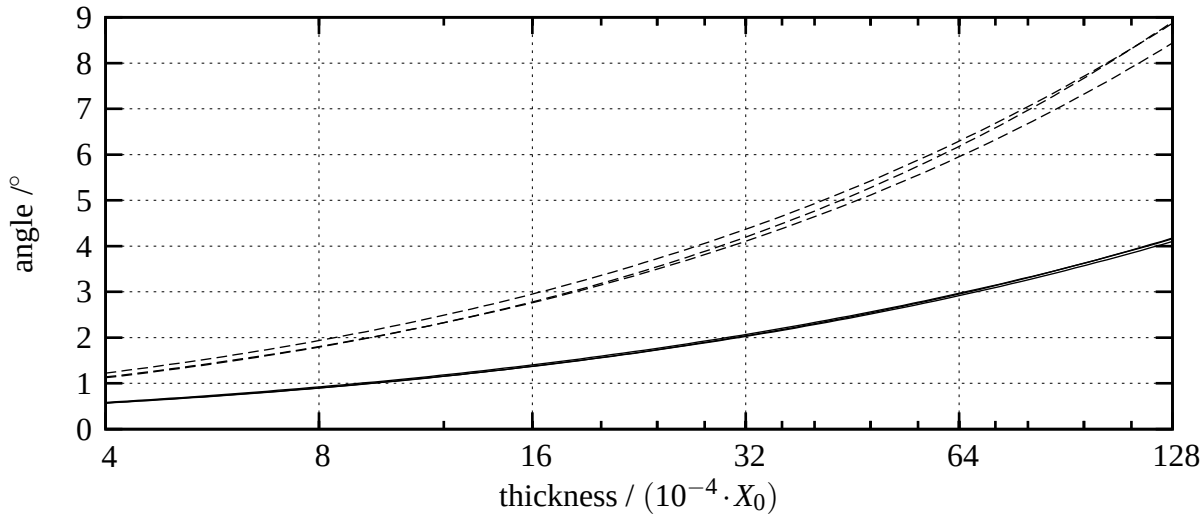

Figure 3.13: The angular distribution of the scattered electrons for different thicknesses and three materials. The lower solid lines denote the median of the distribution and the upper dashed lines are for the 90-% limit. Shown are again gold (lower curve), aluminium (upper curve) and nickel. The angle is not influenced much by the choice of material.

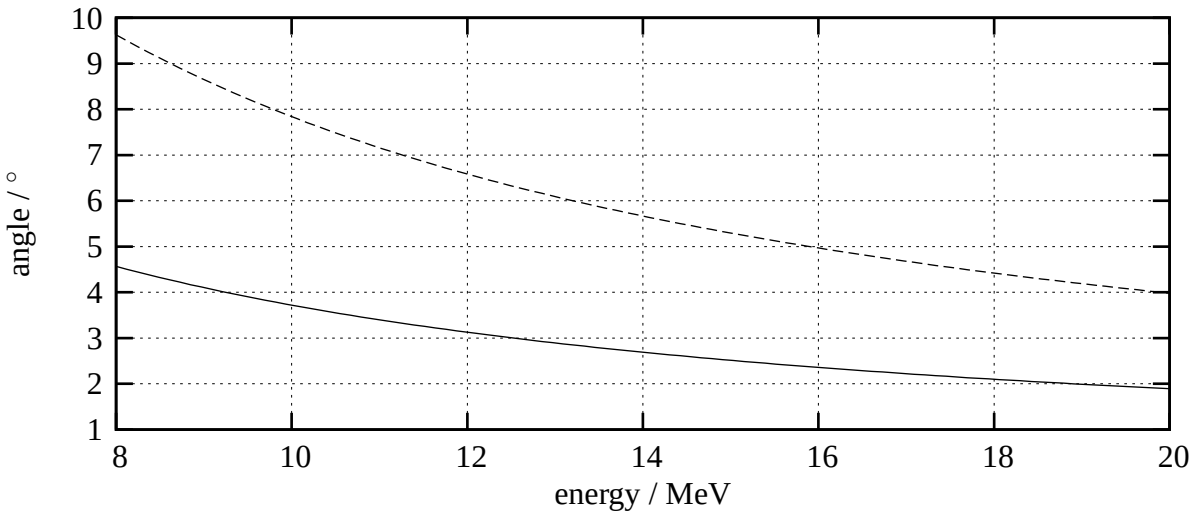

Figure 3.14: For smaller scattering energies the scattering angles increase. Shown are the median scattering angle (solid line) and the 90-% limit (dashed line) for a gold target with $0.32\,\% \cdot X_0$.

3.3 Specification for the target

From the theoretical discussion and the simulations of the last two sections, a high-Z material such as gold is favoured to be chosen as radiator material. The thickness should be about 0.3 % of the radiation length which is 3.3 mm for gold. This results in an absolute thickness of 10 μm. Gold targets with different thicknesses have been produced by vaporisation in the detector laboratory of the institute for nuclear physics at TU Darmstadt. The thickness has been measured by the energy loss of scattered α particles.

For this thickness the photon production yield at 10 MeV is 2 $(\mathrm{MeVfC})^{-1}$ and the fraction of higher-order photons is about 1 %. The median photon angle is 1.5° and 90 % are contained within an angle 4°.

The mean energy loss and the energy spread (80 %) of the degraded electrons are both about 20 keV. More than 90 % of the electrons are scattered within an angle of 4°.

4 Design of the magnet

As shown in the previous chapter, the electron scattering angles are very large. To obtain a high tagging efficiency the acceptance of the magnetic spectrometer has to be sufficiently large, as well. In 1946 Richardson [Ric47] described a simple magnetic design with large acceptance for β-ray spectroscopy. This design has been used for some other spectrometers, especially for tagging spectrometers, e.g. [Kno82, Adl90]. The final design is shown by the CAD drawings in appendix A.

4.1 Geometry

The geometry simply consists of two inclined plane pole faces. In the approximation of infinite equipotential planes, the field is the same as that from a straight current flowing along the line of intersection of the two planes. The magnetic field lines form arcs of circles around the line of intersection as shown in figure 4.1. The figure shows the geometry of the magnetic spectrometer. Disregarding the fringe field in front of the magnet all electrons, regardless of their scattering angle, are bent back and focussed in the line of intersection, where the scattering occurred. The magnetic field strength decreases with $1/r$.

The magnetic field is piecewise cylindrically symmetric about the line of intersection. Because the physical magnetic field does not have a sharp cut-off at the pole boundaries, this symmetry is not valid in an exact analysis. The fringe field at the end of the magnet (right side of figure 4.1) can be moved to a region where no electron orbits are. The fringe field in the

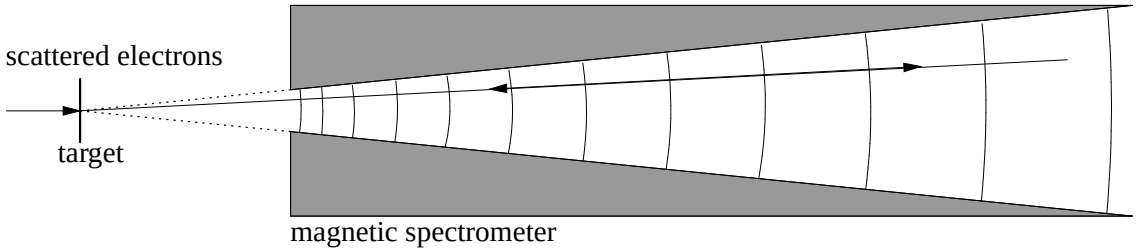

Figure 4.1: The electron is scattered in the radiator target with large angles. The electrons cross perpendicularly the magnetic field lines inside the spectrometer and all electrons are kept on a plane that contains the line of intersection.

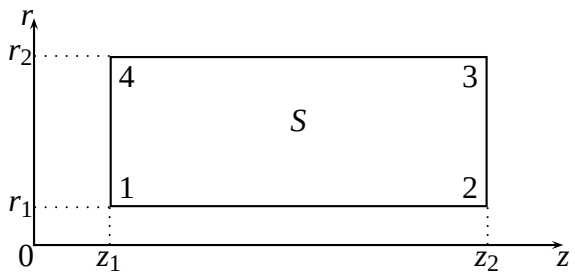

Figure 4.2: Shown is a rectangular with the area S lying in an equipotential plane between two inclined pole faces. The coordinates z and r are the cylindrical coordinates of the symmetry.

beginning can be reduced with passive or active magnetic shielding.

4.2 Focusing properties of inclined pole faces

First in this section the focusing properties of inclined pole faces are discussed and then extended by a region without magnetic field around the line of intersection. Due to the cylindrical symmetry, cylindrical coordinates (z, r, φ) are used, where r is the distance to the line of intersection, φ the angle to the symmetry plane (mid-plane) and z the distance parallel to the line of intersection. The origin is chosen to be at the point of emission. For this geometry the magnetic induction satisfies

$$\mathbf{B} = \frac{B_0}{r^2}(\mathbf{r} \times \mathbf{z})$$

where B_0 is the induction at $r = 1$. The field vector $\mathbf{B}$ can be expressed by the vector potential $\mathbf{A}$

$$\mathbf{B} = \nabla \times \mathbf{A}$$

and Stokes' theorem applies to obtain

$$\int_S \mathbf{B} d\sigma = \oint_C \mathbf{A} d\mathbf{s}$$

with the area element $d\sigma$ and the path element $d\mathbf{s}$.

For the integration a rectangular area S with the surrounding path C lying in an equipotential plane with the sides parallel to z and r, respectively, is defined. The coordinates are $P_1(z_1, r_1)$, $P_2(z_2, r_1)$, $P_3(z_2, r_2)$ and $P_4(z_1, r_2)$. In this symmetry $\mathbf{A}$ reduces to one component parallel to the z-axis and only depends on r. For Stokes' theorem follows that

$$B_0 \int_{z_1}^{z_2} \int_{r_1}^{r_2} \frac{1}{r} dr dz = \int_{z_1}^{z_2} A(r_1) dz + \int_{r_1}^{r_2} A(r) dr + \int_{z_2}^{z_1} A(r_2) dz + \int_{r_2}^{r_1} A(r) dr.$$

On the right hand side the integrals of all four straight paths are given. The second and the fourth integral cancel out and $A(r_{1,2})$ are constant.

$$B_0 \ln\frac{r_2}{r_1}\int_{z_1}^{z_2} dz = A(r_1)(z_2-z_1)+A(r_2)(z_1-z_2)$$
$$B_0 \ln\frac{r_2}{r_1}(z_2-z_1) = [A(r_1)-A(r_2)]\,(z_2-z_1)$$

From $S>0$ follows $z_1 \neq z_2$ and with the boundary condition $A(e)=0$ one obtains the simple equation

$$A(r) = B_0(1-\ln r)$$

where **A** is parallel to **z**.

This can be used to calculate the relativistic equations of the electron orbits. From standard literature [Gre92] the relativistic Lagrangian for a particle moving in static magnetic fields is

$$L = (1-\gamma^{-1})mc^2 + q(\mathbf{Av})$$

where $q=e$ and $v=\sqrt{\dot r^2+\dot z^2+r^2\dot\varphi^2}$. With the vector potential derived above inserted,

$$L = (1-\gamma^{-1})mc^2 + B_0 e\dot z(1-\ln r),$$

the momenta can be calculated. The needed partial derivatives of

$$\gamma^{-1} = \sqrt{1-\frac{v^2}{c^2}} \quad \text{with} \quad v^2 = \dot r^2+\dot z^2+r^2\dot\varphi^2$$

are

$$\frac{\partial\gamma^{-1}}{\partial\dot\varphi} = -\frac{\gamma}{c^2}r^2\dot\varphi \qquad \frac{\partial\gamma^{-1}}{\partial\varphi} = 0$$
$$\frac{\partial\gamma^{-1}}{\partial\dot r} = -\frac{\gamma}{c^2}\dot r \qquad \frac{\partial\gamma^{-1}}{\partial r} = -\frac{\gamma}{c^2}r\dot\varphi^2$$
$$\frac{\partial\gamma^{-1}}{\partial\dot z} = -\frac{\gamma}{c^2}\dot z \qquad \frac{\partial\gamma^{-1}}{\partial z} = 0$$

The angular momentum is a constant of the motion

$$p_\varphi = \frac{\partial L}{\partial\dot\varphi} = \gamma m r^2\dot\varphi, \quad \frac{\partial L}{\partial\varphi} = 0$$
$$0 = \frac{\partial L}{\partial\varphi} = \frac{d}{dt}\left(\frac{\partial L}{\partial\dot\varphi}\right) = \frac{d}{dt}\left(p_\varphi\right)$$
$$\Rightarrow p_\varphi = \gamma m r^2\dot\varphi = \text{const}$$

The equations of motion are obtained from the other variables

$$\frac{\partial L}{\partial \dot{r}} = \gamma m \dot{r}, \quad \frac{\partial L}{\partial r} = \gamma m r \dot{\varphi}^2 - eB_0 \frac{\dot{z}}{r}$$

$$\frac{d}{dt}\left(\frac{\partial L}{\partial \dot{r}}\right) = \frac{\partial L}{\partial r} \Rightarrow \ddot{r} = -\frac{B_0 e}{\gamma m}\frac{\dot{z}}{r} + \frac{1}{\gamma^2 m^2}\frac{p_\varphi^2}{r^3} \tag{4.1}$$

and

$$\frac{\partial L}{\partial \dot{z}} = \gamma m \dot{z} + B_0 e(1 - \ln r), \quad \frac{\partial L}{\partial z} = 0$$

$$\frac{d}{dt}\left(\frac{\partial L}{\partial \dot{z}}\right) = \frac{\partial L}{\partial z} \Rightarrow \ddot{z} = \frac{B_0 e}{\gamma m}\frac{\dot{r}}{r}$$

$$\Rightarrow \dot{z} = \frac{B_0 e}{\gamma m}\ln r + C. \tag{4.2}$$

The constant C is chosen to satisfy $\dot{z}(R) = 0$, when

$$C = -\frac{B_0 e}{\gamma m}\ln R.$$

Now $\dot{z}$ can be inserted into the expression for $\ddot{r}$, equation (4.1).

$$\ddot{r} = -\frac{B_0^2 e^2}{\gamma^2 m^2}\frac{1}{r}\ln\frac{r}{R} + \frac{p_\varphi^2}{\gamma^2 m^2}\frac{1}{r^3}$$

and the integration of both sides with respect to r

$$\int \ddot{r} dr = -\frac{B_0^2 e^2}{\gamma^2 m^2}\int \frac{1}{r}\ln\frac{r}{R} dr + \frac{p_\varphi^2}{\gamma^2 m^2}\int \frac{1}{r^3} dr$$

provides

$$\frac{\dot{r}^2}{2} = -\frac{1}{2}\underbrace{\left(\frac{B_0 e}{\gamma m}\ln\frac{r}{R}\right)^2}_{\dot{z}^2} - \frac{1}{2}\underbrace{\left(\frac{p_\varphi}{\gamma m r}\right)^2}_{r^2\dot{\varphi}^2} + \frac{1}{2}C'$$

with the shown identification

$$C' = \dot{r}^2 + \dot{z}^2 + r^2\dot{\varphi}^2 = v^2.$$

Using the abbreviations

$$K = \frac{\gamma m v}{B_0 e} \quad \text{and} \quad a = \frac{p_\varphi}{\gamma m v} \tag{4.3}$$

for $\dot{r}$ it follows that

$$\dot{r} = \pm v\sqrt{1 - \left(\frac{a}{r}\right)^2 - \left(\frac{1}{K}\ln\frac{r}{R}\right)^2}.$$

It is convenient to express the coordinates in terms of the angle between the direction of motion and the line of intersection ψ as

$$\cos\psi = \frac{\dot{z}}{v}.$$

Then from equation (4.2) it follows

$$v\cos\psi = \frac{v}{K}\ln\frac{r}{R} \Rightarrow r = Re^{K\cos\psi}. \tag{4.4}$$

This is the equation of motion for r for the parameter ψ.

For $z(\psi)$ one can write

$$z = \int dz = \int \frac{dz}{dt}\frac{dt}{dr}\frac{dr}{d\psi}d\psi$$

with the factors

$$\begin{aligned}
\frac{dz}{dt} = \quad \dot{z} \quad &= v\cos\psi \\
\frac{dt}{dr} = \quad \dot{r}^{-1} \quad &= \left[\pm v\sqrt{1-\left(\frac{a}{r}\right)^2 - \left(\frac{1}{K}\ln\frac{r}{R}\right)^2}\right]^{-1} = \\
&= \left[\pm v\sqrt{\sin^2\psi - \left(\frac{a}{Re^{K\cos\psi}}\right)^2}\right]^{-1} \\
\frac{dr}{d\psi} \quad &= -RKe^{K\cos\psi}\sin\psi.
\end{aligned}$$

This results in

$$z = \mp RK\int \frac{e^{K\cos\psi}\cos\psi}{\sqrt{1-\left(\frac{a}{R\sin\psi e^{K\cos\psi}}\right)^2}}d\psi. \tag{4.5}$$

And $\varphi(\psi)$ can be written as

$$\varphi = \int \dot{\varphi}\frac{dt}{dr}\frac{dr}{d\psi}d\psi.$$

With $\dot{\varphi} = \frac{p_\varphi}{\gamma m r^2}$ and the derivatives from above one obtains

$$\varphi = \mp\frac{aK}{R}\int \frac{e^{-K\cos\psi}}{\sqrt{1-\left(\frac{a}{R\sin\psi e^{K\cos\psi}}\right)^2}}d\psi. \tag{4.6}$$

Without loss of generality, let the source of emission lie at $P_S(r = r_s, z = 0, \varphi = 0)$ and the emission angles $\psi = \psi_s$ and $\xi = \xi_s$. The quantity ξ is the angle to the meridional plane ($\varphi =$ const). It can be expressed by the angular momentum and the momentum in the r direction, as

$$\frac{p_\varphi/r}{\gamma m v} = \frac{a}{r} = \sin\xi \Rightarrow a = r_s\sin\xi_s.$$

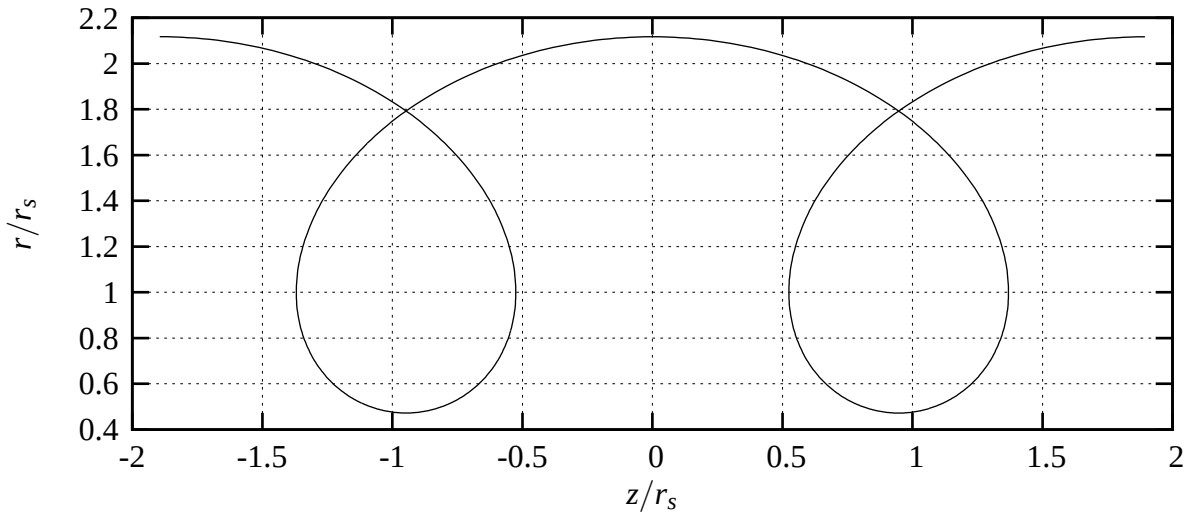

Figure 4.3: Shown are the electron orbits described by equations (4.11), (4.12) and (4.13). Here ψ_s is set to $\pi/2$ and K to the special value of 0.75, as described later. The relevant region is $r/r_s \geq 1$ where the electrons enter the magnet perpendicularly.

From equation (4.4) the parameter R, which satisfies $\dot{z}(R) = 0$, can be expressed by

$$R = r_s e^{-K\cos\xi_s}.$$

Finally, the resulting orbits are calculated by

$$r = r_s e^{K(\cos\psi - \cos\psi_s)} \tag{4.7}$$

$$z = \mp K r_s e^{-K\cos\psi_s} \int \frac{\exp(K\cos\psi)\cos\psi}{\sqrt{1-\left(\frac{\sin\xi_s}{\sin\psi}\right)^2 \exp[-2K(\cos\psi-\cos\psi_s)]}} d\psi \tag{4.8}$$

$$\varphi = \mp K \sin\xi_s e^{K\cos\psi_s} \int \frac{\exp(-K\cos\psi)}{\sqrt{1-\left(\frac{\sin\xi_s}{\sin\psi}\right)^2 \exp[-2K(\cos\psi-\cos\psi_s)]}} d\psi \tag{4.9}$$

where $K = \frac{\gamma m v}{B_0 e}$ or

$$p = K \cdot eB_0 \tag{4.10}$$

is a dimensionless constant which describes physical conditions for the spectrometry, B_0 is the magnetic induction at $r/r_s = 1$ and $\gamma m v$ as the momentum of the electron. For a homogeneous magnetic field $K = r$, which can be derived easily from the combination of centrifugal force and Lorentz force $\gamma m v^2/r = evB$. These equations are parametrised by the angle ψ between the particle's momentum and the z axis. The initial parameters at the source are r_s, ψ_s and ξ_s.

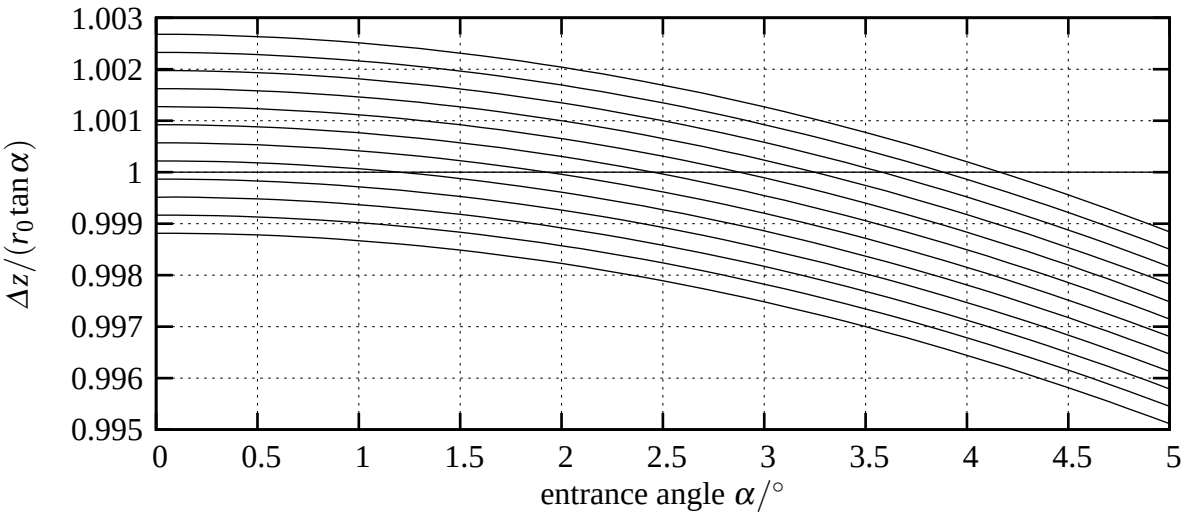

Figure 4.4: Both sides of equation (4.14) are plotted for graphical analysis. The set of curves depends on the parameter K. The lowest curve is for $K = 0.7420$ and the top curve for $K = 0.7431$. The difference in K from one curve to the next is $\Delta K = 0.001$.

4.2.1 Relevant orbits for the spectrometer

As shown before, the source of emission lies in the line of intersection of the inclined planes. With the assumption of the no-field region in front of the magnet, all electron orbits lie in planes that are equivalent to the mid-plane, so $\xi_s = 0$. The electron orbits start at the entrance of the magnet at r_0, so $r_s = r_0$. In this special case the equations of motion (equations (4.7)), (4.8) and (4.9)) simplify to

$$r = r_0 e^{K(\cos\psi - \cos\psi_s)} \tag{4.11}$$

$$z = \mp K r_0 e^{-K\cos\psi_s} \int_0^{\psi} \cos\psi' e^{(K\cos\psi')} d\psi' \tag{4.12}$$

$$\varphi = 0. \tag{4.13}$$

As expected the angle φ to the mid-plane always remains zero. The orbits have been tabulated by means of the c library gsl [gsl06] and plotted in figure 4.3.

The plot shows the orbits in the mid-plane for infinite pole faces. The symmetry about the $z = 0$ axis is used to get an image at $z = z_0$ of the source at $z = -z_0$. Since the spectrometer starts at a distance r_0 from the source as shown in figure 4.1 the electrons first follow a straight line to the magnet and enter the field in different angles α. This gives a small shift in z. The condition for the focus is

$$\Delta z(\alpha) \stackrel{!}{=} r_0 \tan\alpha$$

if the symmetry about $z = 0$ should be kept. This condition holds for the source and for the

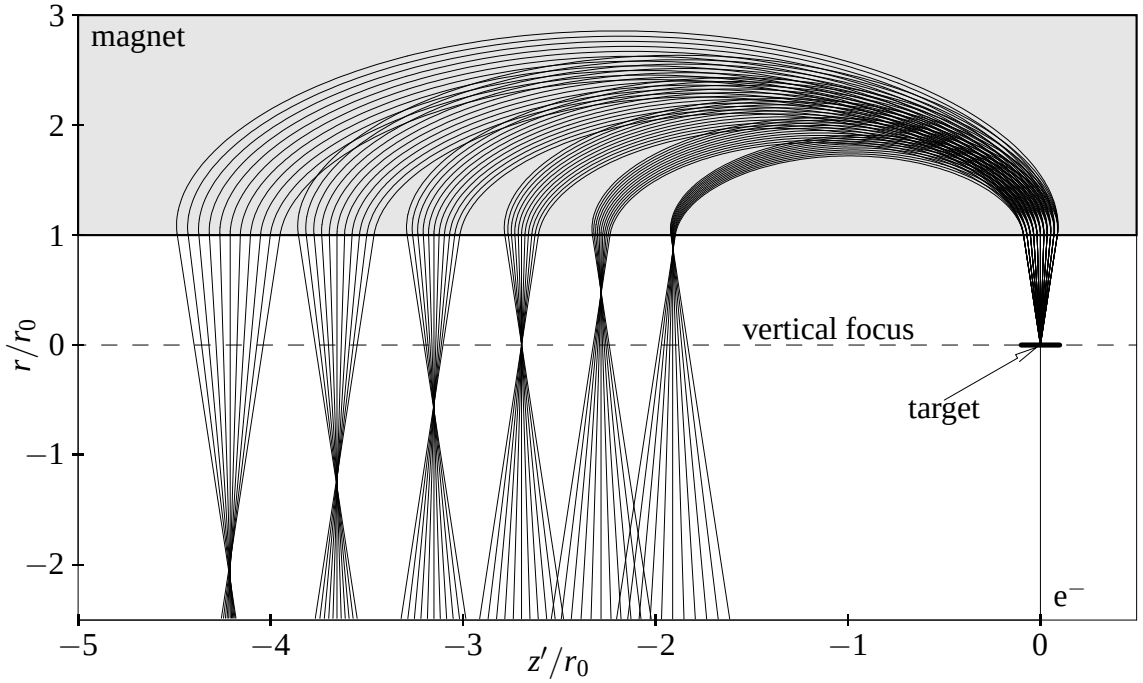

Figure 4.5: The equations of motion (4.11) and (4.15) are plotted in the shaded area denoted as *magnet*. Outside the magnet the electron orbits are plotted as straight lines with the corresponding boundary conditions. At $r = 0$ the vertical focus is indicated with a dashed line, the target is located at $r = 0$ and $z = 0$ where the electrons are scattered. Plotted are five different values of K, from $0.8K_0$ to $1.3K_0$ with $K_0 = 0.7426$.

image. Then, the shift in z can be expressed by

$$\Delta z = z(\psi_s = \pi/2) - z(\psi_s = \pi/2 - \alpha)$$

and with the abbreviation

$$I(\psi, K) = \int_0^{\psi} \cos\psi' e^{K\cos\psi'} d\psi'$$

the focus condition is

$$\mp \frac{K}{\tan\alpha} \left(I(\pi/2, K) - e^{-K\sin\alpha} I(\pi/2 - \alpha, K) \right) \stackrel{!}{=} 1. \tag{4.14}$$

This equation is analysed graphically in figure 4.4. It shows the left side in a set of curves parametrised by K and the claimed unity. The lowest curve is for $K = 0.7420$ and the top curve for $K = 0.7431$. The difference in K from one curve to the next is $\Delta K = 0.001$. One clearly sees that the optimal K varies with the entrance angle α, but the dependence is not very strong. For an entrance angle of 4° the value of K is between 0.7430 and 0.7431 and for an angle of 0.5° the value of K is between 0.7423 and 0.7424. The central K is chosen to be

$$K_0 = 0.7426.$$

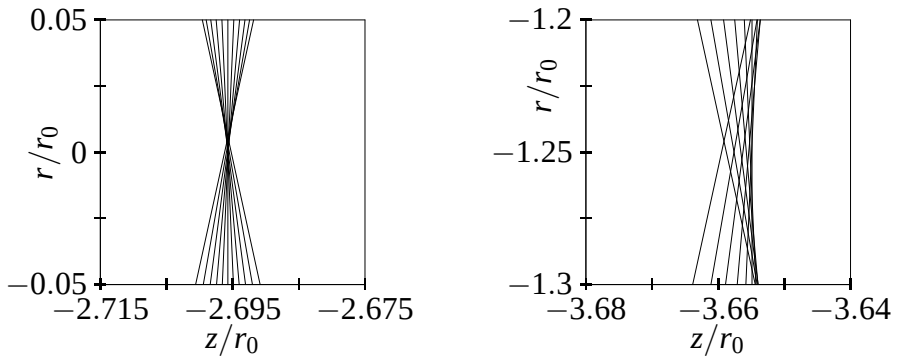

Figure 4.6: A magnification of two parts of figure 4.5 shows the quality of the focus in the z direction. The left picture shows the focus for $K = K_0$ and the right picture the one for $K = 1.2K_0$.

A variation in K of 10^{-3} for an optimal focus up to angles of 5° results in a momentum resolution of the same order, because of their linear correlation. For each K the difference is

$$\Delta\Delta z = r_0 \tan\alpha - \Delta z(\alpha).$$

In order to calculate the position of focal plane a shift of coordinates is performed to have the source of emission at $z = 0$ and $r = 0$. Starting from equation (4.12) the new equation z' is

$$\begin{aligned} z'(\psi) &= z(\psi) - z(\pi/2) - \Delta\Delta z(\psi) \\ z'(\psi) &= z(\psi) - z(\pi/2+\alpha) - r_0 \tan\alpha \end{aligned} \tag{4.15}$$

and plotted in figure 4.5 in the shaded area denoted as *magnet*. On the right side an electron beam hits the radiator target at $r = 0$ and $z = 0$. Then the beam scatters to large angles. Shown are scattering angles from -5° to 5° as straight lines before the magnet. Inside the magnetic field the equations (4.11) and (4.15) define the electrons' orbits. On the left side, outside the magnetic field, the electrons follow straight lines again and are focused for different energies on a nearly linear line.

Figure 4.6 shows the magnification of figure 4.5 in two points. A very high resolution can be obtained for $K = K_0$ compared to the focus for $K = 1.2K_0$. A correct quantification is not yet possible because of the large scattering angles used here, but a qualitative property is that larger angles extend the size of a focus to the high-(low-)K side of the magnet if K is above (below) K_0. As seen before the scattering angles are much below 5° and so the focus quality should be much better. Since this calculation does not concern the fringe fields, both conditions are discussed and evaluated quantitatively in the section 4.3.

For the calculation of the horizontal width of the focal plane, the central orbits are calculated. With $\psi_s = \psi = \pi/2$ the integral in equation (4.12) could be approximated by

$$z = -Kr_0 e^{-K\cos\psi_s} \int_0^{\pi/2} \cos\psi e^{(K\cos\psi)} d\psi = Kr_0 \cdot (e^{aK} + b)$$

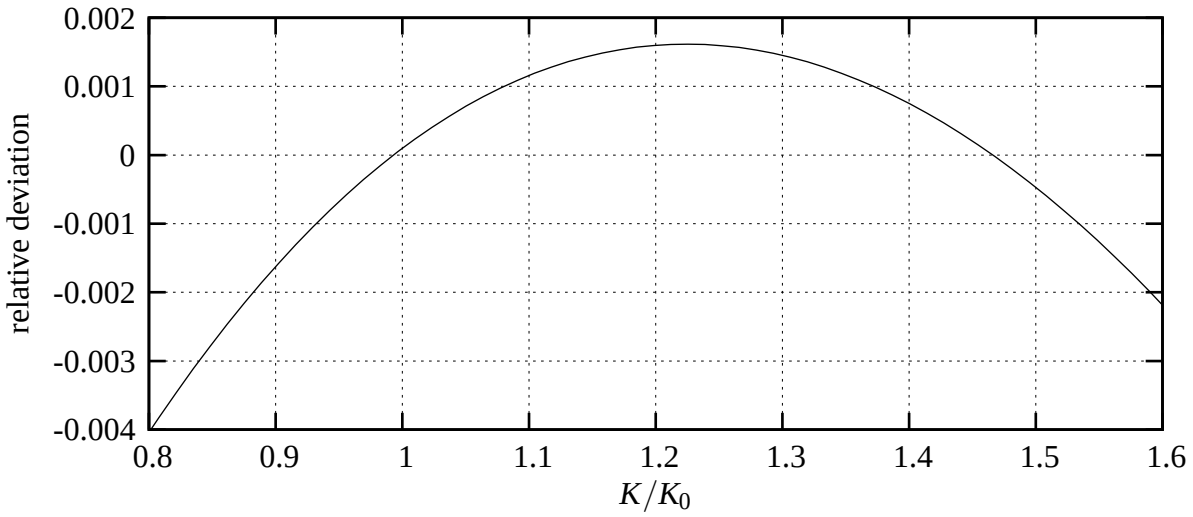

Figure 4.7: The relative deviation of the approximation $(e^{0.691*K} + 0.362)$ to the integral $\int_0^{\pi/2} \cos\psi e^{(K\cos\psi)} d\psi$

with $a = 0.691$ and $b = 0.362$.

The relative deviation, given in figure 4.7, is less than a few tenth of a percent which is sufficient for the determination of the focal plane.

The derivative with respect to K gives an expression for the spatial resolution

$$\frac{dz}{dK} = r_0 \left(e^{aK}(1+aK) + b\right)$$

and with the momentum resolution of $dp/p = dK/K$ it holds that

$$\frac{dz}{r_0} = \left(e^{aK}(1+aK) + b\right) \cdot \frac{dp}{p} K. \tag{4.16}$$

It should be kept in mind that z is the distance to the line of symmetry at $\psi = 0$, so after the coordinate transformation the spatial resolution is twice the amount. This value gives the width for one detector element in the focal plane.

For $dp/p = 10^{-3}$ the left-hand side of equation (4.16) is plotted in figure 4.8. It is remarkable that the spatial width increases with K.

4.2.2 Parameters for the magnetic spectrometer

Since equations (4.11) and (4.15) only depend on r_0 and K the opening angle of the magnet does not effect the resolution or the geometry of the focal plane. To achieve a high resolution and to minimise the detector size the focal plane array will be arranged around $K = K_0$. The scaling factor r_0 is limited by the production costs of the magnet. It should be as large as

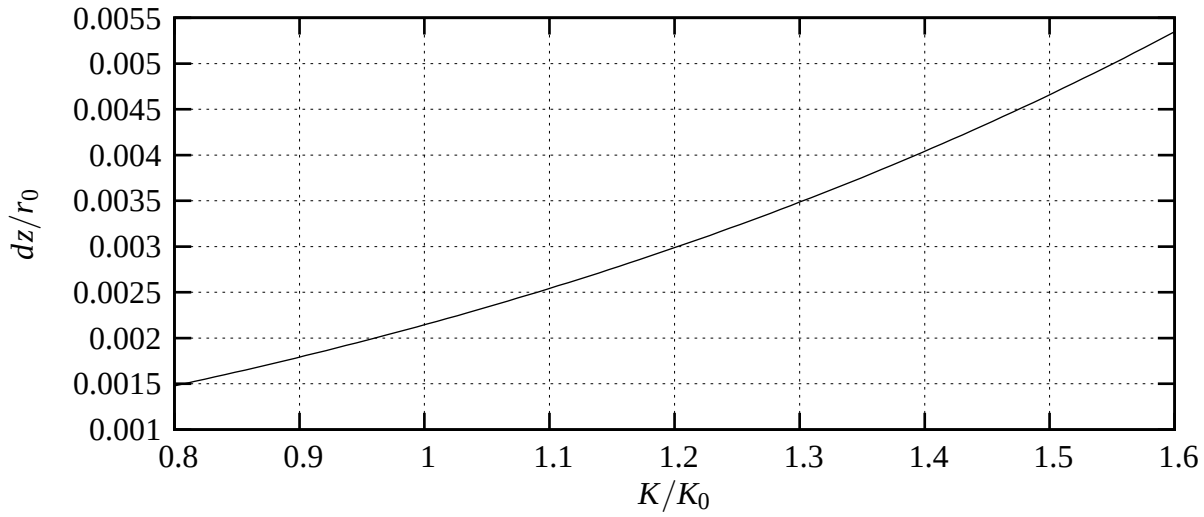

Figure 4.8: The spatial width of scattered electrons with a relative momentum uncertainty of 10^{-3}. The width increases with increasing momentum K.

possible to reach a high spatial resolution with reasonable widths for the detector elements. The negotiation with the manufacturer allowed a maximum value of $r_0 \approx 281.7\,\text{mm}$. The opening angle of the magnet should be as large as possible to provide a large acceptance. But with a larger angle the gap of the magnet gets larger at fixed r_0. So the desired angle is as large as the largest scattering angles of the electrons and photons. The angle then was chosen to be 8°. A larger angle would lead to larger gaps and, due to fringe effects, it would be more expensive to obtain the desired magnetic field.

4.3 Fringe field consideration for real geometry

In the previous sections of this chapter all calculations have been made on the basis that the electrons move abruptly from a field-free region into a region with perfect $1/r$ behaviour. For magnets with air gaps of finite size this discontinuity could not be realized. Calculations and approximations with realistic fringe fields have been undertaken extensively [Cog47, Lil63b, Lil63a, Eng64] before the advent of the first computers that could perform extensive and accurate ray-tracing calculations for charged particles moving in static magnetic fields.

For the motion of particles in the mid-plane, but not in equivalent planes (the median planes) as defined before, the effect of the fringe field could be explained very intuitively. As the particles are already bent in front of the magnet, see figure 4.9, they enter the magnet at another angle and on other position. Both lead to shorter paths inside the magnet and the focal point for $K = K_0$ moves to larger z (smaller distance to the point of emission) and to larger r.

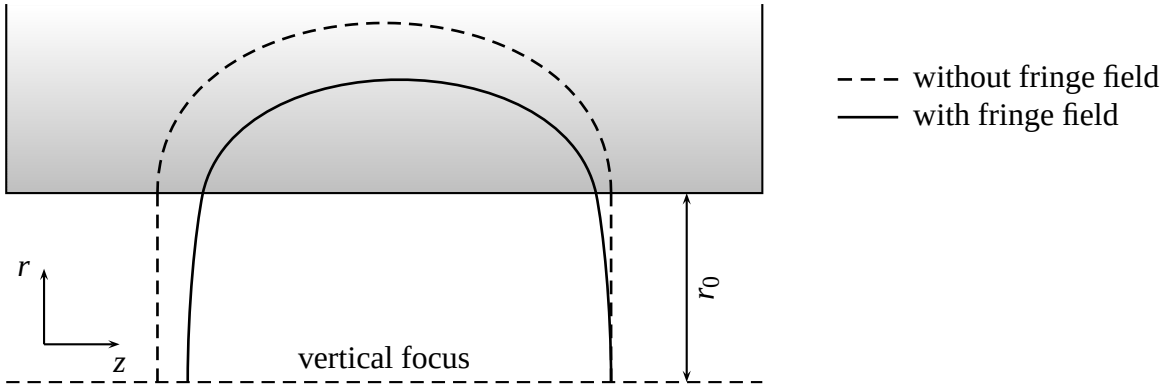

Figure 4.9: Charged particles start from the bottom right side at the line of intersection of the pole faces at the distance r_0 from the magnet. The outer orbit is the calculated path without the fringe field as discussed before. The inner orbit is the path that particles would follow by presence of a fringe field.

As describe by Enge [Eng64] the shape of the fringe field could be described fairly well by

$$h(s) = \frac{1}{1+e^S}$$

with

$$S = c_0 + c_1 s + c_2 s^2 + c_3 s^3$$

and c_1 as the dominating constant. The quantity s is the distance from the pole boundary in units of the gap size. Different values for the constants can be fit depending on the geometry and the position of the coils.

In figure 4.10 the field of a magnet with inclined pole faces with and without fringe fields is shown. Details of the calculation with the commercial software package CST EM Studio™ [EMS04] can be found in the diploma thesis by Jens Hasper [Has05] and in the bachelor thesis by Anna Constantinescu [Con07]. The electrons move a relatively long path in the region of the fringe field compared to the maximum depth, see figure 4.5. Although the focus is moved to a shorter distance from the point of scattering, the focus quality does not suffer. A more severe problem is the fringe field effect of vertically scattered electrons. In the ideal case (without a fringe field) they are scattered to median planes that are equivalent to the mid-plane. Now all the median planes have different field characteristics as shown in figure 4.11.

The perpendicular components of the magnetic field do not differ very much at the rise until 85 % of the maximum. At the peak the strength increases up to 105 % for large angles (4° in figure 4.11) compared to the mid-plane. In this range electrons are bent stronglier with larger scattering angles and the focus smears off to shorter distances. Additionally to a perpendicular field component that does not deflect the particles out of the plane, there is a tangential field component which leads to perpendicular forces. These trajectories could not be described as

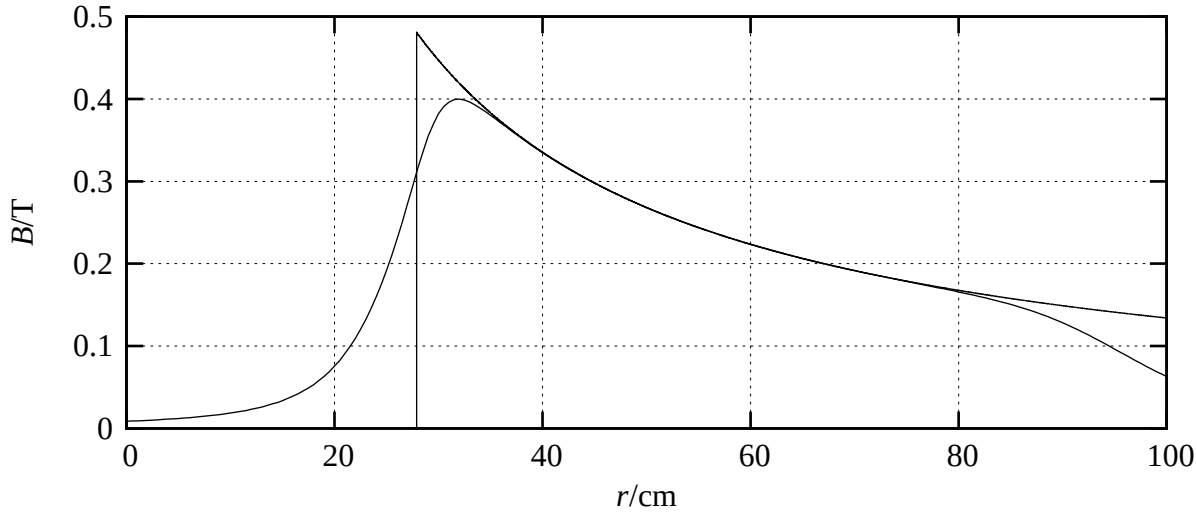

Figure 4.10: The magnetic field of the magnet is shown with and without fringe fields. The sharp cut-off is at the pole boundary at r_0. The fringe field calculation was done with the commercial software package CST EM Studio^{TM} [EMS04] and by the manufacturer with the same results. This was done for the final geometry and maximum magnetic induction. The gap size is 84 mm.

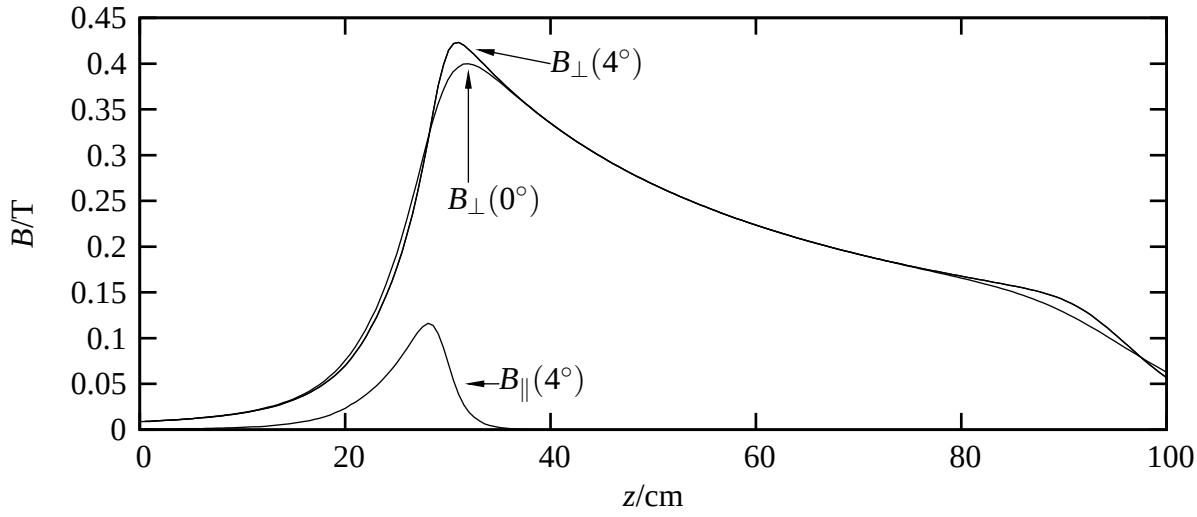

Figure 4.11: The perpendicular ($\perp$) and tangential ($\parallel$) components of the magnetic field in a median plane at 4° compared to the mid-plane (median plane at 0°).

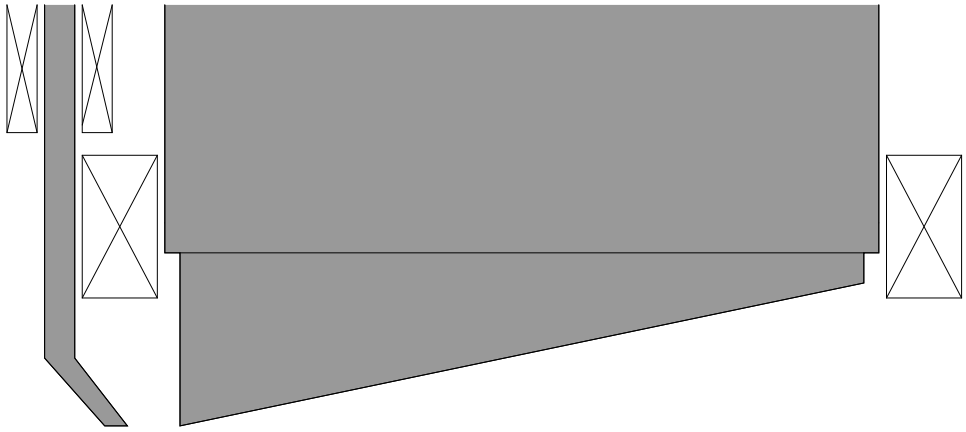

Figure 4.12: The pole face design that was used for the calculation of the magnetic field. The active field clamp is located on the left side and is surrounded by an excitation coil.

those in the mid-plane, because in equations (4.7) to (4.9) the angle ξ_s is not equal to zero. Generally a positive tangential value leads to a force that repulses from a median plane. This force only takes effect if the momentum in the z direction is not zero. So it is important to reduce the entrance angle. A quantitative analysis is done by ray-tracing, described later in this chapter.

4.3.1 Fringe field reduction with active field clamps

To reduce the fringe field and optimise the focus quality, *active field clamps* have been designed that generate a magnetic field in the opposite direction.

Figure 4.12 shows the pole face arrangement with the final position of the active field clamps. The field of the clamps could be controlled independently from the main field.

Figure 4.13 shows the result of a calculation. It is clear that the entrance angle of the incoming beam is reduced by reducing the fringe field, but the difference in the peak has not changed at different median planes.

4.4 Particle tracking

Since the quantitative examination of the characteristics of the focuses of the real magnetic field could not be done analytically, the best and easiest method is *particle ray-tracing*. For the implementation of the ray-tracer some fundamental parts of the Geant4 library have been used. The particle generation and the particle tracking through electromagnetic fields is the basis of the program. A more detailed description of the code can be found in the bachelor thesis of

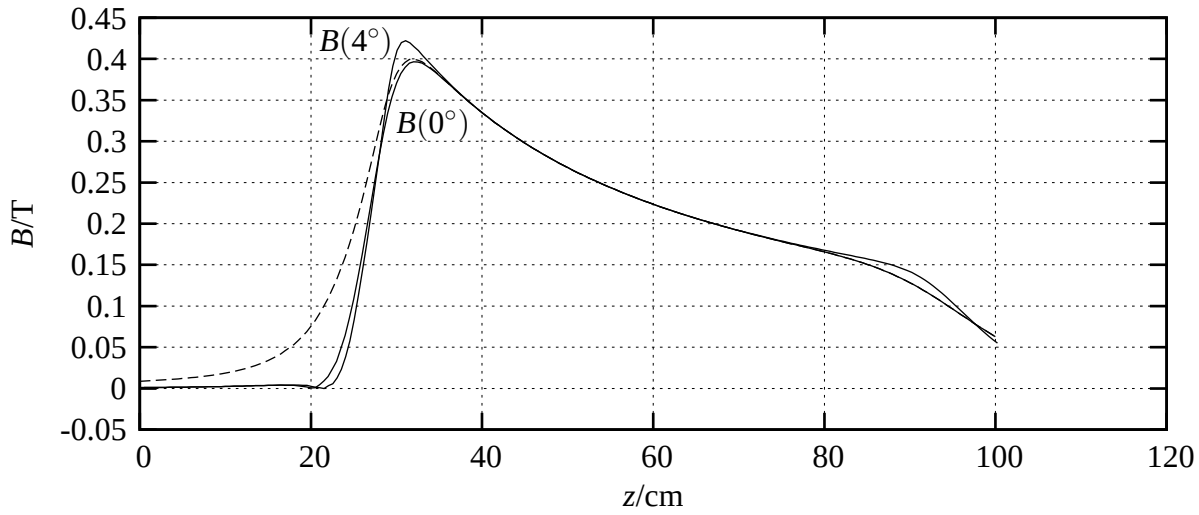

Figure 4.13: The magnetic field with active field clamps is shown for the mid-plane and for a median plane at 4°. The magnetic field without clamps is shown as a dashed line for the mid-plane. The clamps have been optimized to minimize the fringe field. The current ratio of the exciting coils was 160 A/6 A.

Anna Constantinescu [Con07].

A sampled magnetic field of the manufacturer's calculation was used with the final r_0 of 281.7 mm. The table is a three dimensional vector field with 6.875 million coordinates. A trilinear interpolation was used for coordinates between the given points.

For particle generation the position was always kept at a fixed point at the line of intersection of the pole faces. The direction was changed in a way that a realistic angular distribution was obtained, comparable to that of a gold target with a thickness of $0.3\,\%X_0$. Due to symmetry reasons only one half of the magnetic field was used to track one thousand particles.

4.4.1 Focus quality and resolving power

To quantify the resolving power planes of intersection with electron paths have been created, which are perpendicular to the central electron orbits. The electron orbits appear as dots on these planes as shown in figure 4.14. There are planes at different distances (from 40 mm to -5 mm) from the line of intersection of the pole faces, where positive values are measured in the direction to the magnet. The optimal spatial resolution is achieved at 1 mm behind the line of intersection.

The resolution could be quantified by the standard deviation or by a width which contains 90 % of all paths. In the following the 90-% widths were used and all planes of intersection have been searched for the horizontal minimum as shown in figure 4.14.

The spatial resolution and the relative momentum resolution are plotted in figure 4.15. It

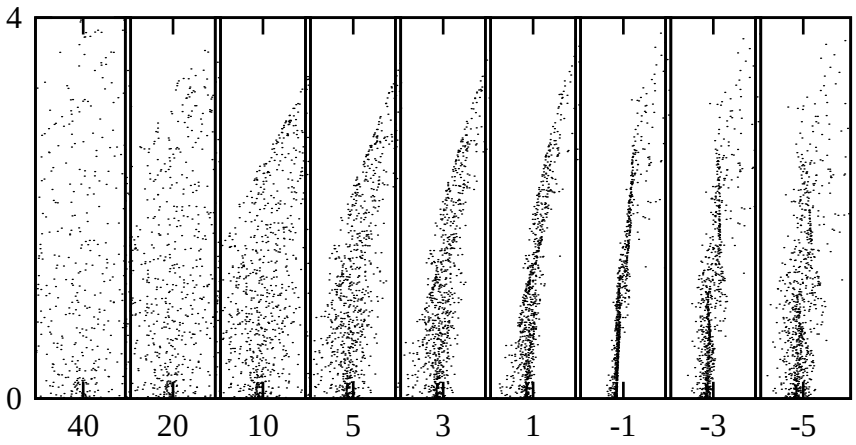

Figure 4.14: The evolution of the electron paths for the momentum K_0 in the vicinity of its focus. Shown are areas of 4 mm height times 1 mm width at different distances from the line of intersection of the pole faces. The focus is at 1 mm behind the line of intersection.

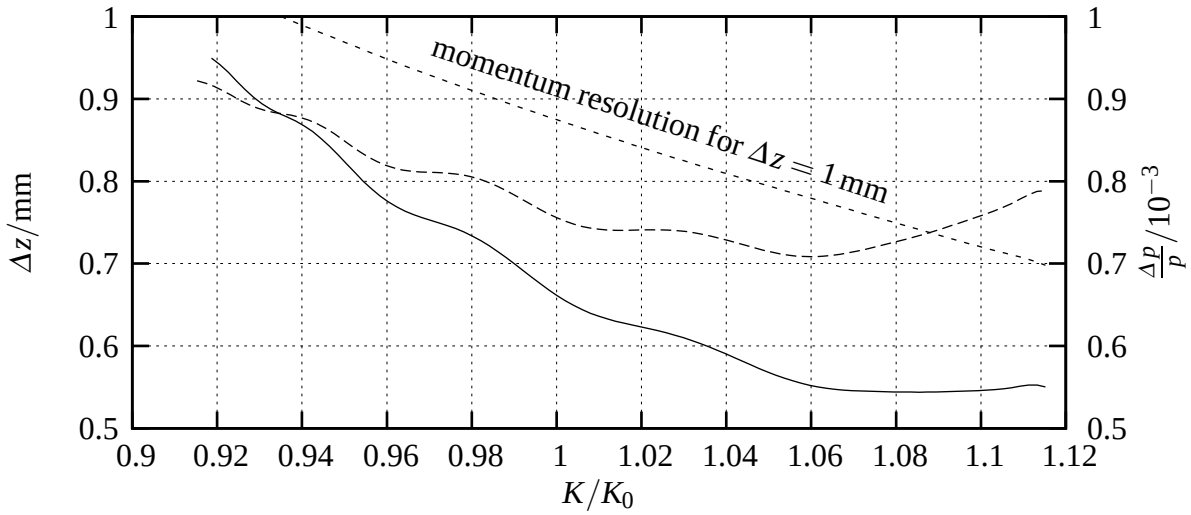

Figure 4.15: The dashed line shows the spatial resolution on the left ordinate for different electron momenta for the magnet with $r_0 = 281.7\,\mathrm{mm}$. The solid line shows the relative momentum resolution in tenths of a percent at the right ordinate. The dotted line shows the momentum resolution limit for a fixed spatial width of $\Delta z = 1\,\mathrm{mm}$.

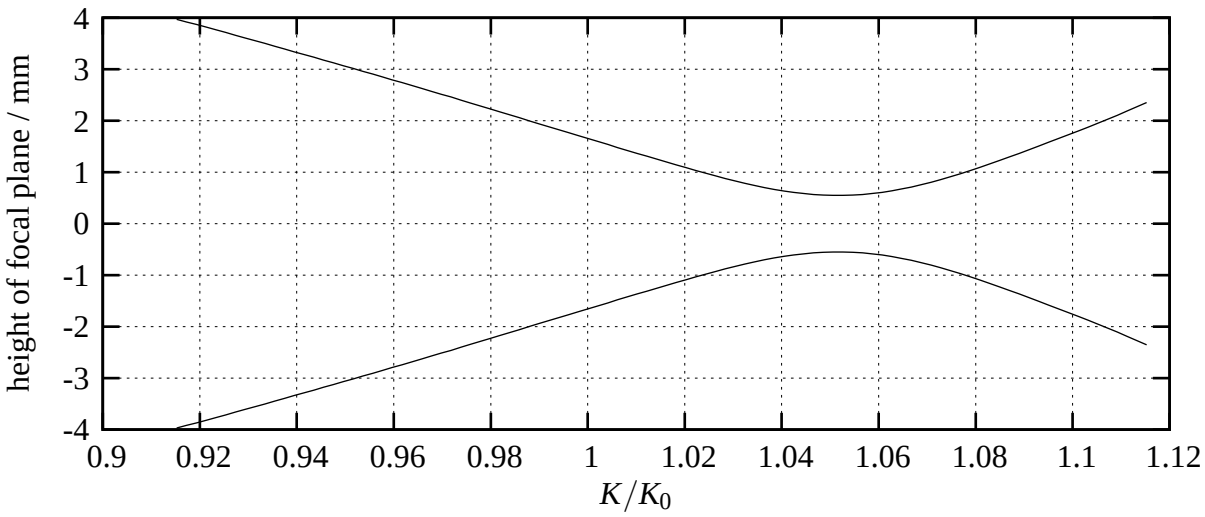

Figure 4.16: The height of the focal plane is plotted. Both curves show the standard deviation from the symmetry plane. The minimum at $K = 1.05 \cdot K_0$ is remarkable.

shows that a realistic angular distribution and the real magnetic field results with a resolution of better than 0.1 % at a spatial width of less than 1 mm. This can be compared with figure 4.8. The momentum K_0 is defined as the momentum where the focus is again in the line of intersection of the pole faces. From the definition of K in equation (4.3) for K_0 holds

$$K_0 = \frac{\gamma_0 m v_0}{B_0 e} = \frac{p_0 c \cdot \mathrm{MeV}}{B_0 e c \cdot \mathrm{MeV}} = \frac{p_0 c \cdot 10^6 \mathrm{Vs}}{B_0 \cdot 3 \cdot 10^8 \mathrm{m\,MeV}} = \frac{p_0 c}{300\,\mathrm{MeV} B(r_0) r_0} \mathrm{Tm}$$

$$K_0 = \frac{p_0 c}{84.64 \cdot B(r_0)} \frac{\mathrm{T}}{\mathrm{MeV}}$$

with $r_0 = 281.7\,\mathrm{mm}$. From figure 4.10 the value for $B(r_0)$ is 478 mT. This strength focuses electrons with a momentum of $p_0 c = 30\,\mathrm{MeV}$ in the line of intersection at $r = 0$. With these parameters

$$K_0 = 0.7412 \pm 0.003$$

which satisfies the no-fringe value of $K_0 \approx 0.7426$, see discussion in the caption of figure 4.4. The uncertainty of almost one half a percent stems from the magnetic field and its interpolation, which are also visible in the wavy shape of the curves in figure 4.15.

The focal height is plotted in figure 4.16. The curves show the standard deviation in the vertical distribution. The total height is always below 10 mm. Remarkable is the minimum at $K = 1.05 \cdot K_0$, since the vertical focus is not at $K = K_0$. This is a fringe field effect of the tangential field component that is strong for large vertical angles, see figure 4.13.

The momentum resolution has been evaluated for scattering energies of 20 MeV. At lower momenta the scattering angles increase (see figure 3.14) and the resolution decreases as seen in figure 4.17. Nevertheless the tagging facility could be used at lower momenta.

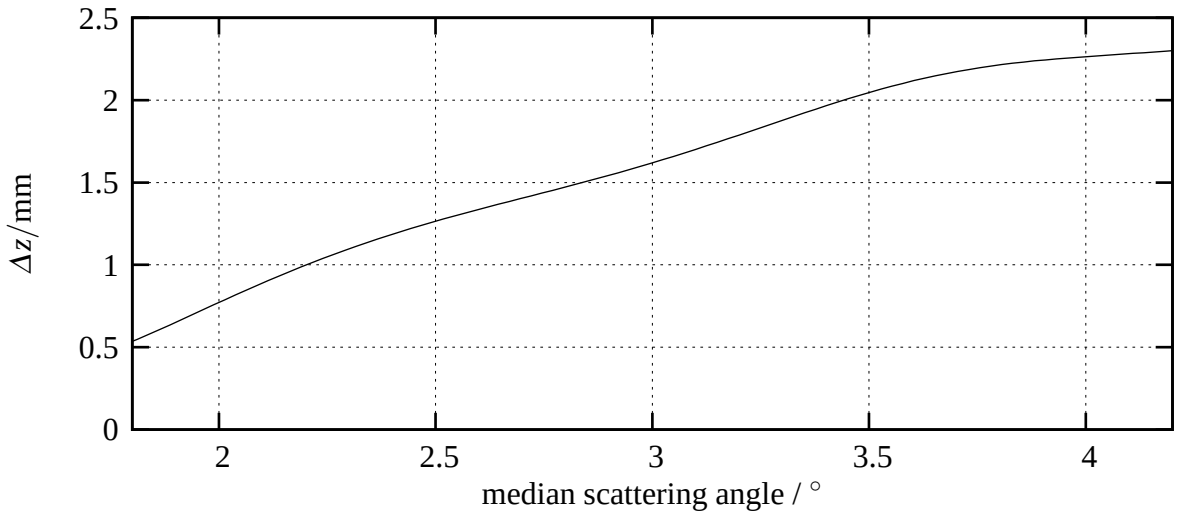

Figure 4.17: The spatial resolution decreases with increasing scattering angle (decreasing momentum) of the scattered electrons. Shown is the focus width for $K = 1.1 \cdot K_0$ as a function of the median angle of the scattered electrons. For the dependence of the angles on the momentum see figure 3.14.

4.4.2 Position of the focal plane

The positions of all minima of the widths of each momentum form the focal plane. The geometry is plotted in figure 4.18. Since the dependence of the z coordinate on the momentum K is quite linear in this range, the corresponding momenta are given in the upper abscissa. The geometry of the magnet limits the z range to -845 mm. The shape of the focal plane is rather linear, so the construction of the focal plane is easy.

The sensitivity of the positioning is plotted for two momenta, $K = 1.0 \cdot K_0$ and $K = 1.1 \cdot K_0$, in figure 4.19. On the left the focus for $K = 1.1 \cdot K_0$ and on the right the focus for $K = 1.0 \cdot K_0$ is shown. Please note the aspect ratio of 40 mm for r to 6 mm for z. It shows that the focal quality does not change much within 10 mm around the focus, so the sensitivity of the positioning of the focal plane is not very high. The asymmetry of the distribution of the electron orbits in the focus is remarkable. The width of the orbits on the left side of the median is much smaller than the width on the right side. This means that there are more electrons that are bent to shorter distances, and this in turn can be ascribed to the larger magnetic field for electrons with large scattering angles, compare to figure 4.13.

4.5 Position of the radiator

The ideal position of the radiator is on the line of intersection of the inclined pole faces of the dipole magnet. In the following the dependence of the focus on this position is studied.

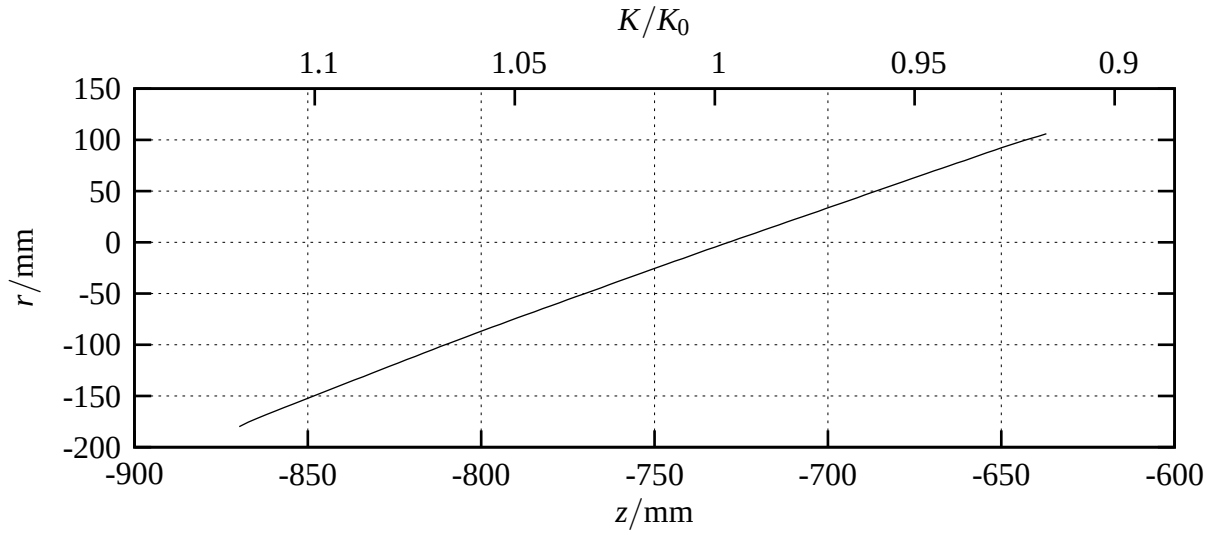

Figure 4.18: The geometry of the focal plane is plotted in coordinates relative to the radiator. At the upper abscissa the according momenta relative to K_0 are given. The dependence between momenta and z coordinate can be linearised quite well in this range.

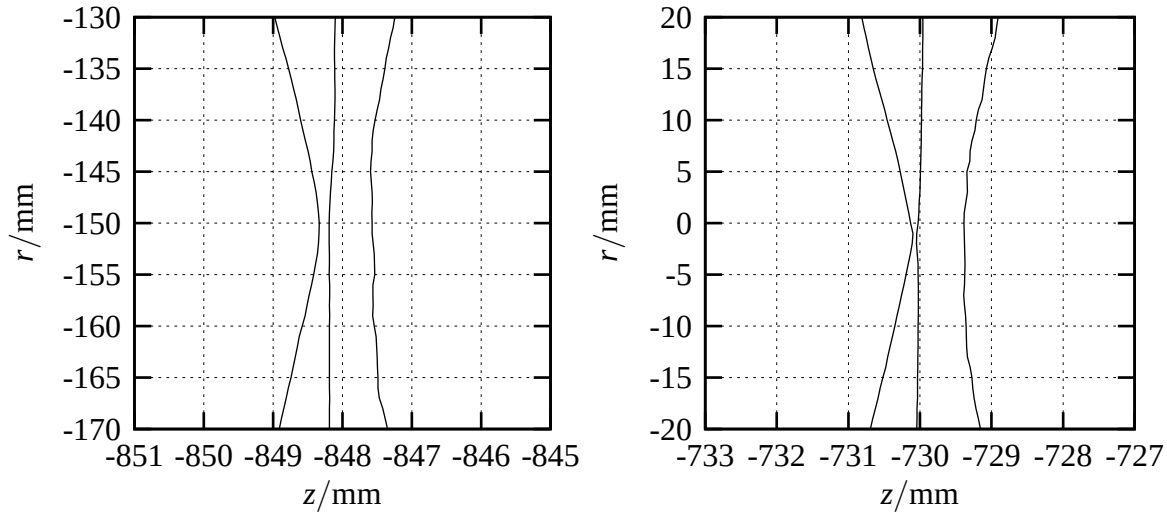

Figure 4.19: The evolution of the electron paths in shown in the vicinity of the focal point. The left plot shows the focus for $K = 1.1 \cdot K_0$ and the right plot the one for $K = 1.0 \cdot K_0$. Note the aspect ratio of 40 mm for r to 6 mm for z. The middle line is the median of the distribution and both outer lines mark the central 90-% region.

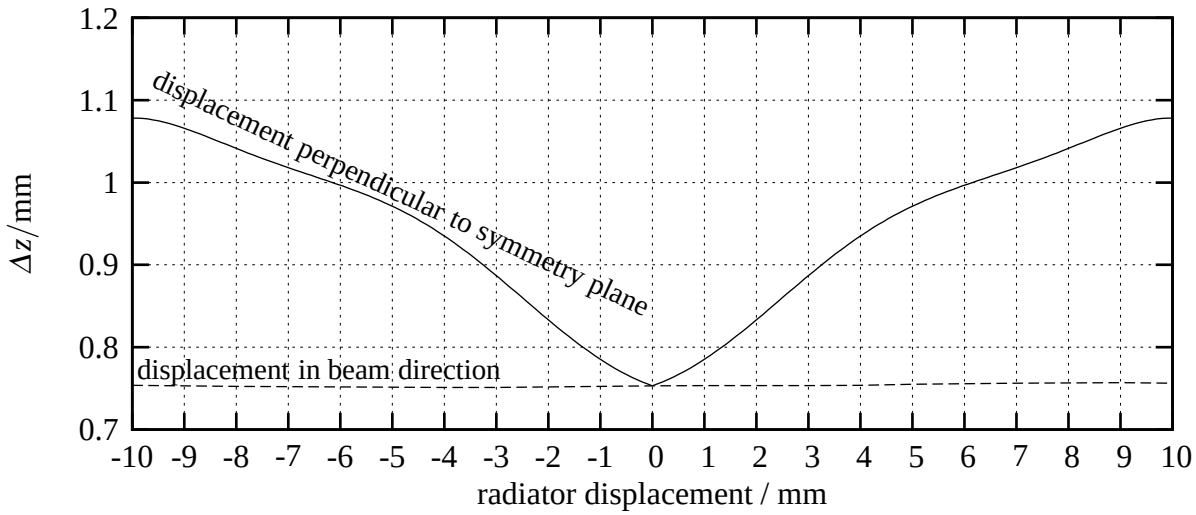

Figure 4.20: The effect of the displacement of the radiator on the focus quality is shown. The ordinate shows the width that contains 90 % of all electron paths in the focus at $K = 1.1K_0$. The dashed line shows the displacement of the radiator in the beam direction and the solid line shows the dependence on the displacement perpendicular to the magnetic symmetry plane.

Figure 4.20 shows the effect of displacing the radiator on the quality. Shown is the 90-% width of the focus at $1.1K_0$. The quality is very insensitive to longitudinal displacement in the beam direction. This behaviour can be deduced from the small scattering angles relative to this direction. In this direction the deviation from the cylindrical symmetry of the magnetic field is not very large and the electron orbits are still near to a median plane orbit. The position of the focal plane is shifted linearly to smaller r. The position in z direction does not change.

An offset perpendicular to the symmetry plane of the magnet has a larger effect on the quality, but it is still good natured. At an offset of five millimetres the focal width remains below one millimetre. The perpendicular offset leads to a large deviation from the cylindrical symmetry, which worsens the focal quality. The position does not move very much. For a radiator offset of 10 mm the focus shifts 0.3 mm to shorter distances (larger z). The shift in r is below the resolution of the simulation (1 mm).

4.6 Position of the beam dump

Most electrons of the incoming beam do not loose much energy in the radiator foil, see figure 3.10. So a beam dump has to be installed for electrons that do not participate in the tagging process. For low photon energies of about 6 MeV to 10 MeV the orbits of electrons not scattered would hit the magnet's yoke. So in the *low-energy mode* the electrons leave the magnet

through a hole in the yoke. In this mode the ratio of the momenta of incoming electrons and scattered electrons has to be kept.

In the *high-energy mode*, the electrons leave the magnet at the open rear side of the magnet. Here a large beam dump can be used to operate more efficiently with a different K_0 and the same incoming beam momentum. The limits for these modes have been scanned by ray-tracing.

The spectrometer should be usable in the horizontal and vertical positions. In the vertical position, the low-energy beam dump should stand on top of the magnet and dump electrons with the lowest possible momentum. This momentum is at $K_{\mathrm{BD}} = 1.38 \cdot K_0$. At lower momenta the beam dump cannot stand stable on top of the magnet (see figure 7.4). The hole in the yoke had to be small to minimise effects on the field shape and therefore the momentum of the incoming beam is fixed to values around the value mentioned above. This means that for a desired photon energy of E_γ the energy difference of incoming electrons and measured electrons is E_γ and the momentum ratio has to be K_i/K_0, which is, at relativistic energies, equal to the energy ratio E_i/E_0 where E_0 is the energy corresponding to K_0 and E_i is the energy of the incoming electron. This system of equations leads to

$$E_i = \frac{K_i/K_0}{K_i/K_0 - 1} E_\gamma.$$

First tests in low-energy mode showed that K_i could be varied by $\pm 5\,\%$ without missing the beam dump. With a linearisation this leads to a variation of the accelerator energy of

$$\frac{\Delta E_i}{E_i} = -\frac{1}{K_i/K_0 - 1} \cdot \frac{\Delta K_i}{K} \approx 13\,\%.$$

In high-energy mode the electrons must not hit the yoke, so there is a minimum K_i for the momentum of the incoming electron. From ray-tracing, this minimum is at $K_{\mathrm{min}} = 1.7 \cdot K_0$.

5 Focal-plane detector array

This chapter deals with the geometry and the position of the focal plane in consideration of the focus quality and the resulting energy resolution of the tagged photon beam. Later on different detection methods will be discussed and the functional principle of the chosen organic scintillators explained.

5.1 The geometry of the focal plane

The electrons, degraded by the radiator and focused by the magnet, have to be detected in the focal plane. All electrons in the relevant energy region leave the magnet nearly anti-parallel to the incoming beam, see figure 4.19. This defines the orientation of the detectors to be perpendicular to the magnet. The shape of the focal plane is given in figure 4.18 and it is nearly a straight line. The usable range is from $K = 0.915K_0$ at $P(z,r) = P(-637\,\mathrm{mm}, 106\,\mathrm{mm})$ to $K = 1.095K_0$ at $P(z,r) = P(-844\,\mathrm{mm}, -146\,\mathrm{mm})$ which is limited by the available space inside the vacuum chamber. The origin of the coordinates is at the radiator position. This space has been maximised for the magnet's geometry with the active field clamps. At $K_0 \mathrel{\hat{=}} 20\,\mathrm{MeV/c}$ the detectable momentum range is $3.6\,\mathrm{MeV/c}$ at a length of $\Delta z = 207\,\mathrm{mm}$ and depth of $\Delta r = 252\,\mathrm{mm}$. See table B.1 for the exact geometry.

The width of one focal-plane detector should be on the order of the spatial resolving power of the magnet, in order to not decrease the possible resolution. In this case the ideal width is $0.7\,\mathrm{mm}$ with a resulting momentum resolution of $0.06\,\%$ at $K = K_0$ and $0.05\,\%$ at $K = 1.1K_0$. Although the momentum resolution increases with higher K the upper limit is given by the height of the magnet, since the interesting value is not the relative momentum resolution, but the absolute momentum resolution. For the determination of the energy of the photons the energy of the degraded electrons is a subtrahend, see equation (2.1), and this in turn leads to lower energy resolution for the produced photons.

The resulting energy resolution for the photons is plotted in figure 5.1 for different ratios of incoming electron momentum to degraded momentum. The resolution is evaluated in the relativistic limit, where $E_e = cp_e$, by neglecting the rest mass of the electrons. The given momentum ratios are those of the different energy modes, see section 4.6. The resolution has a minimum that moves to larger values of K/K_0 on the focal plane with increasing K_i/K_0, namely the momentum ratio of incoming electron beam energy and scattered electron energy. For the low-energy mode ($K_i/K_0 = 1.38$) the uncertainty of the photon energy does not exceed a value

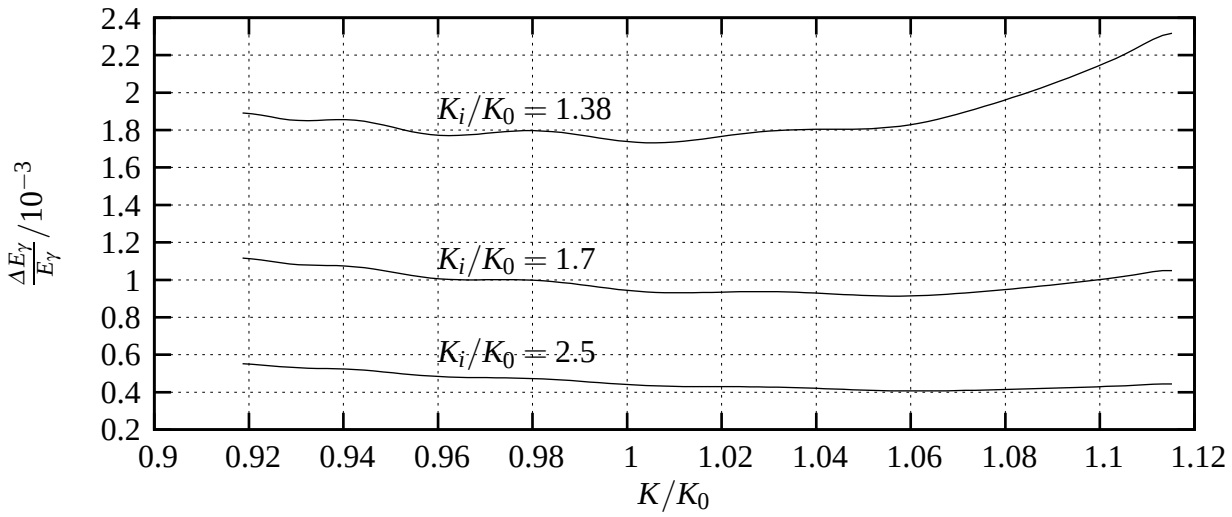

Figure 5.1: The relative energy resolution of the produced photons for three different ratios of incoming electron momentum to degraded electron momentum. The upper curve shows the shape for the low-energy mode (see section 4.6), the middle curve is for the lower limit in high-energy mode. The minimum in uncertainty moves to larger momenta for larger momenta of the incoming electrons.

of 0.24 % across the focal plane, but increases quickly beyond $1.1K_0$.

5.2 The focal-plane detectors

Most widely used detectors for electron detection at high spatial resolution are plastic scintillators, multi-wire chambers, silicon detectors and maybe in the future diamond detectors. Plastic scintillators generate optical photons by charged particles that ionise the material. For electrons at 20 MeV the typical yields are two thousand photons per millimetre path in the material. The light has to be transported with optical fibres to a photomultiplier tube. With typical collection efficiencies, transportation efficiencies and quantum efficiencies about ten photons are expected to produce a signal. The low overall yield requires a high accuracy in the construction and assembling of the detection system. Typical time resolution is about a few nanoseconds without dead time and the signal width is about 20 ns. An important advantage is the ease of fabrication into desired shapes at very low costs. In addition, special fibres with quadratic cross sections and an edge length of 1 mm are available [Yao06].

In gas filled wire chambers a particles produces electron-ion pairs along its path. In the presence of electric and magnetic fields, the ionisation electron drifts to a collecting anode wire where it is then accelerated by a strong electric field so that secondary ionisation occurs and an avalanche follows. With a quenching gas the avalanche region could be kept localised and a

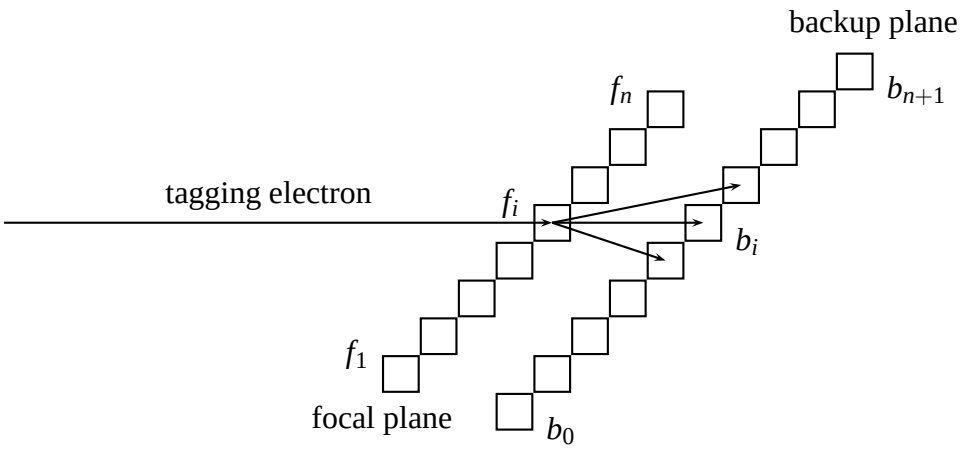

Figure 5.2: The tagging electron hits from the left of the focal plane and scatters to one of three detector elements in the backup plane. A tagging event is only generated in a produced backup event with a focal plane event.

spatial resolution of about a few hundreds of micrometres at a wire spacing of 1 mm is possible. The drift time is in the range of 50 ns/mm to 100 ns/mm, which defines the dead time of the detector. The time resolution is in the order of a few nanoseconds. Because of the large dead time, the rate is limited to a few 10^4 per second per wire [Yao06].

Silicon detectors are $p-n$ junction diodes that are operated in reverse bias to form a depleted region of mobile charge. This region is sensitive to ionising particles which produce electron-hole pairs that could be measured. The strip width can be below one hundred micrometres, but the time resolution is around 25 ns with a very large dead time, which disqualifies it for the use in the tagging facility [Yao06].

Polycrystalline diamond detectors, which are used in the same way as silicon detectors, offer a very good time resolution of better than a hundred picoseconds at a maximum rate on the order of 10^8 per second [Ber06]. These detectors rely critically on low-noise electronics to allow a very low detection threshold. Unfortunately, it is not yet a standard application to separate a single-electron event from noise at a high confidence level.

We have chosen scintillating fibres with photomultiplier tubes as detector elements in the focal plane, because of easy handling, high rates, high time resolution and moderate costs. The detector elements are quite cheap and can be tooled and handled by students. The expensive components are the photomultiplier tubes, but they do not need to be adapted for different experiments.

For different experimental demands the detectors can be arranged in different ways. The normal arrangement is to have all detectors side by side in the focal plane to cover a broad energy range. The trigger is generated from the experiment and in this case the energy information of the focal plane is used. Because of the small time window random coincidences are

very unlikely, see section 2.1. If absolute background should be reduced, for example if the absolute photon flux should be controlled with the focal plane or the focal plane should generate the trigger, a backup plane can be placed behind the focal-plane detectors, see figure 5.2.

A tagging electron hits the i^{th} detector element F_i in the focal plane. The electron interacts with atoms in the scintillating fibre and leaves within a small angle. At the distance where the backup plane is located it is presumable that one of three detector elements of the backup plane (b_{i-1}, b_i, b_{i+1}) get hit by the electron within 100 ps. A tagging event (t_i) is only generated if at least one of those three backup elements report a hit.

$$t_i = f_i \wedge (b_{i-1} \vee b_i \vee b_{i+1})$$

This tagging logic array (TLA) is based on a simple PLA. The TLA is not finished yet and only needed if background has to be reduced.

5.2.1 Performance

There are three issues that have to be addressed in the realisation of the detector system. The detector elements have to be small to provide a high spatial resolution, but the photomultiplier tubes are much larger, so they could not be connected directly to the scintillating fibres. The fibres have a short radiation length for the scintillating photons ($X_0 \approx 42$ cm) and cannot be made very long to guide the light to the photomultiplier tube. Besides that, a long scintillator would cause some bothersome side effects. A fibre-optic light guide must be used to guide the light from the scintillators to the tubes. This in turn causes a loss of typically 50 % of the photons at the additional coupling of the fibres. For easier handling the photomultiplier tubes form the vacuum closure at the detector chamber, that can be replaced by a blind flange. A sketch is shown in figure 5.3.

The performance of the detector system is limited by the photomultiplier tubes and by the succeeding discriminators. A vital requirement to the photomultiplier tubes is the gain. Since only about ten photons are expected from an electron hit in the scintillator the amplification has to be large and have low noise to distinguish a hit from other single-photon events. Noise is produced by thermionic emission and field emission of electrons at the cathode and the dynodes. This noise appears as a so-called dark current.

The width of an amplified signal at the anode is about 15 ns at a maximum voltage of 80 mV. At a count rate of 10^6 /s the fraction of hits that occur within this width is about 1.5 %, see equation (2.4). These hits produce a pile-up and they cannot be distinguished by the succeeding discriminator.

The constant fraction discriminators are embedded in the housing of the photomultipliers which support the same differential signal standard (LVDS) as the data acquisition. The processing time of the discriminators should be short, so that a count rate of 10^6 /s is possible without considerable dead time. The tests showed that all requirements are fulfilled.

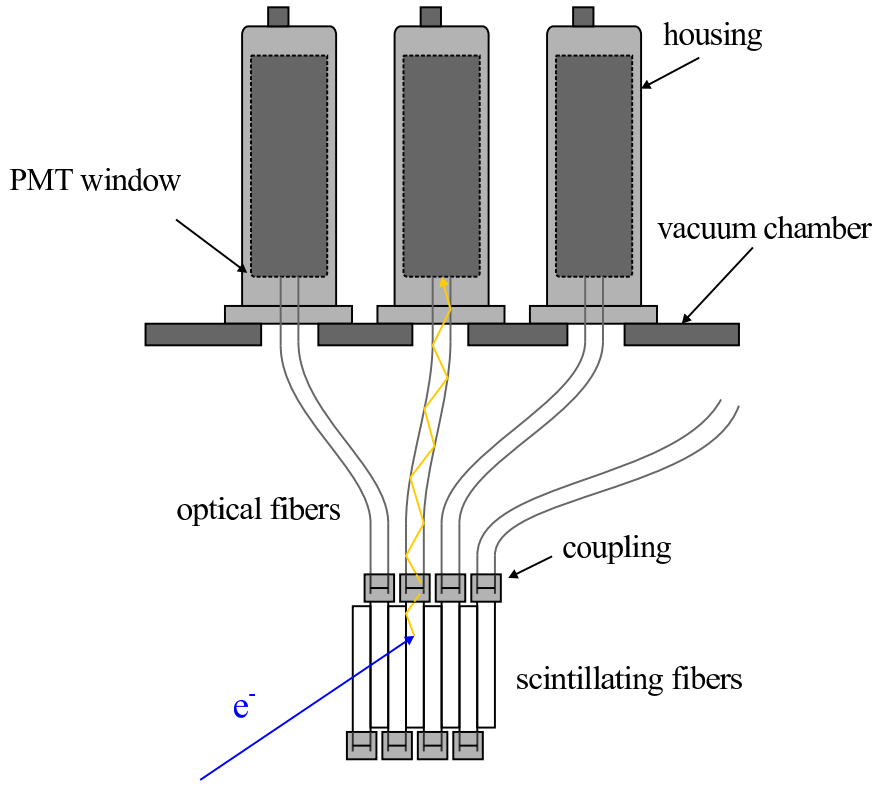

Figure 5.3: Sketch of the arrangement of the scintillating fibres with light guides and photomultiplier tubes. The sensitive fibres are coupled with optical glue to the optical fibres that guide the scintillation photons to the photomultiplier tubes. The light guides are not connected with optical grease or similar to the tubes because is does not increase the transmission probability, actually there is a small gap of $1-2\,\mathrm{mm}$ to the tubes. Although photons leave the fibre at large angles up to 35° all photons hit the large photocathode. The picture is taken from the diploma thesis of Jens Hasper [Has05].

Details on the focal planes detectors with simulations, tests and measurements, and the slow control can be found in the diploma theses of Janis Endres [End07] and Michael Elvers [Elv07].

6 Data acquisition

The most crucial part of the tagging system is the data acquisition system. Especially for coincidence experiments with slow reaction products additional effort is necessary to combine a high rate of tagging electrons of about 100 MHz in total with possibly long ejectile detection times of up to a few microseconds. The average electron count per ejectile detection is a few hundred, and it is possible that fast particles produced later are detected before particles produced earlier.

Experiments with tagged photons and only fast reactions products can be performed with standard electronics, since the time difference of an electron hit and the detection of the reaction product only fluctuates within a few nanoseconds and can be regarded as nearly constant.

6.1 Time characteristics of the different experiments

To assign the slow and rare reaction products to the prompt and frequent electrons the time structure of the events is plotted schematically in figure 6.1. The points show all tagging electron hits, the *hit history*, in the focal plane within 500 ns with their energy on the left ordinate and their time stamp with respect to the detection time of the reaction product on the abscissa. The right ordinate shows the resulting energy of the tagged photons. Here an incoming beam energy of 30 MeV is assumed. The recorded time is the time when the photo-reaction at the target was initiated. Most reactions took place in a time span that is an order of magnitudes shorter than the time resolution of the detectors and can be disregarded, so this time is the point when the reaction product has left the target. Minimally the separation energy has to be exceeded by the photons to produce particles from the target. Additional energy is converted into kinetic energy of the reaction products. The amount of kinetic energy depends on the excitation energy of the compound nucleus, which leads to a correlation between the time-of-flight of the detected ejectile and the energy of the tagged photon. This time-energy correlation is plotted in figure 6.1 as a solid line with respect to the particle's separation energy plotted as a dashed line. The zero point in time is the detection time of the particle. It is clear that high photon energies produce particles with high kinetic energies and short times-of-flight, which is at the right hand side of the picture, and photon energies close above the threshold produce slow particles with long times-of-flight. This in turn means that only those electrons accompany the detected particle where the time-of-flight information matches the photon energy. This is the case for only one electron in the plot. Due to the finite time and energy resolution an unambiguous assign-

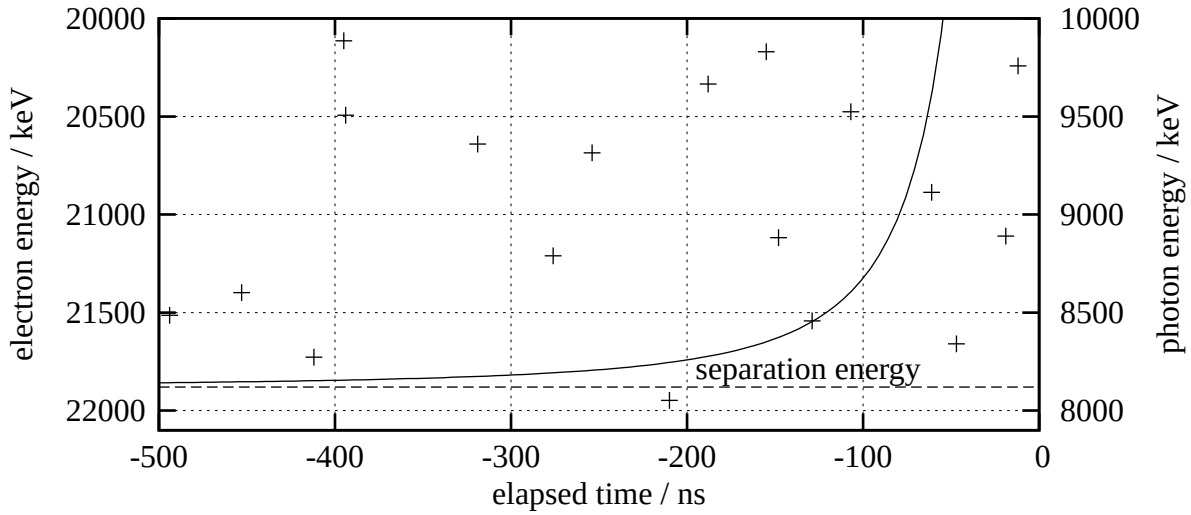

Figure 6.1: The detection times of tagging electrons for slow reaction products are plotted schematically. The left ordinate shows the electron energy in the focal plane of the spectrometer and the right ordinate the corresponding photon energy for an initial electron energy of 30 MeV.
With the elapsed time on the abscissa the points form the history of electron hits in the focal plane with their detection times and their energy. The detection time is given with respect to the detection time of the reaction product. The dashed line indicates a typical separation energy (right ordinate) for the reaction product in the target.
The solid line shows the photon energy as a function of time of flight of the reaction product. The strict relationship between photon energy and time of flight separates good events from background events.
Here the time-of-flight condition matches exactly one electron hit. Other hits are regarded as background and can be eliminated with high confidence or will be assigned to later detected reaction products.
In this picture the distance from target to product detector is 1 m and the product was assumed to be a neutron. The error bars are covered completely by the size of the points.

ment is not always possible. This background cannot be eliminated, but it is rather improbable as discussed in section 2.2.2.

A target may remain in different excited states. Then the time-of-flight is not relative to the separation energy but rather to the energy of the excited state. Those particles travel a longer time to the detector and have to be assigned to electrons with lower energy. Without other detectors it is not possible to distinguish between different excited states. The additional use of other detectors would extremely reduce the maximum tagging rate and is out of the question. The remaining option is to dump the complete history on every trigger from a particle detector. This history contains the complete information on the electron hits, the energy and the time, which span the phase space of this system. The area that is covered by one point is given by a time resolution of about 5 nanoseconds and by an energy resolution of about 20 keV, which corresponds to one detector element and therefore forms a fixed lattice on the energy axis. At a rate of 10^6 per second per detector the chance of two events within twice the time resolution is 1 % and almost all hits can be separated. The average distance is one microsecond. Generally at high tagging efficiencies for one trigger event one point in the full phase space is a tagging electron that is located on a time-of-flight line. Other points are spread over the whole phase space equally in time and exponentially in energy. At low background most electron hits are gathered around the lines of time-of-flight for the different excitation energies. For known separation and excitation energies the decision for which electron hit belongs to the trigger is easy, but has to be done off-line. The next chapter deals with raw spectra where these energies are not known.

6.1.1 Background estimation in raw spectra

The energy range of the full phase space of the photons is limited by the separation energy of the particle at the lower end because no triggers are generated below this limit, and by the energy of the incoming beam at the upper end. The time scale is limited by the time-of-flight of a particle with maximum kinetic energy at the lower end. Generally this is a few nanoseconds and could be approximated as zero. The upper limit is infinite.

The width of one detector element corresponds to an relative energy width of about 10^{-3} of the energy scale. Assuming a constant particle production yield from particle separation to maximum energy, the probability that a trigger corresponds to one hit in the history of this detector element is 10^{-3}. So at a time resolution of 5 ns and a rate of 10^6 /s per detector element the peak-to-background ratio is $1/5$, compare to section 2.2.2. Then, the signal-to-noise ratio would be 10^{-3}, which is about two or three orders of magnitude smaller than the measured one. Higher peak-to-background ratios are available on lower hit rates or better time resolution. A higher spatial resolution does not reduce the ratio. The ratio is also reduced by a factor that is the number of levels which are excited.

This estimate shows that it is possible to examine unknown states in nuclei as long as the level spacing is high enough.

6.2 The CATCH TDC

For the data acquisition a versatile module for buffering the hit history is needed. A brilliant device for this purpose is the CATCH TDC.

The CATCH TDC has been developed at the University of Freiburg for the COMPASS experiment at CERN [Abb07]. The TDC has a hit buffer, where 8 hits could be stored per channel within a maximum time span of eight microseconds. The best time resolution is about 120 picoseconds. Without a trigger the TDC stores every event in a so-called ring buffer. On a trigger event, the information in the ring buffer is converted to a *NEPTUN event structure* or root data structure and written to a file. Details, exact wiring schemes with all electronics, software and electronic development and all tests can be found in the diploma thesis of Michael Elvers [Elv07].

7 New beam line at the S-DALINAC

The S-DALINAC has some beam extractions from the main beam line in the experimental hall. The tagging facility was built at E5, which is the first external experimental place behind the accelerator, see figure 2.3. Here the beam is dispersion-free in the transverse direction which allows one to develop an optimised dispersion-matching mode in the future. The relative energy definition was only a few 10^{-3}, and with additional slits at locations with high transversal dispersion it could be reduced to 10^{-3} [Win93], which is still insufficient. Besides the energy definition the spatial width and the position of the beam spot on the radiator target is vital. It affects the momentum resolution of the magnet directly. Since the spectrometer is movable special attention is needed for the control of the position.

7.1 Requirements and limitations of the accelerator

The most important requirements for the beam are the components of the beam vector at the position of the radiator target. The beam vector is a six dimensional vector in a phase space that describes all beam parameters at a point in the beam line. The components are the position of an electron relative to the ideal orbit in the beam line in the horizontal, vertical and longitudinal directions and the relative momentum deviations in all directions. The momentum deviations in the transversal direction and the divergences describe the angle of the electron.

7.1.1 Emittance of electron beam

The electrons in a bunch have different vectors in this phase space. Under the terms of Gaussian distributed positions and momenta of each electron the ensemble forms a hyper-ellipsoid at each position in the beam line in the phase space. This ellipsoid can be described by a 6×6 matrix, the beam matrix. Since only conservative forces act on the electrons after acceleration, its volume does not change throughout the beam line and the determinant of the matrix is a good quantity to specify the beam quality. The square root of this is the *emittance*. Each spatial coordinate of the matrix is independent of all others. In the two-dimensional projection to one spatial sub phase space, the conservation of volume means that at the expense of large divergences the distribution of transversal positions could be kept small. Details can be found in the diploma thesis of Steffen Döbert [Döb95].

At the beginning of the dispersion-free part of the beam line after the accelerator the

transversal width of the beam spot is about 3 mm at an angle of 1.3 mrad [Par05]. As seen in the last chapters the width must be below 1 mm to not reduce the resolution of the tagging facility. Since the magnetic spectrometer has an acceptance that is more than one order of magnitude larger than the divergence of the beam an increase does not cause trouble.

7.1.2 Energy definition and stability

The energy definition and stability can be ascribed to two parameters. The first parameter is the longitudinal position distribution in a bunch during acceleration, the initial bunch length. The acceleration is done by standing waves in the radio-frequency cavities and the bunch distance is exactly the wavelength of 100 mm. At maximum elongation, the centre of a bunch is at the anti-node, where the electric field intensity has a maximum. Electrons at other positions are accelerated less and so there are slightly different energies in a bunch. After acceleration the half-length of a bunch is about 0.6 mm [Loo95] which results in a minor acceleration of $2 \cdot 10^{-7}$. This is far below the needed relative resolution of about a few 10^{-4}.

The main errors derive from instabilities in the radio-frequency control units of the accelerator. There could be long-term shifts because of, for example, temperature fluctuations, fatigue of material or other external influences with time constants of more than a second. The short-term fluctuations can arise from other electromagnetic fields which induce a disturbance or by the radio-frequency control process itself [Pla04].

Electrons with different momenta take different orbits through the beam line and therefore have different transit times. This results in a longitudinal dispersion which can be measured by phase shifts between two radio-frequency cavity resonators. The electron beam excites transversal magnetic modes in these cylindrical cavities. To increase the long-term energy stability, one rf monitor is located directly behind the accelerator and the other before the tagging facility [Par05, Ara05, Döb99]. The minimum phase shift that is detectable with standard electronics is 0.3°. To maximise the energy resolution the longitudinal dispersion has to be maximized without an enlargement of the transversal beam size. The main beam line was extended by two quadrupole magnets [Par05] and a longitudinal dispersion of 12 mm/% could be reached. The relative energy resolution at the detection threshold for the phase shift is about $7 \cdot 10^{-5}$. The measured phase shift will be used to adjust the accelerator cavities. This method allows an energy stability on a time scale of a few hundred milliseconds. The installation and tests are already in progress and will be finished during 2008.

With the redesign and extension of the main beam line the transversal beam size has been further decreased and much less background is produced in the walls of the beam pipes by outer electrons. This is a great benefit for the tagging facility.

7.2 New beam line

The extraction E5 has been used so far only for experiments with untagged photons. The conversion of electrons to photons took place a few meters behind the main beam line. Now tagged photons should be produced in the tagging facility far away from the main beam line and the vacuum system has to be extended to the tagging facility. The volume of the magnetic spectrometer is connected to beam vacuum, so additional pumps with very high flow rate had to be installed. The leakage rate is dominated by the vacuum chamber with the 128 photomultiplier housings and is about $10^{-3}\,\mathrm{mbar}\cdot\mathrm{l/s}$ [End07]. To obtain a maximum pressure of $10^{-6}\,\mathrm{mbar}$, which is sufficient at the end of the beam line, the flow rate of the pump has to be about $10^{3}\,\mathrm{l/s}$. So a cryogenic pump was installed at the scattering chamber, where the radiator foil is located.

7.2.1 Additional quadrupole magnets and beam control on the target

To focus the electrons with small widths on the radiator foil quadrupole magnets can be used. At least two magnets are needed because if a quadrupole magnet focuses in one direction angles in the perpendicular direction are enlarged. By combining two quadrupole magnets it is possible to get a focusing doublet for both directions. The distance of the last quadrupole triplet in the main beam line to the radiator foil is about 15 m. This distance is too long to focus the beam spot because to obtain large angles the beam width at the position of the triplet has to be very large, larger than the diameter of the beam pipes, so additional quadrupole magnets have to be installed near the radiator. With a doublet at a distance of about 2.5 m from the foil a beam width of better than 0.4 mm is possible. Details can be found in the diploma thesis of Stefan Paret [Par05]. The beam angles are still one order of magnitude smaller than the acceptance of the spectrometer, therefore this is negligible. The position is insensitive to small energy fluctuations because there is no transverse dispersion. Larger energy fluctuations influence the energy definition directly.

To control the beam position on the radiator foil a combination of two dipole magnets is installed behind the quadrupole doublet. These *steerer magnets* are aligned so that their magnetic fields are perpendicular and can be excited bipolarly. This allows one to control the position on the target in a range of a few centimetres. The needed range is only a few millimetres.

7.3 Beam dump

The total yield of the photon production is only a few percent, see figure 3.5, so almost all electrons do not loose much energy. In the high-energy mode the electrons can leave the magnet at any point of the open rear side of the magnet. In the low-energy mode the electrons of the

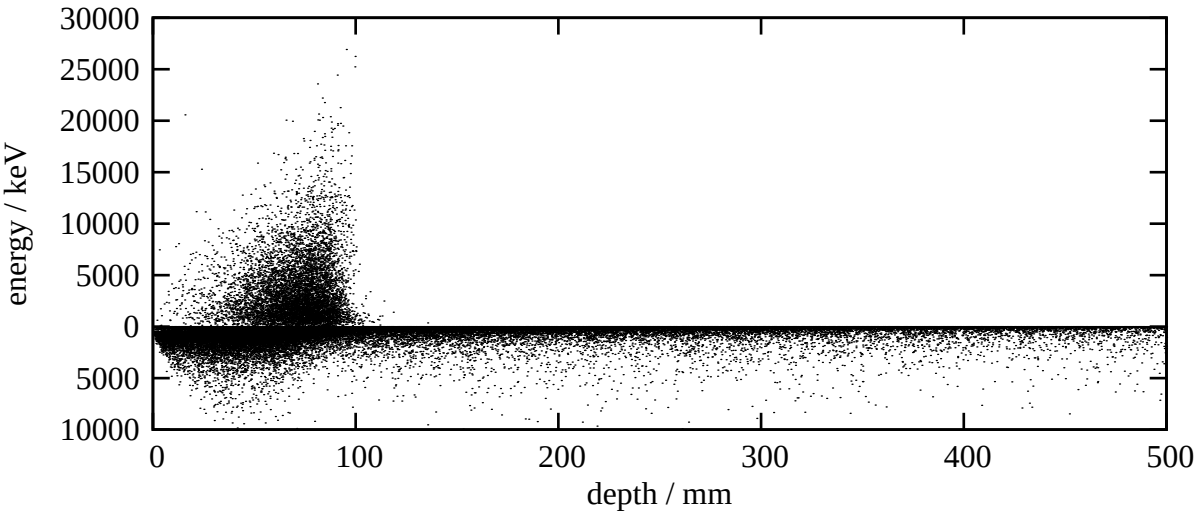

Figure 7.1: Stopped electrons in a block of graphite. The initial energy was 30 MeV. Each point stands for one stopped electron with the depth on the abscissa and the deposited energy on the ordinate. Points above the zero line are primary electrons and points below the zero line are secondary electrons.

main beam leave the magnet at 114° through the yoke of the magnet. Since the magnet is installed vertically the beam dump has to be installed on top of the magnet. Here the beam dump is near the focal-plane detectors and the photomultiplier tubes where background is very annoying. Its size should be very small to allow easy handling with the crane. A simplification is possible if no absolute currents are needed. Then the electron beam does not need to be kept in vacuum and there does not need to be a tight connection of the beam dump to the vacuum chamber.

7.3.1 Simulations

As discussed in chapter 3, low-Z material produces less bremsstrahlung than heavy material. The primary electron beam should be stopped completely in a core of carbon, namely graphite with a density of about $2.0\,\mathrm{g/cm^3}$. The absorbed power is only 3 W at an energy of 30 MeV and an electron current of 100 nA. Although it depends on the absorbing volume, cooling should be unnecessary because the thermal conductivity is more than six times higher than austenite steel and twice as high as iron.

Electrons

An electron beam with an energy of 30 MeV hitting a block of graphite has been simulated by Geant4. Figure 7.1 shows the depth where each electron has been stopped and the energy

deposited to the material. Each point stands for one electron. All (99.4 %) primary electrons (points above the zero line) are stopped within 100 mm. Electrons produced by further processes (points below the zero line) are not stopped at a threshold, but the amount decreases continuously. One primary electron produces about thirty secondary electrons with lower energy, where about the half is also stopped within 100 mm. The transmission of secondary electrons decreases nearly exponentially with the depth. 96 % of the electrons that are not stopped within 100 mm have energies below 500 keV. This fraction decreases slightly at larger depths. The amount of backscattered secondary electrons can be neglected. From the simulations it is about 0.1 % relative to the primary electrons.

The deposited energy of the electrons was averaged over spatial cubes with a volume of $1\,\mathrm{mm}^3$ and checked for maximum power density. The power density does not exceed a value of $12.3\,\mathrm{mW}/(\mathrm{mm}^3\mu\mathrm{A})$ and is located in a cylindrical volume of radius 1 mm and a depth of 25 mm directly at the point where the electrons impinge. Outside this volume the power density is less than a half of the maximum and vanishes very quickly. This power has to be led away by the thermal conductance of graphite which is about $\lambda = 160\,\mathrm{W}/(\mathrm{K}\cdot\mathrm{m})$. Assuming an infinite cylinder with a radius of $l_0 = 1\,\mathrm{mm}$ and a constant power density of the above given value the thermal power is about 3.9 mW per millimetre length per microampere. The differential thermal resistance is

$$dR = \lambda^{-1}\frac{dl}{A(l)},$$

where $A(l)$ is the conducting area, name the surface of the surrounding cylinder $A(l) = 2\pi l \cdot h$, and l the conducting length. After integration, for the total conductance it follows that

$$G/h = R^{-1}/h = \frac{\lambda}{\ln(l/l_0)} = 23\,\mathrm{mW}/(\mathrm{K}\cdot\mathrm{mm})$$

with a large $l = 1000\,\mathrm{mm}$. The ratio to the thermal power of $3.9\,\mathrm{mW}/(\mathrm{mm}\mu\mathrm{A})$ gives the temperature difference of the hot spot to a point at a distance of 1000 mm. A value of $170\,\mathrm{mK}/\mu\mathrm{A}$ shows that cooling is unnecessary.

Photons

Although graphite is used as a beam-dump core, the electrons stopped in matter produce at this energy a large amount of bremsstrahlung. From simulations, on average 1.1 photons with energies of more than 25 keV are produced per electron. The energy spectrum is a bremsstrahlung spectrum as described in chapter 3 with the endpoint energy at 30 MeV.

For further shielding the energy-angle distribution of the produced photons is interesting. Figure 7.2 shows that high-energy photons are emitted at small angles in the forward direction. At energies around 10 MeV and angles around 0° an accumulation of photons is identifiable. Plenty of backscattered photons with angles above 90° are produced with energies below 500 keV. The albedo is 66 % which requires a special design of the beam dump, to not let these backscattered photons hit the focal-plane detectors or the photomultiplier tubes.

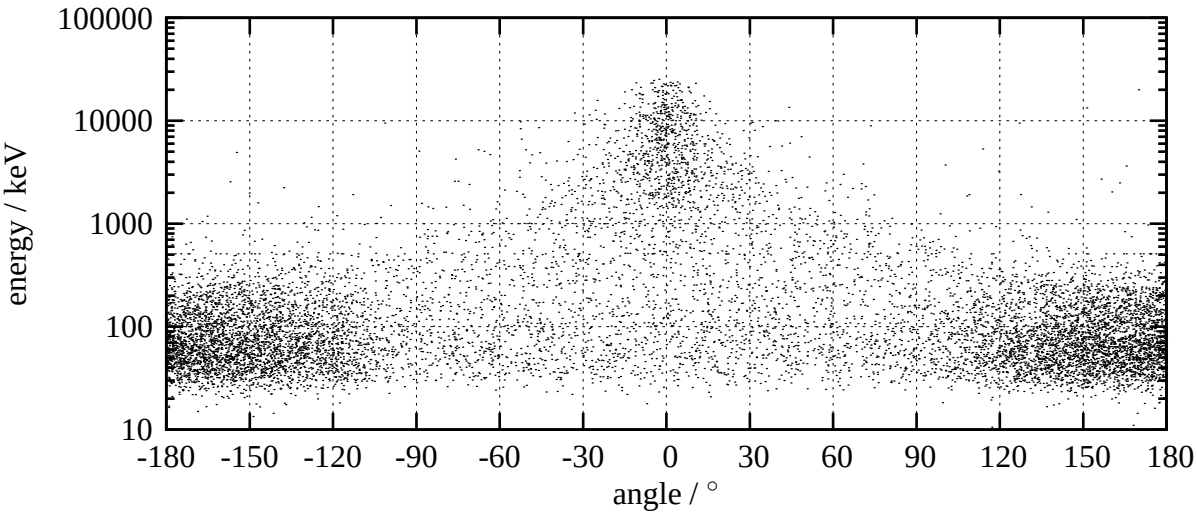

Figure 7.2: The energy-angle distribution of the photons that are emitted in the graphite core of the beam dump. The abscissa shows logarithmically the photon energy and the ordinate the emission angle with respect to the incoming beam. A high-energy bulk can be identified at zero degree and 10 MeV. The backscattered photons at more than 90° have energies below 500 keV.

Photons can be absorbed with high-Z material, such as lead, which surrounds the carbon core. The absorption coefficient of photons in lead has a minimum at 4 MeV with $1\,\mathrm{cm}^{-1}$. At higher energy the pair production raises the coefficient slightly. At lower energies photo absorption predominates the interaction. At 500 keV the coefficient is about $2\,\mathrm{cm}^{-1}$ and the transmitted intensity decreases exponentially with the thickness. So for the backscattered electrons only the half of the thickness of lead is needed compared to the forward direction.

The simulation of the graphite core with lead walls produces as well some neutrons, but the count rate is negligible. The neutron production yield is 10^{-4} per incoming electron.

7.3.2 Design

As mentioned before, the magnetic spectrometer is installed vertically and the beam dump has to be on top of the magnet as shown in figure 7.4. Then an additional handicap is that the distance to the focal-plane detectors cannot be very high. For stability reasons the centre of mass has to be kept low and the total weight should be below 1.5 t to ensure easy handling.

The shielding of photons emitted in forward direction from the graphite core is simply done by placing a thick lead wall behind the graphite. The shielding of the backscattered photons is complicated because they can always leave the beam dump where the electron beam has entered and the entrance has to be large to allow different magnetic field strengths in the spectrometer with one electron energy. The front wall (the right graphite/lead wall in the picture)

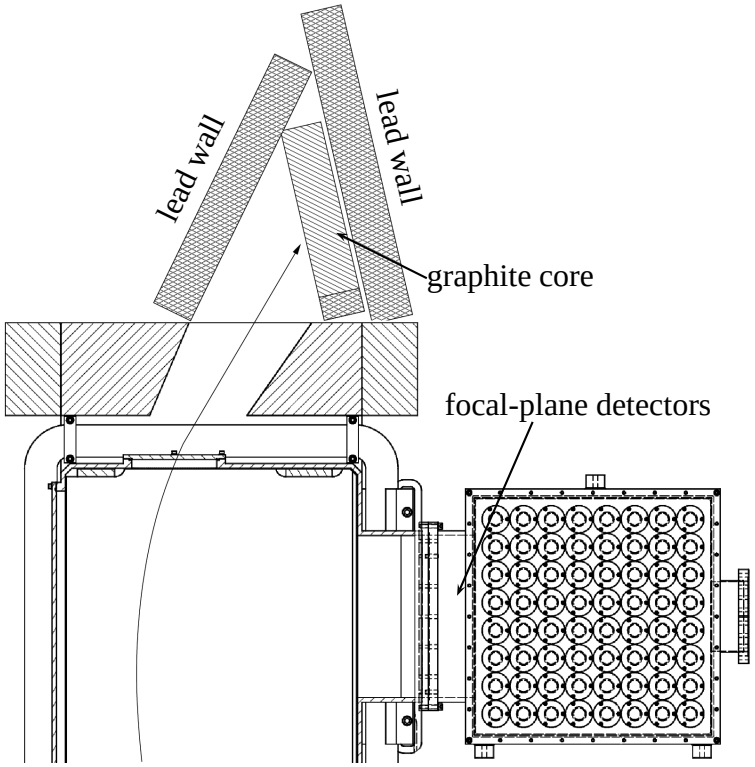

Figure 7.4: On top of the magnet is the beam dump, which consists of a graphite core and is surrounded by lead. The geometry is designed so that all bremsstrahlung photons produced in graphite and emitted in the direction of the focal-plane detectors or photomultiplier tubes have to transit a long way through lead. The angles of the lead walls are chosen to keep to total size small.

is aligned nearly vertically so that every particle that is scattered in direction of the focal-plane detectors or the photomultiplier tubes has to transit a long way through lead. The base of the graphite core is as well shielded with lead bricks. The back wall (the left lead wall in the picture) and the two side walls are simply made of lead. A much simpler design with four vertical walls and a horizontal roof, that has the same shielding properties, is possible, but would be much larger and heavier.

Beneath the beam dump a 10 mm thick plate made of polyvinyl chloride (PVC) with a very high electrical resistivity of $10^{15}\,\Omega$m allows one to measure the electronic current of the stopped electrons.

8 First test experiments

The first test experiments with electrons from the accelerator have been performed in December 2006. Besides of detecting tagged photons directly an important aim was to check the performance of the tagging facility and to determine the experimental constraints. Later an overview is given on experimental parameters for future experiments.

8.1 Performance of the system

The experimental constraints of the spectrometer are important for every experiment planned with the tagging facility. Here the focus is on the range of the spectrometer in low-energy mode and produced background. The energy resolution is discovered to be the energy resolution of the accelerator, which is not the limit of the tagging facility. A method to estimate the momentum spread of the accelerated electrons is given on the basis of beam profile measurements.

8.1.1 Spectrometer range

As discussed in section 4.6 in low-energy mode the spectrometer range is limited by the small hole in the yoke of the magnet. The size of the hole was limited by the quality of the magnetic field in the spectrometer, but there is still a small range of the magnetic field which bends the electrons of the main beam to the beam dump, compare figure 7.4.

For this measurement the incoming electron energy was 28.2 MeV and the beam was bent into the beam dump at a coil current of about 104 A which corresponds to a maximum field of 294 mT. The data was taken with a radiator, because the large scattering angles broaden the beam which reduces the range.

To measure the momentum range that could be detected by the spectrometer with a fixed beam energy, the magnetic field was altered and the beam current measured in the beam dump. Having too high or too low magnetic field strength the beam dump was not hit and the current decreased.

As seen in figure 8.1 there is a 10-percent range within which the beam dump was hit. The range from 99 A to 108 A corresponds to the momentum range of 20.6 MeV/c to 22.6 MeV/c in the centre of the focal plane, see table C.1. The resulting photon range is 5.6 MeV to 7.6 MeV. The ratio

$$\frac{K_i}{K_0} = 1.30$$

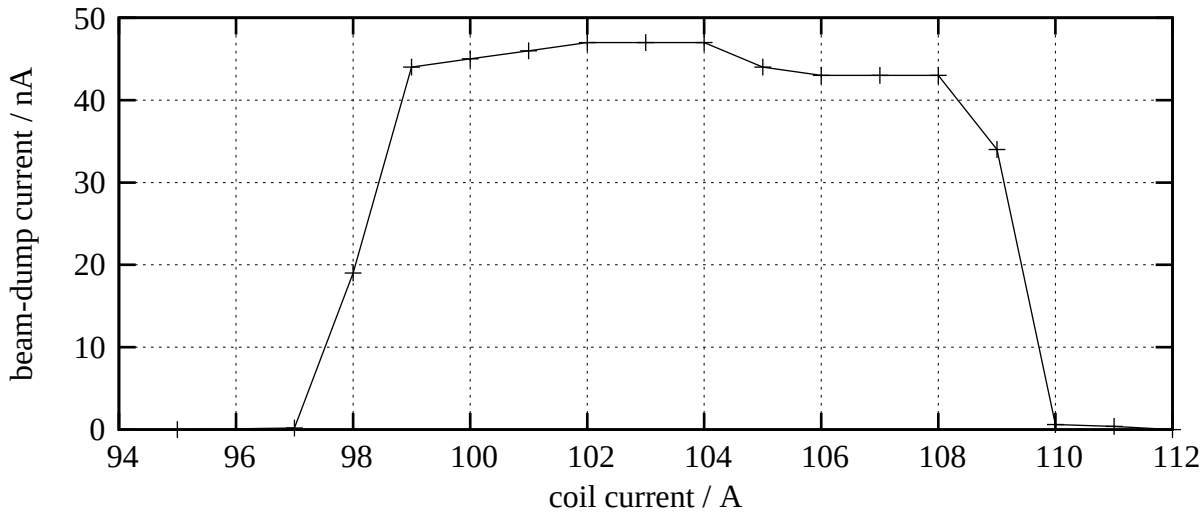

Figure 8.1: The current in the beam dump at different magnetic field strengths and the same beam energy. The beam current measured in the beam dump is a good quantity to show how well the beam is led through the magnets hole. Only the points correspond to measured values. The lines are only eye guides.

which has to be compared with the calculated value of $K_{\mathrm{BD}} = 1.38 \cdot K_0$ in section 4.6. The difference is explained by the active field clamps that have not been excited by the additional correction coils in this test.

The slight loss of beam current at coil currents higher than 104 A could not be explained during the test, but the background did not increase significantly, so it is expected that the beam is still dumped completely in the beam dump.

The width of the "edges" in the plot of the currents in the beam dump is a quantity that describes the width of the beam in the beam dump. Only with sharp edges a large magnetic range is usable. A detailed view of the edge is plotted in figure 8.2. This data is the integral of the electron-beam distribution in the dispersive direction of the magnet. And the first derivative is the beam profile in this direction, shown as smooth solid line. The width is defined by the initial width, the scattering angles behind the radiator and the energy spread of the incoming electron beam. If no scattering occurs and the initial width is about one millimetre the measured width is directly correlated to the momentum definition of the electrons. Since the data was not taken without the radiator, these conditions do not apply, but this determination of the energy spread should be done as a showcase. Here the full width at half maximum is 1.6 A from 97.3 A to 98.9 A. This corresponds to a momentum range in the centre of the focal plane of 320 keV, see table C.1. As evaluated in section 4.6 the momentum in the beam dump is a factor K_{i}/K_0 greater than in the focal plane. This would result in a momentum uncertainty of the electron beam of about 400 keV at 28.2 MeV. At most 0.5 % was expected before the experiment was started. In future experiments the beam width has to be measured without the radiator to obtain

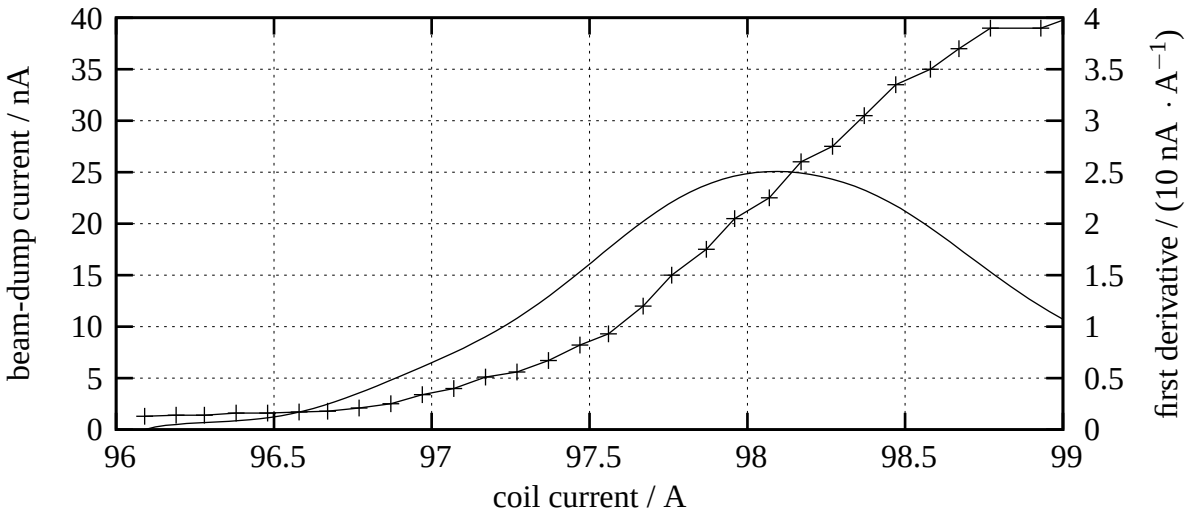

Figure 8.2: A detailed scan of the increasing beam current with increasing coil current is displayed as crosses. This "edge" is a quantity for the size of the beam in the beam dump. Only the points correspond to measured values. The lines are only eye guides. The smooth line is a full-degree bézier curve of the differential points of the edge.

the initial momentum uncertainty. Furthermore the comparison between a measurement with and without radiator leads to an estimate for the energy loss in the radiator.

The size of the hole in the yoke is 265 mm which corresponds to the coil-current range from 99 A to 108 A. The spatial full width at half maximum is then 47 mm.

8.1.2 Background measurements

The main function of the beam dump is to absorb the beam completely without producing too much background. To analyse the effect of the beam dump the count rate in the focal plane is monitored as a function of the coil current. This data was taken without a radiator to avoid a count rate from degraded electrons. Much effort for optimising the beam quality in the beam line was necessary to minimise the count rate in the focal plane detector to about $100 \cdot 10^3\,\mathrm{s}^{-1}$ when hitting the beam dump.

This data is displayed in figure 8.3 with the beam current in the beam dump. It shows that at low magnetic field strength the background is at a minimum. Here the beam is dumped at the back plane of the spectrometer. From 50 A to 80 A the background increases to $280 \cdot 10^3\,\mathrm{s}^{-1}$. Then, from 90 A to 100 A, although the beam dump is not hit the background decreases again down to $110 \cdot 10^3\,\mathrm{s}^{-1}$. When hitting the beam dump, between 100 A and 110 A, the background is still around $110 \cdot 10^3\,\mathrm{s}^{-1}$. At higher magnetic field strength the background increases again to over $150 \cdot 10^3\,\mathrm{s}^{-1}$. Obviously, the beam is dumped completely and additional background is

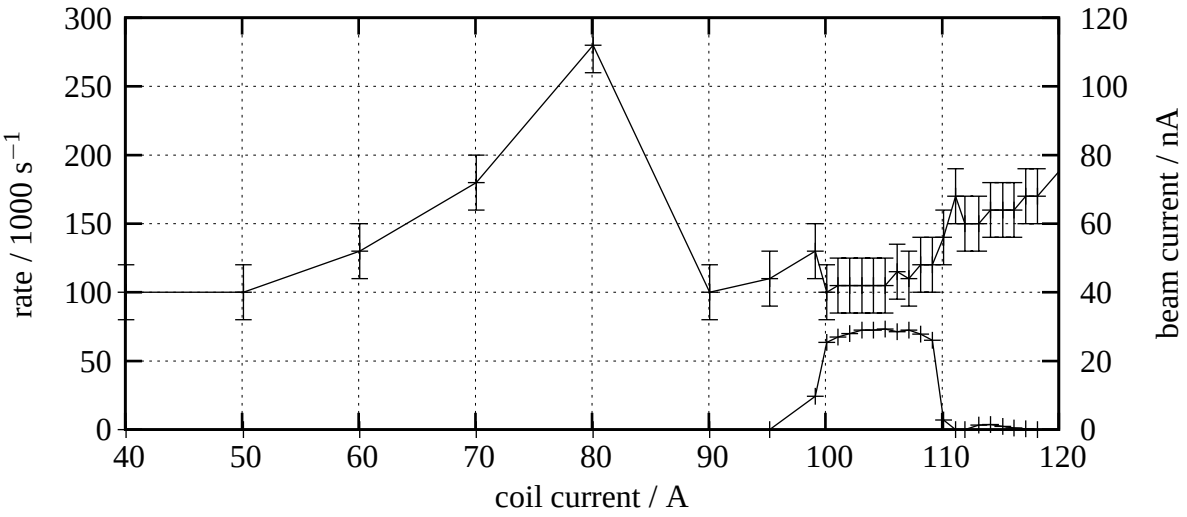

Figure 8.3: The upper curve shows the count rate on the left ordinate in one detector element in the focal plane. The lower curve shows the current detected in the beam dump on the right ordinate. Both data are taken as a function of the coil current. The lower limit of $100 \cdot 10^3\,\mathrm{s}^{-1}$ is the minimum that is observed from 0 A to 50 A and is basically background from the accelerator.

kept very low. The beam current of 30 nA is a typical current for experiments.

To shield the focal plane detectors and the photomultiplier tubes from background produced in the beam line a large block of concrete ($80 \times 120 \times 120\,\mathrm{cm}^3$) was placed directly in front of the detector chamber. The position has been optimised by some background measurements. The former background of about $100 \cdot 10^3\,\mathrm{s}^{-1}$ could be reduced to less than $30 \cdot 10^3\,\mathrm{s}^{-1}$ at the same beam current.

The background at the experimental place a few centimetres next to the collimated photon beam is not higher than the background without beam. This has been measured with a Ceriumtetrafluorid photo detector. A high count-rate could be produced if the magnetic field was turned down to check the operation of the detector. So it is known, that every event detected at the experimental place stems from the target in the photon beam.

8.2 First tagged photons

The simplest experiment to demonstrate the operation of the tagging facility is to measure the photons directly in coincidence with one focal-plane detector, see figure 8.4. For that purpose only analogous electronics was used for the timing and to generate a gate for an ADC. The ADC digitised the energy signal from a high-purity germanium detector whose energy resolution is better that of the tagging facility.

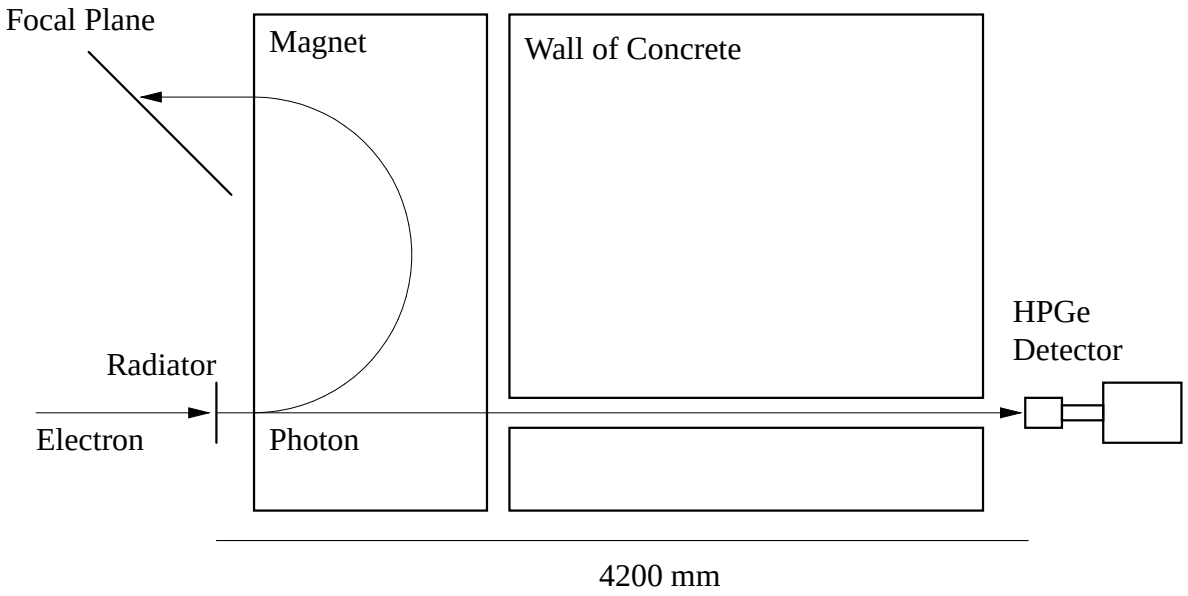

Figure 8.4: The electron beam hits the radiator from the left side and the degraded electron is detected in the one detector element of the focal plane. The tagged photon leaves the magnet at the rear side and is collimated in a copper collimator which is located inside a thick wall of concrete. The HPGe detector analyses the energy and a simple coincidence electronic system assigns the photon event with the electron hit in the focal plane.

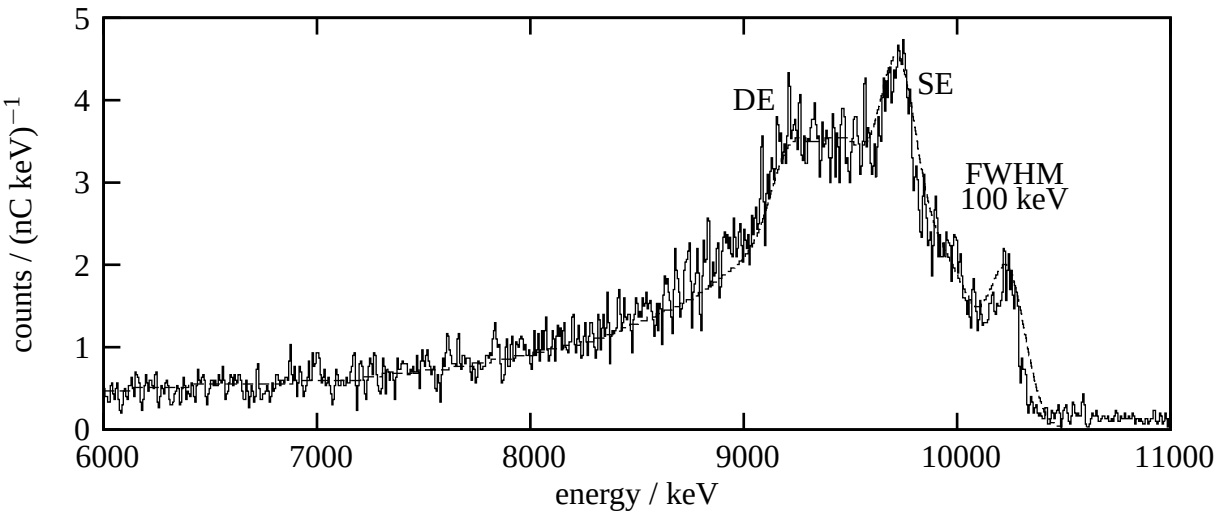

Figure 8.5: The energy signal that is generated by the germanium detector. The histogram is normalised to the collected charge in the beam dump. The dashed line is a Monte-Carlo simulation of the detector response. It shows that the right peak at 10250 keV is the full-energy peak and the peaks at 9740 keV and 9230 keV are the single and double-escape peaks.

Figure 8.5 shows the energy signal as a histogram. It is normalised to the collected charge in the beam dump. The absolute accuracy of the normalisation is not very high, because the beam current was very low and impossible to monitor. From higher and measurable currents the beam intensity was extrapolated linearly by the background as seen in the focal-plane detectors. With this calibration a beam current of $40(30)$ pA was estimated. Higher currents led to very high rates in the detector, which was limited to $15 \cdot 10^3\,\mathrm{s}^{-1}$. The dashed line shows a Monte-Carlo simulation of the detector response for the expected photon beam. This region of the energy spectrum is dominated by the full-energy peak at 10250 keV and the single and double-escape peaks from pair production and subsequent positron annihilation at 9740 keV and 9230 keV. The spectrum also includes the deposited energy from Compton scattering that overlays the full range up to 10000 keV. Although the width of the full-energy peak seems to be smaller the simulations could only reproduce the spectrum quite well with an energy width of about 100 keV. This is the energy resolution that is obtained in the experiment and not the desired resolution of 25 keV. In this experiment we expected an energy definition of the beam of some 10^{-3} at 28.2 MeV and the focal-plane detectors were not at the ideal position in the focal plane, where photons would be tagged with an energy of 7.8 MeV.

The sum of all counts in this spectrum is 20026. Due to the low intrinsic efficiency of the detector and the large dead time of about $7.8(10) \cdot 10^7$ tagged photons (width: $100(20)$ keV) have reached the detector after collecting 700 nC. So the measured value is 1.1(8) photons per MeV and fC.

From figure 3.5 about 3 photons per MeV and fC are expected in the full solid angle and from figure 3.8 about 20 % of all of them reach the detector which was at a distance of 3.6 m and has a radius of 50 mm. The measured value is twice as large but agrees with the simulation within the systematic errors.

The count rate in a focal-plane detector was only a few $100\,s^{-1}$. The limit of $10^6\,s^{-1}$ was reached at about 80 nA which is a factor of 2000 higher than in this experiment. Nevertheless this current should be possible in experiments. But one has to keep in mind that this is a very far extrapolation and the direct detection of tagged photons with high energy resolution is not possible at a high current.

8.3 Future experiments

This section deals with the two main classes of experiments which can be performed at the photon tagging facility. The first class consists of “prompt coincidence experiments”i where only fast particles emitted from the target have to be detected. Experiments with slow particles, when no constant time difference within a few nanoseconds between emission and detection exists, form the second class, the “delayed coincidence experiments”. The distinction between fast and slow particles has to be done depending on the needed gate width of the coincidence. Massive particles need different times-of-flight from the point of emission to the point of detection. For example if time differences of about 100 ns should be regarded as coincident, on average ten electron events have been detected in the focal plane. Then the coincidence is delayed and has be treated in a different way. For time differences of less than 10 ns only one electron event corresponds to the trigger and standard electronics can be used.

The expected flux density at the target position at a 4.2 m distance from the radiator is $10^2\,cm^{-2}keV^{-1}s^{-1}$ and is constant on the central area of $10\,cm^2$. At larger angles the flux density decreases and reaches half its value at a radius of 75 mm, as is shown in figure 3.8. The beam is collimated to a radius of 60 mm.

8.3.1 Prompt coincidence experiments

In nuclear resonance-fluorescence experiments with germanium detectors the total time resolution is about 20 ns. At the full rate in the focal-plane detectors of 100 MHz typically two electron events are detected and both should be recorded, as discussed in chapter 6. If the total time resolution is less, the gate has to be longer and more random coincidence background will be produced. Of course experiments with massive particles can be performed if the differences in time-of-flight are small.

For prompt coincidence experiments simple standard electronics can be used and the timing and gate generation can be done completely in hardware.

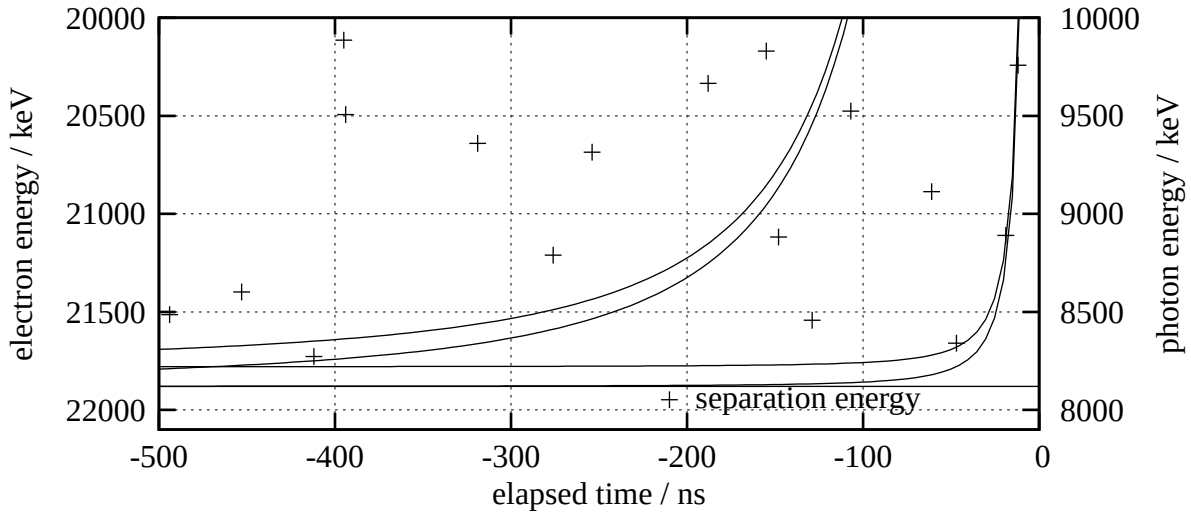

Figure 8.6: Time-of-flight spectra for different detector distances and one excited state. The plot is similar to figure 6.1. Here the distances of the detector from the target is 0.2 m (right curves) and 2 m (left curves).

8.3.2 Delayed coincidence experiments

If the difference in time-of-flight of massive particles is in the order of 100 ns background events occur very frequently if a fixed time window is chosen. The idea is to have different time windows for different focal-plane detectors. Particles with short times-of-flight are produced by photons with high energy that correspond to electrons with low momentum in the focal-plane detector. By tuning this window off-line it is possible to erase many background events from the data. To accomplish this requirement a special multi-hit TDC has to be used, see chapter 6.

Nevertheless the particle detectors should be arranged very close to the target, because then the maximum time-of-flight is kept small and less background is recorded. With large distances the chance for additional electron events that could be assigned to the slow particle increases.

If one is interested in the final states of the target nucleus one has to increase the distance of the particle detectors to the target. Then the energy of the travelling particle could be determined by the time-of-flight. Figure 8.6 shows the time-of-flight dependence for different particle energies as a function of the detector distance. A close detector (10 cm) does not distinguish between particle energies that differ by 100 keV if the kinetic energy is above 500 keV. A distant detector can separate these energies up to higher energies.

K_i/K_0	$1.1K_0$	$1.0K_0$	$0.9K_0$
1.30	4.6 MeV – 6.9 MeV	5.8 MeV – 8.1 MeV	6.9 MeV – 9.2 MeV
1.45	7.2 MeV – 9.3 MeV	8.3 MeV – 10.3 MeV	9.3 MeV – 11.4 MeV
1.70	10.6 MeV – 12.3 MeV	11.5 MeV – 13.2 MeV	12.3 MeV – 14.1 MeV

Table 8.1: This gives an overview about the possible photon energy ranges of the photon tagging facility. The values are valid for a beam momentum of 30 MeV/c and scale linearly. The left column shows the ratio of the momentum of the incoming beam and the momentum in the centre of the focal plane. The first two rows show the lower and the upper limit in low-energy mode and the third row shows the minimum for high-energy mode. The three right columns are the ranges for different placements of the focal-plane detectors.

8.3.3 Parameters of the tagging facility

The energy range of the photon tagging facility depends on the possible energy range of the accelerator, the operation mode of the spectrometer and the location of the focal-plane detectors in the focal plane. In low-energy mode the ratio of accelerator momentum and the electron momentum in the centre of the focal plane varies from 1.30 to 1.45 by varying the magnetic field strength, as discussed in section 4.6 and previously in this chapter. So at a typical momentum of the electron beam of 30 MeV/c the energy range of tagged photons in the centre of the focal plane is from 6.9 MeV to 9.3 MeV. The focal-plane detectors can be arranged at 10 % higher momentum and 10 % lower momentum. This gives a total range in low-energy mode of 4.6 MeV to 11.4 MeV. Of course this photon energy scales linearly with the accelerator momentum. The energy range that can be tagged simultaneously depends on the amount of detector elements in the focal plane. One detector element covers roughly 10^{-3} of the momentum so with 128 detectors it is about 10 %, which is half the accessible focal plane.

The photon-energy ranges for an electron-beam momentum of 30 MeV/c are tabulated in 8.1. The quantity K_0 denotes the momentum that is focused in the centre of the focal plane, and $1.1K_0$ and $0.9K_0$ are the momenta at the upper and lower end of the accessible region. The range stems from the 128 detector elements that are arranged in the focal plane. In the first column the ratio of the momentum of the incoming beam K_i to K_0 is shown. The first two rows are the lower and the upper limit in low-energy mode where the beam is dumped in the beam dump on top of the magnet. The third row is the lower limit for high-energy mode, where the main beam leaves the magnet at the rear side. The range can easily be calculated by the formulas given earlier in this work. The photon energy is given by energy conservation as

$$E_\gamma = E_i - E_0$$

where E_i is the incoming electron energy and E_0 is the energy of the electrons that are detected in the middle of the focal plane at $K = K_0$. The electrons' energies are given by their momenta

and their negligible rest mass as

$$E_{i/0} = \sqrt{p_{i/0}^2 c^2 + m^2 c^4} \approx pc.$$

The ratio $K_i/K_0 = E_i/E_0$ is fixed for a given momentum of the incoming beam and a given magnetic field strength. So the photon energy is

$$E_\gamma = E_i(1 - K/K_i)$$

where K denotes the position on the focal plane, of which the range between $0.9K_0$ and $1.1K_0$ is accessible.

9 Final remarks and outlook

The photon tagging facility has been developed and constructed to fulfil the experimental requirements of a high energy resolution of 25 keV at a photon energy of 10 MeV, a photon range of at least 6 MeV to 20 MeV, and a full tagging rate of $10^4\,\mathrm{keV}^{-1}\mathrm{s}^{-1}$. These preconditions define already many of the apparatus parameters. The energy resolution can only be reached if the size of a detector element in the focal plane corresponds to 25 keV. This in turn defines the minimum count rate per detector for true coincidences of $2.5 \cdot 10^5\,\mathrm{s}^{-1}$ to achieve $10^4\,\mathrm{keV}^{-1}\mathrm{s}^{-1}$. With the scintillating fibres and the photomultiplier tubes a maximum count rate of $1 \cdot 10^6\,\mathrm{s}^{-1}$ to $2 \cdot 10^6\,\mathrm{s}^{-1}$ can be processed. This allows a signal-to-noise ratio of at least $1/5$. As discussed in chapters 1 and 6, it does not cause many random coincidences. The drawback of the fibres as detector elements is the minimum width of about 1 mm [End07], which demands a large focusing magnet to reach a dispersion of at least $1.25 \cdot 10^{-3}\,\mathrm{mm}^{-1}$. The financial budget even allowed a larger magnet to reach $0.9 \cdot 10^{-3}\,\mathrm{mm}^{-1}$. The specification of a total tagging rate of $10^4\,\mathrm{keV}^{-1}\mathrm{s}^{-1}$ also defines already the flux density at the target position due to the photon angles. The expected flux density is about $100\,\mathrm{cm}^{-2}\mathrm{keV}^{-1}\mathrm{s}^{-1}$ at four metres behind the radiator, see chapter 3. A factor of one hundred could be gained with polycrystalline diamond detectors in the focal plane, but there were no standard electronics available and not even the experience in detecting single electron events [Ber04]. Of course this is an option for a future upgrade.

The experiment has shown that the momentum definition of the accelerator can be reached. Better resolution is expected after the upgrade of the radio-frequency control units. The simulated photo-production yield of three photons per MeV and fC could be confirmed within a large error which originates from the insufficient estimation of the beam current below values of 250 pA.

The test experiment has been performed with 32 of the 128 focal-plane detectors. Until spring 2008 the complete set of detectors will be tested and installed at the tagging facility. During 2008 first (γ,n) experiments with fast neutrons will be performed. Experiments with slow neutrons (below 200 keV) need new detectors that will be delivered during the second half of 2008. The low-energy limit of experiments with slow particles depends highly on the detection efficiency in this range.

A CAD drawing

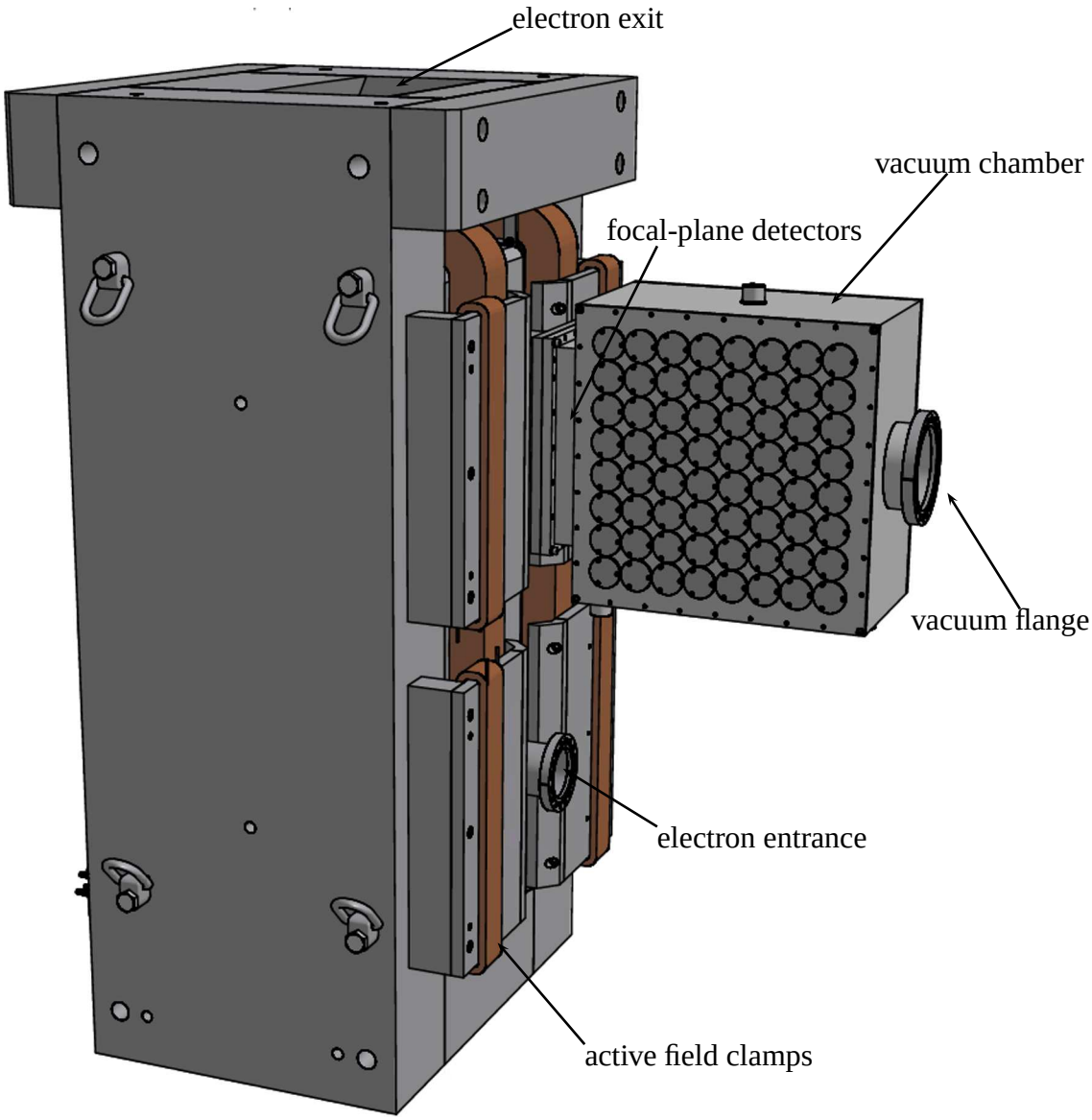

A CAD drawing of the tagging spectrometer. The radiator is placed before the electron entrance. The full height is 1850 mm and the full weight is 9000 kg.

B Data from raytracing

B.1 Focal plane

K/K_0	r/mm	z/mm @ 5 %	z/mm @ 50 %	z/mm @ 95 %	$\Delta K/(10^{-3}K_0)$
0.9168	106	-637.1	-637.0	-636.2	0.0000
0.9202	102	-640.7	-640.6	-639.8	0.8738
0.9236	99	-644.3	-644.2	-643.4	0.8661
0.9270	95	-647.9	-647.7	-647.0	0.8547
0.9304	91	-651.5	-651.3	-650.6	0.8303
0.9338	87	-655.1	-655.0	-654.2	0.8149
0.9372	82	-658.7	-658.6	-657.8	0.8094
0.9406	77	-662.4	-662.2	-661.5	0.8217
0.9440	73	-666.0	-665.9	-665.1	0.8425
0.9474	70	-669.7	-669.6	-668.8	0.8395
0.9508	66	-673.4	-673.2	-672.5	0.8067
0.9542	62	-677.0	-676.9	-676.2	0.7699
0.9576	57	-680.7	-680.6	-679.9	0.7266
0.9610	52	-684.4	-684.4	-683.7	0.6949
0.9643	47	-688.2	-688.1	-687.4	0.7078
0.9677	43	-691.9	-691.8	-691.1	0.7226
0.9711	38	-695.7	-695.6	-694.9	0.7289
0.9745	35	-699.5	-699.4	-698.6	0.7509
0.9779	30	-703.3	-703.2	-702.4	0.7461
0.9813	26	-707.1	-707.0	-706.2	0.7523
0.9847	20	-710.9	-710.8	-710.1	0.7187
0.9881	16	-714.7	-714.6	-713.9	0.7276
0.9915	12	-718.6	-718.4	-717.7	0.7225
0.9949	8	-722.4	-722.3	-721.6	0.6875
0.9983	3	-726.2	-726.2	-725.5	0.6560
1.0017	-1	-730.1	-730.0	-729.4	0.6281
1.0051	-6	-734.0	-733.9	-733.3	0.6174

Table B.1: Ray-tracing data for the focal plane, continued on next page.

K/K_0	r/mm	z/mm @ 5 %	z/mm @ 50 %	z/mm @ 95 %	$\Delta K/(10^{-3}K_0)$
1.0085	-11	-737.9	-737.8	-737.2	0.6137
1.0119	-15	-741.8	-741.7	-741.1	0.6202
1.0153	-20	-745.7	-745.7	-745.0	0.6396
1.0187	-26	-749.7	-749.6	-748.9	0.6499
1.0221	-30	-753.7	-753.6	-752.9	0.6523
1.0255	-35	-757.6	-757.5	-756.9	0.6416
1.0289	-39	-761.6	-761.5	-760.9	0.6443
1.0323	-44	-765.6	-765.5	-764.9	0.6312
1.0357	-49	-769.6	-769.5	-768.9	0.6341
1.0390	-55	-773.6	-773.6	-772.9	0.6271
1.0424	-59	-777.7	-777.6	-776.9	0.6109
1.0458	-64	-781.7	-781.6	-781.0	0.6178
1.0492	-69	-785.8	-785.7	-785.1	0.5979
1.0526	-74	-789.8	-789.7	-789.1	0.5910
1.0560	-79	-793.9	-793.8	-793.2	0.5699
1.0594	-84	-798.0	-797.9	-797.3	0.5582
1.0628	-89	-802.1	-802.0	-801.4	0.5833
1.0662	-94	-806.3	-806.1	-805.5	0.5885
1.0696	-99	-810.4	-810.3	-809.7	0.5799
1.0730	-105	-814.5	-814.4	-813.8	0.5806
1.0764	-110	-818.7	-818.6	-818.0	0.5868
1.0798	-118	-822.9	-822.8	-822.2	0.5951
1.0832	-123	-827.1	-827.0	-826.4	0.5923
1.0866	-126	-831.3	-831.2	-830.6	0.5871
1.0900	-132	-835.6	-835.4	-834.8	0.5774
1.0934	-138	-839.8	-839.7	-839.1	0.5989
1.0968	-146	-844.1	-843.9	-843.3	0.6050
1.1002	-150	-848.3	-848.2	-847.6	0.6045
1.1036	-156	-852.6	-852.5	-851.9	0.5944
1.1070	-161	-856.9	-856.8	-856.2	0.5995
1.1104	-167	-861.3	-861.1	-860.5	0.6146
1.1138	-172	-865.6	-865.4	-864.8	0.6204
1.1171	-180	-870.0	-869.8	-869.2	0.6147

Table B.1: Ray-tracing data for the focal plane. The table shows the position of the focus for different momenta K/K_0. Given is the coordinate r and three values for z. The percentage gives the ratio of electron orbits that is at lower z. The rightmost value is the momentum resolution that is derived from the difference of z @ 5 % and z @ 95 %.

C Data from magnetic field measurements

C.1 Current dependence

I/A	$B\uparrow$ /mT	$B\downarrow$ /mT	$B\uparrow$ /mT	$B\downarrow$ /mT	$p_0/(\mathrm{MeV}c^{-}1)$
0	4.2	6.5	6.5	6	0.44
20	56.8	61.9	58.6	62	4.60
25	70.6	75.5	71.3	76	5.64
30	83.5	89.2	84.5	89	6.61
35	97.7	103.0	97.9	103	7.65
40	112.0	116.7	111.4	117	8.69
45	125.5	130.7	124.8	131	9.73
50	140.0	144.4	138.5	144	10.6
55	151.5	158.2	152.0	158	11.7
60	165.2	171.7	165.7	172	12.7
65	178.7	185.5	179.5	186	13.8
70	192.0	199.1	192.9	199	14.7
75	205.5	212.7	206.5	213	15.8
80	219.5	226.3	220.3	227	16.8
85	232.7	240	233.8	240	17.8
90	246.4	254	247.3	254	18.8
95	259.8	267	261.6	267	19.8
100	273.3	281	274.4	281	20.8
105	287	294	287.9	294	21.8
110	300	308	301	308	22.8
115	314	321	315	321	23.8
120	327	334	328	334	24.8
125	341	348	341	348	25.8
130	354	360	354	360	26.7
135	366	373	367	373	27.7

Table C.1: Magnetic field data for different currents, continued on next page.

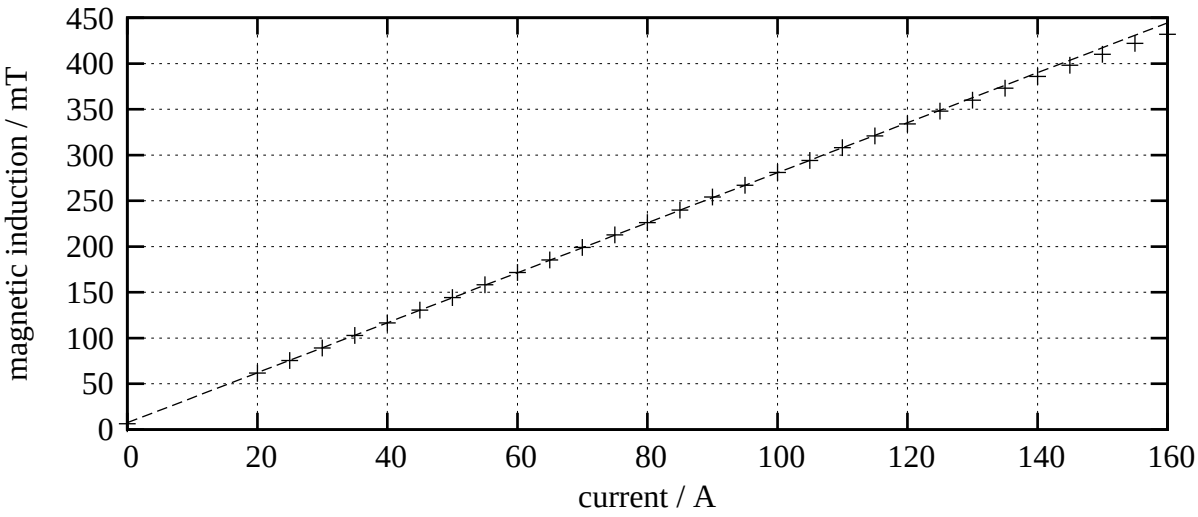

Figure C.1: The data of the fourth column of table C.1 is plotted. Above 110 A the effect of magnetic saturation is noticeable.

I/A	$B\uparrow$ /mT	$B\downarrow$ /mT	$B\uparrow$ /mT	$B\downarrow$ /mT	$p_0/(\mathrm{MeV}c^{-}1)$
140	380	386	380	386	28.6
145	393	398	394	398	29.5
150	406	410	406	410	30.4
155	419	422	420	422	31.3
160	432	432	432	432	32.0

Table C.1: The strength of the magnetic field at a point in the mid-plane at $r = 314$ mm. The first column is the set value for the current in the magnet. The absolute uncertainties are on the order of 5 mA and the relative stability is more than one order of magnitude below. The field was measured four times, twice with increasing current ($B\uparrow$) and twice with decreasing current ($B\downarrow$). The last column is the according momentum that is related to $K = K_0$.

To determine the associated momentum $p = \gamma mv$ equation (C.1) can be used,

$$p_0 = f(r) \cdot K_0 \cdot eB_0, \tag{C.1}$$

where is e is the charge of an electron, $K_0 = 0.7426$, and B_0 the product of the magnetic field B and the coordinate r. Of course this is only true if r is measured at a location where fringe effects do not disturb. This is definitely not true for the point at $r = 314$ mm as shown in figure C.2.

This behaviour can be taken into account by a factor $f(r)$ that corrects the deviation, see

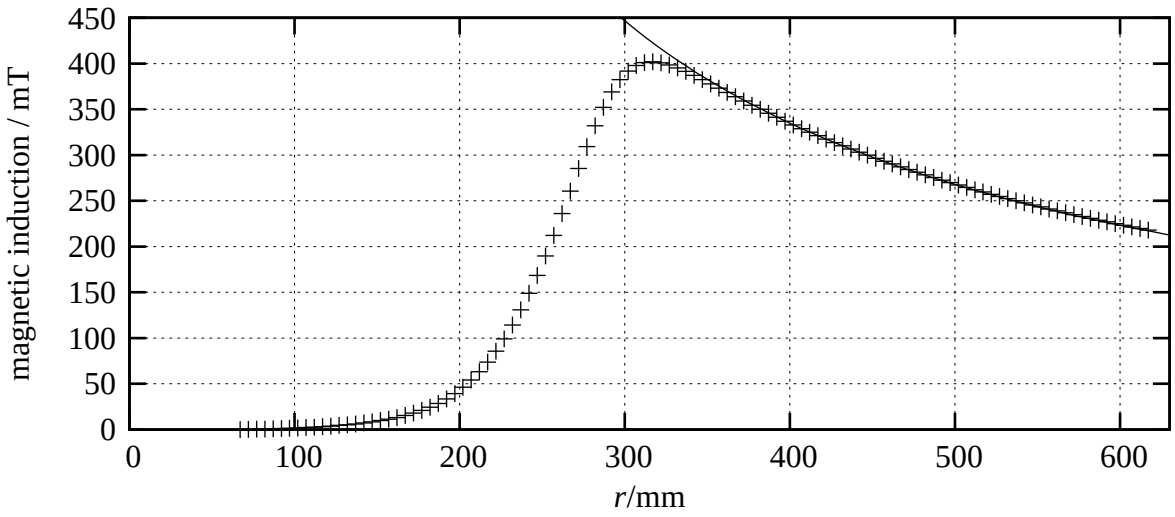

Figure C.2: Plotted is the measured magnetic induction and the calculated $1/r$ dependence of the magnet. Differences are due to fringe-field effects, especially up to 350 mm.

figure C.3. For $r = 314$ mm this factor is 1.062, see table C.2. The momenta are given in the fifth column of table C.1.

r/mm	$f(r)$	r/mm	$f(r)$	r/mm	$f(r)$	r/mm	$f(r)$
102	709.8	177	36.0686	252	2.80138	327	1.02796
107	553.88	182	30.0257	257	2.45485	332	1.02083
112	439.664	187	24.9566	262	2.166	337	1.01565
117	353.327	192	20.7496	267	1.92555	342	1.01195
122	285.159	197	17.2431	272	1.72647	347	1.00921
127	232.812	202	14.3459	277	1.56317	352	1.00725
132	191.451	207	11.9492	282	1.43091	357	1.00574
137	157.687	212	9.98245	287	1.32544	362	1.00458
142	130.461	217	8.36131	292	1.24294	367	1.00373
147	108.341	222	7.03592	297	1.17963	372	1.00301
152	90.0082	227	5.9486	302	1.13186	377	1.00247
157	74.9663	232	5.05627	307	1.09639	382	1.00202
162	62.4461	237	4.32266	312	1.07037	387	1.00167
167	52.0125	242	3.71805	317	1.05149	392	1.00135
172	43.3102	247	3.21742	322	1.03783	397	1.00112

Table C.2: The fringe field correction factor is the quotient of $1/r$ behaviour and the measured field.

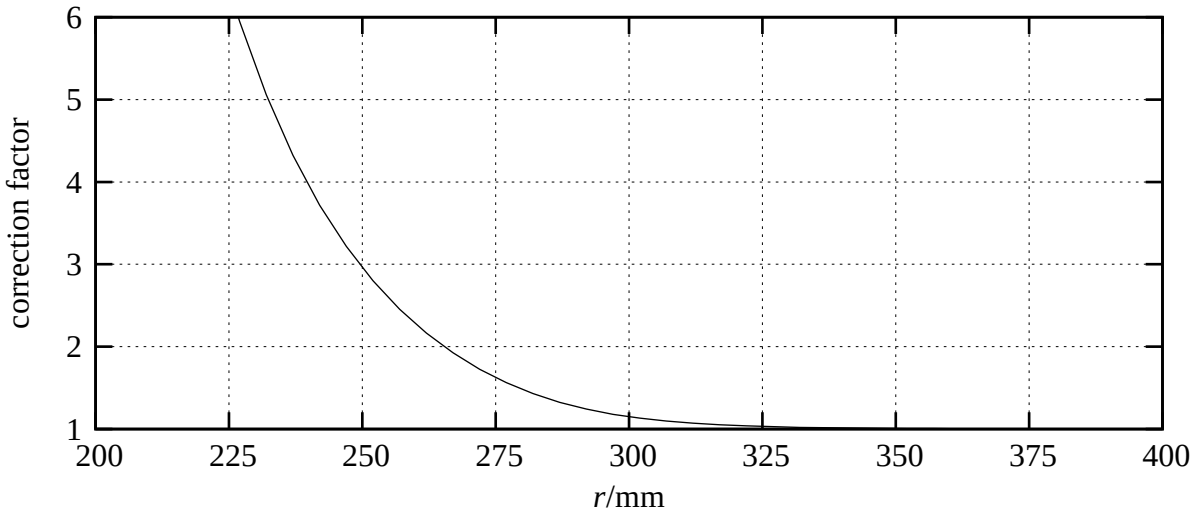

Figure C.3: The relative deviation of $1/r$ and the magnetic field strength as a function of r.

List of Figures

Bibliography

[Abb07] P. Abbon, E. Albrecht, V. Alexakhin, Y. Alexandrov, G. Alexeev, M. Alekseev, A. Amoroso, H. Angerer, V. Anosov, B. Badelek, et al., Nucl. Instr. and Meth. A **577** (2007) 455 (DOI).

[Adl90] J.-O. Adler, B.-E. Andersson, K. I. Blomqvist, B. Forkman, K. Hansen, L. Isaksson, K. Lindgren, D. Nilsson, A. Sandell, B. Schröder, K. Ziakas, Nucl. Instr. and Meth. A **294** (1990) 15 (DOI).

[Adl97] J.-O. Adler, B.-E. Andersson, K. I. Blomqvist, K. G. Fissum, K. Hansen, L. Isaksson, B. Nilsson, D. Nilsson, H. Ruijter, A. Sandell, B. Schröder, D. A. Sims, Nucl. Instr. and Meth. A **388** (1997) 17 (DOI).

[Ago03] S. Agostinelli, J. Allison, K. Amako, J. Apostolakis, H. Araujo, P. Arce, M. Asai, D. Axen, S. Banerjee, G. Barrand, F. Behner, L. Bellagamba, J. Boudreau, et. al, Nucl. Instr. and Meth. A **506** (2003) 250 (DOI).

[All06] J. Allison, K. Amako, J. Apostolakis, H. Araujo, P. A. Dubois, M. Asai, G. Barrand, R. Capra, S. Chauvie, R. Chytracek, G. Cirrone, G. Cooperman, et al., IEEE Trans. Nucl. Sci. **53** (2006) 270 (DOI).

[Ant91] I. Anthony, J. D. Kellie, S. J. Hall, G. J. Miller, J. Ahrens, Nucl. Instr. and Meth. A **301** (1991) 230 (DOI).

[Ara05] A. Araz, *Entwicklung einer Ausleseelektronik und Darstellungssoftware für die nicht-destruktiven Strahldiagnoseeinheiten am S-DALINAC*, Diploma Thesis, Institut für Kernphysik, TU Darmstadt (2005), unbpublished.

[Are82] J. Arends, J. Eyink, A. Hegerath, B. Mecking, H. Rost, Nucl. Instr. and Meth. **201** (1982) 361 (DOI).

[Arg84] P. Argan, G. Audit, J. Bechade, A. Bloch, N. de Botton, G. Colin, J. L. Faure, D. Foucaud, M. L. Ghedira, C. Guerra, J. Martin, E. Mazzucato, C. Schuhl, G. Tamas, E. Vincent, Nucl. Instr. and Meth. A **228** (1984) 20 (DOI).

[Arn07] A. Arnold, H. Büttig, D. Janssen, T. Kamps, G. Klemz, W. Lehmann, U. Lehnert, D. Lipka, F. Marhauser, P. Michel, K. Möller, P. Murcek, C. Schneider, R. Schurig,

F. Staufenbiel, J. Stephan, J. Teichert, V. Volkov, I. Will, R. Xiang, Nucl. Instr. and Meth. A **577** (2007) 440 (DOI).

[Aud70] G. Audit, N. D. Botton, G. Tamas, H. Beil, R. Bergère, A. Veyssière, Nucl. Instr. and Meth. **79** (1970) 203 (DOI).

[Bab02] M. Babilon, T. Hartmann, P. Mohr, K. Vogt, S. Volz, A. Zilges, Phys. Rev. C **65** (2002) 037303 (DOI).

[Bel82] Z. W. Bell, L. S. Cardman, P. Axel, Phys. Rev. C **25** (1982) 791 (DOI).

[Ber04] E. Berdermann, private communication (2004).

[Ber06] E. Berdermann, private communication (2006).

[Bet30] H. A. Bethe, Ann. Phys. **5** (1930) 325.

[Bet34] H. A. Bethe, W. Heitler, Proc. Roy. Soc. (London) **A146** (1934) 83.

[Bet53] H. A. Bethe, Phys. Rev. **89** (1953) 1256 (DOI).

[Blo33] F. Bloch, Ann. Phys. **16** (1933) 285.

[Boh57] A. Bohr, B. R. Mottelson, Nucl. Phys. **4** (1957) 529 (DOI).

[Boh58] A. Bohr, B. R. Mottelson, Nucl. Phys. **9** (1958) 687 (DOI).

[Bru00] M. Brunken, S. Döbert, , H. Genz, H.-D. Gräf, S. Khodyachykh, S. Kostial, U. Laier, H. Loos, A. Richter, S. Richter, B. Schweizer, A. Stascheck, O. Titze, Los Alamos Rep. **LA-13782-C** (2000) 65.

[Cog47] N. D. Coggeshall, J. App. Phys. **18** (1947) 855 (DOI).

[Con07] A. Constantinescu, *Untersuchung der Ablenkeigenschaften eines Dipolmagneten und Entwicklung eines Teilchen-Raytracers*, Bachelor Thesis, Institut für Kernphysik, TU Darmstadt (2007), unpublished.

[Cri70] A. Crispin, G. Fowler, Rev. Mod. Phys. **42** (1970) 290 (DOI).

[Det92] P. Detemple, K. H. Althoff, G. Anton, J. Arends, A. Bock, M. Breuer, K. Büchler, G. Nöldeke, M. Serwazi, W. Schneider, D. Urban, B. Zucht, Nucl. Instr. and Meth. A **321** (1992) 479 (DOI).

[Döb95] S. Döbert, *Extraktion des Elektronenstrahls am S-DALINAC und Messung der transversalen Strahlparameter mit optischer Übergangsstrahlung*, Diploma Thesis, Institut für Kernphysik, TH Darmstadt (1995), unpublished.

[Döb99] S. Döbert, *Nichtlineare Zeitreihenanalyse der Feldamplitude der supraleitenden Beschleunigungsstrukturen und Aufbau eines HF-Monitorsystems zur zerstörungsfreien Strahldiagnose am S-DALINAC*, Doctoral Thesis, Institut für Kernphysik, TU Darmstadt (1999).

[Elv07] M. Elvers, *Aufbau und Entwicklung eines Datenaufnahmesystems für den Niederenergie-Photonentagger NEPTUN*, Diploma Thesis, Institut für Kernphysik, TU Darmstadt (2007), unpublished.

[EMS04] CST - Computer Simulation Technology, Bad Nauheimer Str. 19, D-64289 Darmstadt, Germany, www.cst.com (2004) (Link).

[End07] J. Endres, *Konstruktion und Untersuchung der Fokalebene von NEPTUN*, Diploma Thesis, Institut für Kernphysik, TU Darmstadt (2007), unpublished.

[Eng64] H. Enge, Rev. Sci. Instr. **35** (1964) 278 (DOI).

[Fre97] J. Freudenberger, H. Genz, V. V. Morokhovskii, A. Richter, V. L. Morokhovskii, U. Nething, R. Zahn, J. P. F. Sellschop, Appl. Phys. Lett. **70** (1997) 267 (DOI).

[G4PM] *The Geant4 Physics Manual*, http://geant4.cern.ch (Link).

[Gol53a] J. Goldemberg, Phys. Rev. **93** (1953) 1426 (DOI).

[Gol53b] J. Goldemberg, L. Katz, Phys. Rev. **89** (1953) 1300 (DOI).

[Gre92] W. Greiner, J. Rafelski, *Spezielle Relativitätstheorie*, Verlag Harri Deutsch (1992) (Link).

[gsl06] http://www.gnu.org/software/gsl (2006) (Link).

[Ham79] J. W. Hammer, B. Fischer, H. Hollick, H. P. Trautvetter, K. U. Kettner, C. Rolfs, M. Wiescher, Nucl. Instr. and Meth. **161** (1979) 189 (DOI).

[Har00] T. Hartmann, J. Enders, P. Mohr, K. Vogt, S. Volz, A. Zilges, Phys. Rev. Lett. **85** (2000) 274; Erratum: Phys. Rev. Lett. **86** (2001) 4981 (DOI).

[Har02] T. Hartmann, J. Enders, P. Mohr, K. Vogt, S. Volz, A. Zilges, Phys. Rev. C **65** (2002) 034301 (DOI).

[Har04] T. Hartmann, M. Babilon, S. Kamerdzhiev, E. Litvinova, D. Savran, S. Volz, A. Zilges, Phys. Rev. Lett. **93** (2004) 192501 (DOI).

[Has05] J. Hasper, *Design eines Niederenergie-Photonentaggers am S-DALINAC*, Diploma Thesis, Institut für Kernphysik, TU Darmstadt (2005), unpublished.

[Hig75] V. Highland, Nucl. Instr. and Meth. **129** (1975) 497 (DOI).

[Hig79] V. Highland, Nucl. Instr. and Meth. **161** (1979) 171 (DOI).

[Hir06] K. Hirose, M. Chiba, M. Inoue, H. Kanda, R. Kimura, K. Kino, Y. Kobayashi, O. Konno, K. Maeda, H. Miyase, A. Miyamoto, T. Ohtsuki, A. Saito, T. Suda, K. Takahashi, T. Tamae, Y. Terasaki, T. Terasawa, H. Tsubota, T. Tsuruta, M. Utoyama, H. Yuuki, Y. Yamaguchi, H. Yamazaki, Nucl. Instr. and Meth. A **564** (2006) 100 (DOI).

[HPGE86] Health and Environmental Research, DOE/ER-0275-Vol. 2, page 29 (1986) (Link).

[Hum92] K. D. Hummel, *Entwicklung, Aufbau und Inbetriebnahme eines Vieldrahtdriftkammer-Detektorsystems für das QCLAM-Spektrometer am supraleitenden Darmstädter Elektronenbeschleuniger S-DALINAC*, Doctoral Thesis, Institut für Kernphysik, TH Darmstadt (1992), unpublished.

[ICRU93] ICRU Report No. 49 (1993) (DOI).

[Jac98] J. Jackson, *Classical Electrodynamics, 3rd Edition*, John Wiley & Sons, Inc, chapter 14. Radiation by Moving Charges (1998), 668 (Link).

[Kel85] J. D. Kellie, I. Anthony, S. J. Hall, I. J. D. MacGregor, A. McPherson, P. J. Thorley, S. L. Wan, F. Zettl, Nucl. Instr. and Meth. A **241** (1985) 153 (DOI).

[Ker40] D. W. Kerst, Phys. Rev. **58** (1940) 841 (DOI).

[Ker41] D. W. Kerst, Phys. Rev. **60** (1941) 47 (DOI).

[Kne06] U. Kneissl, N. Pietralla, A. Zilges, J. Phys. G **32** (2006) R217 (DOI).

[Kno82] J. W. Knowles, W. F. Mills, R. N. King, G. E. Lee-Whiting, S. Yen, B. O. Pich, J. C. Kim, T. E. Drake, L. S. Cardman, R. L. Gulbranson, Nucl. Instr. and Meth. **193** (1982) 463 (DOI).

[Kno00] G. F. Knoll, *Radiation Detection and Measurement*, John Wiley and Sons, Inc. (2000) (Link).

[Kra91] K.-H. Krause, J. Sobolewski, D. Hauff, J. M. Henneberg, N. Wieloch-Laufenberg, J. Ahrens, H. Gimm, A. Zieger, B. Ziegler, P. Rullhusen, Nucl. Instr. and Meth. A **310** (1991) 577 (DOI).

[Lan44] L. Landau, J. Phys. (USSR) **8** (1944) 201.

[Lass95] K. Lassila-Perini, L. Urban, Nucl. Phys. **A362** (1995) 416 (DOI).

[Len04] A. W. Lenhardt, *Entwicklung eines Si-Mikrostreifendetektors für das 169°-Spektrometer am S-DALINAC*, Doctoral Thesis, Institut für Kernphysik, TU Darmstadt (2004).

[Lil63a] A. C. Lilly, T. J. Weismann, D. A. Lowitz, J. App. Phys. **34** (1963) 2124 (DOI).

[Lil63b] A. C. Lilly, T. J. Weismann, D. A. Lowitz, J. App. Phys. **34** (1963) 631 (DOI).

[Lit97] V. N. Litvinenko, B. Burnham, M. Emamian, N. Hower, J. M. J. Madey, P. Morcombe, P. G. O'Shea, S. H. Park, R. S. Canon, C. R. Howell, N. R. Roberson, E. C. Schreiber, M. Spraker, W. Tornow, H. R. Weller, I. V. Pinayev, N. G. Gavrilov, M. G. Fedotov, G. N. Kulipanov, G. Y. Kurkin, S. F. Mikhailov, V. M. Popik, B. E. Norum, A. Lumpkin, B. Yang, Phys. Rev. Lett. **78** (1997) 4569 (DOI).

[Loo95] H. Loos, *Bestimmung der Elektronenpulsstruktur des S-DALINAC mit kohärenter Übergangsstrahlung*, Diploma Thesis, Institut für Kernphysik, TH Darmstadt (1995), unpublished.

[Lyn91] G. Lynch, O. Dahl, Nucl. Instr. and Meth. B **58** (1991) 486 (DOI).

[May92] T. Mayer-Kuckuk, *Kernphysik*, Teubner Studienbücher, chapter 3.5: Elektromagnetische Übergänge (1992), 88 (Link).

[Moh71] R. Mohan, M. Danos, L. C. Biedenharn, Phys. Rev. C **3** (1971) 1740 (DOI).

[Moh99] P. Mohr, J. Enders, T. Hartmann, H. Kaiser, D. Schiesser, S. Schmitt, S. Volz, F. Wissel, A. Zilges, Nucl. Instr. and Meth. A **423** (1999) 480 (DOI).

[Moh00] P. Mohr, K. Vogt, M. Babilon, J. Enders, T. Hartmann, C. Hutter, T. Rauscher, S. Volz, A. Zilges, Phys. Lett. B **488** (2000) 127 (DOI).

[Moh01] P. Mohr, M. Babilon, J. Enders, T. Hartmann, C. Hutter, K. Vogt, S. Volz, Nucl. Phys. **A688** (2001) 82c (DOI).

[Moh03a] P. Mohr, M. Babilon, D. Galaviz, K. Sonnabend, K. Vogt, A. Zilges, Nucl. Phys. **A719** (2003) 90c (DOI).

[Moh03b] P. Mohr, T. Rauscher, K. Sonnabend, K. Vogt, A. Zilges, Nucl. Phys. **A718** (2003) 243c (DOI).

[Møl32] C. Møller, Ann. Phys. **14** (1932) 531.

[Nau03] J. Naumann, G. Anton, A. Bock, P. Grabmayr, K. Helbing, B. Kiel, D. Menze, T. Michel, S. Proff, M. Sauer, M. Schumacher, T. Speckner, W. Weihofen, G. Zeitler, Nucl. Instr. and Meth. A **498** (2003) 211 (DOI).

[Net95] U. Nething, M. Galemann, H. Genz, M. Höfer, P. Hoffmann-Stascheck, J. Hormes, A. Richter, J. P. F. Sellshop, Phys. Rev. Lett. **72** (1995) 2411 (DOI).

[OBri74] J. O'Brien, H. Crannell, F. Kline, Phys. Rev. C **9** (1974) 1418 (DOI).

[Ohg91] H. Ohgaki, S. Sugiyama, T. Yamazaki, T. Mikado, M. Chiwaki, K. Yamada, R. Suzuki, T. Noguchi, T. Tomimasu, IEEE Trans. Nucl. Sci. **38** (1991) 386 (DOI).

[Par05] S. Paret, *Optimierung der Strahlführung in der Extraktion des S-DALINAC*, Diploma Thesis, Institut für Kernphysik, TU Darmstadt (2005), unpublished.

[Per52] A. M. Perry, J. C. Keck, Phys. Rev. **86** (1952) 629 (DOI).

[Pie02] N. Pietralla, Z. B. V. N. Litvinenko, S. Hartman, F. F. Mikhailov, I. V. Pinayev, G. S. M. W. Ahmed, J. H. Kelley, S. O. Nelson, R. Prior, K. Sabourov, A. P. Tonchev, H. R. Weller, Phys. Rev. Lett. **88** (2002) 012502 (DOI).

[Pla04] M. Platz, *Neuentwicklung und Aufbau einer Rechnerschnittstelle zur Ansteuerung der Geräte am S-DALINAC und Konzeption einer digitalen HF-Regelung*, Doctoral Thesis, Institut für Kernphysik, TU Darmstadt (2004).

[Pri55] B. Price, Rep. Prog. Phys. **18** (1955) 52 (DOI).

[Rau00] T. Rauscher, F.-K. Thielemann, At. Data Nucl. Data Tables **75** (2000) 1 (DOI).

[Ric47] H. Richardson, Proc. Phys. Soc. **59** (1947) 791 (DOI).

[Ric96] A. Richter, in S. Meyers *et al.*, Ed., *Proceedings of Fifth European Particle Accelerator Conference*, IOP, Bristol (1996), S. 110.

[Rye02] N. Ryezayeva, T. Hartmann, Y. Kalmykov, H. Lenske, P. von Neumann-Cosel, V. Y. Ponomarev, A. Richter, A. Shevchenko, S. Volz, J. Wambach, Phys. Rev. Lett. **89** (2002) 272502 (DOI).

[San83] A. M. Sandorfi, et al., IEEE Trans. Nucl. Sci. **30** (1983) 3083 (Link).

[Sav05] D. Savran, S. Müller, A. Zilges, M. Babilon, M. W. Ahmed, J. H. Kelley, A. Tonchev, W. Tornow, H. R. Weller, N. Pietralla, J. Li, I. V. Pinayev, Y. K. Wu, Phys. Rev. C **71** (2005) 034304 (DOI).

[Sav06] D. Savran, A. M. van den Berg, M. N. Harakeh, J. Hasper, A. Matic, H. J. Wörtche, A. Zilges, Phys. Rev. Lett. **97** (2006) 172502 (DOI).

[Sch46] L. I. Schiff, Phys. Rev. **70** (1946) 761 (DOI).

[Sch51] L. I. Schiff, Phys. Rev. **83** (1951) 252 (DOI).

[Sob00] D. I. Sober, H. Crannell, A. Longhi, S. K. Matthews, J. T. O'Brien, B. L. Berman, W. J. Briscoe, P. L. Cole, J. P. Connell, W. R. Dodge, L. Y. Murphy, S. A. Philips, M. K. Dugger, D. Lawrence, B. G. Ritchie, E. S. Smith, J. M. Lambert, E. Anciant, G. Audit, T. Auger, C. Marchand, M. Klusman, J. Napolitano, M. A. Khandaker, C. W. Salgado, A. J. Sarty, Nucl. Instr. and Meth. A **440** (2000) 263 (DOI).

[Son03a] K. Sonnabend, A. Mengoni, P. Mohr, T. Rauscher, K. Vogt, A. Zilges, Nucl. Phys. **A719** (2003) 123c (DOI).

[Son03b] K. Sonnabend, A. Mengoni, P. Mohr, T. Rauscher, K. Vogt, A. Zilges, Nucl. Phys. **A718** (2003) 533c (DOI).

[Son04] K. Sonnabend, K. Vogt, D. Galaviz, S. Müller, A. Zilges, Phys. Rev. C **70** (2004) 035802 (DOI).

[Ste66] R. M. Sternheimer, Phys. Rev. **145** (1966) 247 (DOI).

[Str57] V. Strutinski, J. Nucl. En. **4** (1957) 523 (DOI).

[Ter86] T. Terasawa, K. Mori, Y. Fujii, T. Suda, I. Nomura, O. Konno, T. Ichinohe, Y. Torizuka, K. Maeda, P. D. Harty, G. J. O'Keefe, M. N. Thompson, Nucl. Instr. and Meth. A **248** (1986) 429 (DOI).

[Tsa74] Y. Tsai, Rev. Mod. Phys. **46** (1974) 815 (DOI).

[Uts05] H. Utsunomiya, S. Goko, K. Soutome, N. Kumagai, H. Yonehara, Nucl. Instr. and Meth. A **538** (2005) 225 (DOI).

[Uts06a] H. Utsunomiya, S. Goko, H. Toyokawa, H. Ohgaki, K. Soutome, H. Yonehara, S. Goriely, P. Mohr, Zs. Fülöp, Eur. Phys. Journal A **27, s01** (2006) 153 (DOI).

[Uts06b] H. Utsunomiya, A. Makinaga, S. Goko, T. Kaihori, H. Akimune, M. Ohta, T. Yamagata, H. Toyokawa, Y.-W. Lui, S. Müller, S. Goriely, Phys. Rev. C **74** (2006) 025806 (DOI).

[Uts06c] H. Utsunomiya, P. Mohr, A. Zilges, M. Rayet, Nucl. Phys. **A777** (2006) 459 (DOI).

[Var04] V. V. Varlamov, B. S. Ishkhanov, D. S. Rudenko, M. E. Stepanov, Phys. Atom. Nucl. **67** (2004) 2107 (DOI).

[Vav57] P. Vavilov, Sov. Phys. JETP **5** (1957) 749.

[Vey70] A. Veyssiere, H. Beil, R. Bergere, P. Carlos, A. Lepretre, Nucl. Phys. **A159** (1970) 561 (DOI).

[Vog93] J. M. Vogt, R. E. Pywell, D. M. Skopik, E. L. Hallin, J. C. Bergstrom, H. S. Caplan, K. I. Blomqvist, W. D. Bianco, J. W. Jury, Nucl. Instr. and Meth. A **324** (1993) 198 (DOI).

[Vog01] K. Vogt, P. Mohr, M. Babilon, J. Enders, T. Hartmann, C. Hutter, T. Rauscher, S. Volz, A. Zilges, Phys. Rev. C **63** (2001) 055802 (DOI).

[Vog02] K. Vogt, P. Mohr, M. Babilon, W. Bayer, D. Galaviz, T. Hartmann, C. Hutter, T. Rauscher, K. Sonnabend, S. Volz, A. Zilges, Nucl. Phys. **A707** (2002) 241 (DOI).

[Vog03] K. Vogt, P. Mohr, T. Rauscher, K. Sonnabend, A. Zilges, Nucl. Phys. **A718** (2003) 575c (DOI).

[Vol05] S. Volz, *Untersuchung der elektrischen Pygmy-Dipoleresonanz in den N=82-Isotonen* ^{138}*Ba,* ^{140}*Ce,* ^{142}*Nd und* ^{144}*Sm mit Photonenstreuung am S-DALINAC*, Doctoral Thesis, Institut für Kernphysik, TU Darmstadt (2005).

[Vol06] S. Volz, N. Tsoneva, M. Babilon, M. Elvers, J. Hasper, R.-D. Herzberg, H. Lenske, K. Lindenberg, D. Savran, A. Zilges, Nucl. Phys. **A779** (2006) 1 (DOI).

[Wap03] A. H. Wapstra, G. Audi, C. Thibault, Nucl. Phys. **729** (2003) 129 (DOI).

[Wat05] S. Watzlawik, *Aufbau und Erprobung eines Messplatzes zur Bestimmung der Polarisierbarkeit des Protons und des Deuterons über eine neue Messmethode der Comptonstreuung bei niedrigen Energien am S-DALINAC*, Doctoral Thesis, Institut für Kernphysik, TU Darmstadt (2005).

[Wei53] J. W. Weil, B. D. McDaniel, Phys. Rev. **92** (1953) 391 (DOI).

[Wid28] R. Wideröe, Arch. f. Elektrotechnik. **21** (1928) 387 (DOI).

[Win93] T. Winkler, *Entwurf, Bau und Erprobung eines energiedefinierenden Blendensystems für das magnetische 40-Grad-Analysiersystem und Entwicklung eines Rechnerprogramms zur interaktiven graphischen Simulation des Strahltransports in 1. Ordnung für das magnetische Strahlführungssytem des S-DALINAC*, Diploma Thesis, Institut für Kernphysik, TH Darmstadt (1993), unpublished.

[Yao06] W.-M. Yao, C. Amsler, D. Asner, R. Barnett, J. Beringer, P. Burchat, C. Carone, C. Caso, O. Dahl, G. D'Ambrosio, A. DeGouvea, M. Doser, S. Eidelman, J. Feng, T. Gherghetta, M. Goodman, C. Grab, et. al, Journal of Physics G **33** (2006) 1 (DOI).

[Zie90] W. Ziegler, *Untersuchung niedrigliegender magnetischer Dipolstärke in den Übergangskernen* ^{148,150,152,154}*Sm mit inelastischer Photonenstreuung am S-DALINAC*, Doctoral Thesis, Institut für Kernphysik, TU Darmstadt (1990).

[Zil00] A. Zilges, P. Mohr, Prog. Part. Nucl. Phys. **44** (2000) 39 (DOI).

[Zil02] A. Zilges, S. Volz, M. Babilon, T. Hartmann, P. Mohr, K. Vogt, Phys. Lett. B **542** (2002) 43 (DOI).

Index

Acknowledgements

I am very glad to have been able to work on this project at this institute for the last four years. Sincere thanks go to Professor Dr. Andreas Zilges who took the courage to assign the task to me after a diploma thesis on a completely different topic. He allowed me great latitude in the development of the spectrometer and was always open for discussion and assistance. The whole project benefited from this leadership. I was very lucky to be part his group where heavy responsibility for one project is combined with great encouragement for all projects.

Professor Dr. Dr. h.c. mult. Achim Richter gave broad surrounding conditions and very interesting and important views for the construction and installation of the spectrometer at the S-DALINAC. He also always relied on my way to get through this project. His open-door policy made it easy to ask his advice on any major organisational questions. I would like to thank Achim Richter for the possibility to take on responsibility for such a project at the S-DALINAC.

In the early design stage the general experimental conditions at the S-DALINAC had to be carried together. Some basic questions on magnetic spectrometry had to be answered and a rough course had to be drawn up. For this purpose the knowledge of the “veterans” was indispensable. In particular Dr. Hans-Dieter Gräf, Dr. Gerhard Schrieder and Prof. Dr. Peter von Neumann-Cosel provided vital information and indicated possible problems and additional pitfalls that could have been encountered.

During the extension of the beam line of the S-DALINAC it was Dr. Ralf Eichhorn who assisted and was a consultant for the planning and installation. He was also our instructor for operating the accelerator for the test experiments. Furthermore I am indebted to him for all discussions and new ideas he contributed to optimise the experimental operation.

One of the most crucial parts of each tagging facility is the electronics and the data acquisition. After it was clear that no standard electronics can be used for the special requirements, Dipl.-Ing. Uwe Bonnes clarified the electronic limits and devised a main module. I thank him supporting me in all external discussions and to help to chose the best data acquisition system. Furthermore the electronics group and he built nearly every unit for the slow control and devices for signal processing. I really appreciate to have such an expert in-house.

Much of the basic work was done in three diploma theses by Dipl.-Phys. Jens Hasper, Dipl.-Phys. Michael Elvers and Dipl.-Phys. Janis Endres. Besides a huge work relief they have been those who critically discussed the main ideas and the details of the project. They always pointed out my faults and supported crucially the successful completion of the construction and the first test experiments.

I am very grateful to Dipl.-Phys. Stefan Paret who optimised the beam-control magnets in the beam line and calculated the position of the additional quadrupole magnets.

During this work important external contacts have been established. The person who gave me first insights into the photon-tagging spectrometry was Dr. Jürgen Ahrens from Johannes-Gutenberg University in Mainz. Dr. Andreas Reiter (U Mainz) and Dipl.-Ing. Igor Konorov (TU München) explained the importance of the data acquisition and introduced some basic principles.

The main module for the data acquisition, the CATCH module, was a development by Dr. Horst Fischer (U Freiburg) and Dr. Fritz-Herbert Heinsius (now U Bochum). They were available on every question and helped on any problems that we encountered with the operation of the module.

Dr. Bent Schröder from Lund University discussed with me the construction details of both Lund tagging facilities. The NEPTUN spectrometer design was adapted from the old Lund design. Thanks go also to the Danfysik staff, Denmark. The dipole design was done in permanent discussion and optimising. Their development effort was far beyond the standard and exceeded my early expectations.

The detector expertise was included by Dr. Eleni Berdermann (GSI Darmstadt) and Dr. Rainer Novotny (U Gießen). Eleni Berdermann advised with the electron detectors and provided diamond detectors for a possible enhancement. Rainer Novotny lent some high-efficient photon detectors for the test experiments. I am grateful for these contributions.

Finally I have to thank all other members of Zilges group. Each of them was involved in some way in the development and/or construction of the photon tagging facility. Dipl.-Phys. Sebastian Müller and Dr. Stephan Volz for any help on the installation. Dr. Deniz Savran for the help on administration and preparation of the test experiment. Dr. Kerstin Sonnabend, Dipl.-Phys. Matthias Fritzsche and Dipl.-Phys. Linda Kern for any help and discussion within all topics that our group is concerned with. Besides professional assistance the work climate was always enjoyable and honest. This was doubtlessly one of the motivations working on this project without any tedium.

Special thanks go to the students B. Sc. Anna Constantinescu, B. Sc. Christopher Romig, B. Sc. Vanessa Simon and Philipp Lang who worked on the different photon detectors and neutron detectors.

The project was funded by the Deutsche Forschungsgemeinschaft with the Sonderforschungsbereich 634 “Kernstruktur, nukleare Astrophysik und fundamentale Experimente bei kleinen Impulsüberträgen am supraleitenden Darmstädter Elektronenbeschleuniger S-DALINAC”.

Hiermit versichere ich, die vorliegende Dissertation ohne Hilfe Dritter nur mit den angegebenen Quellen und Hilfsmitteln angefertigt zu haben. Alle Stellen, die aus den Quellen entnommen wurden, sind als solche kenntlich gemacht worden. Diese Arbeit hat in gleicher oder ähnlicher Form noch keiner Prüfungsbehörde vorgelegen. Ich habe bisher an keiner in- oder ausländischen physikalischen Fakultät ein Gesuch um Zulassung zur Promotion eingereicht.

Darmstadt, den 13. Juli 2007

Unterschrift

Bildungsweg

	Persönliche Daten
Name	Kai Lindenberg
Geburtsdatum	2. August 1976
Geburtsort	Bremervörde
	Schulbildung
1983 – 1987	Findorff-Schule Iserlersheim
1987 – 1989	Orientierungsstufe Bremervörde
1989 – 1991	Gymnasium Bremervörde
1991 – 1996	Gymnasium Michelstadt
1996 – 1997	Zivildienst Odenwaldkreis
1997 – 1999	Vordiplom Physik, TU Darmstadt
1999 – 2003	Diplom Physik, TU Darmstadt
seit 2003	wissenschaftlicher Angesteller der TU Darmstadt, Institut für Kernphysik